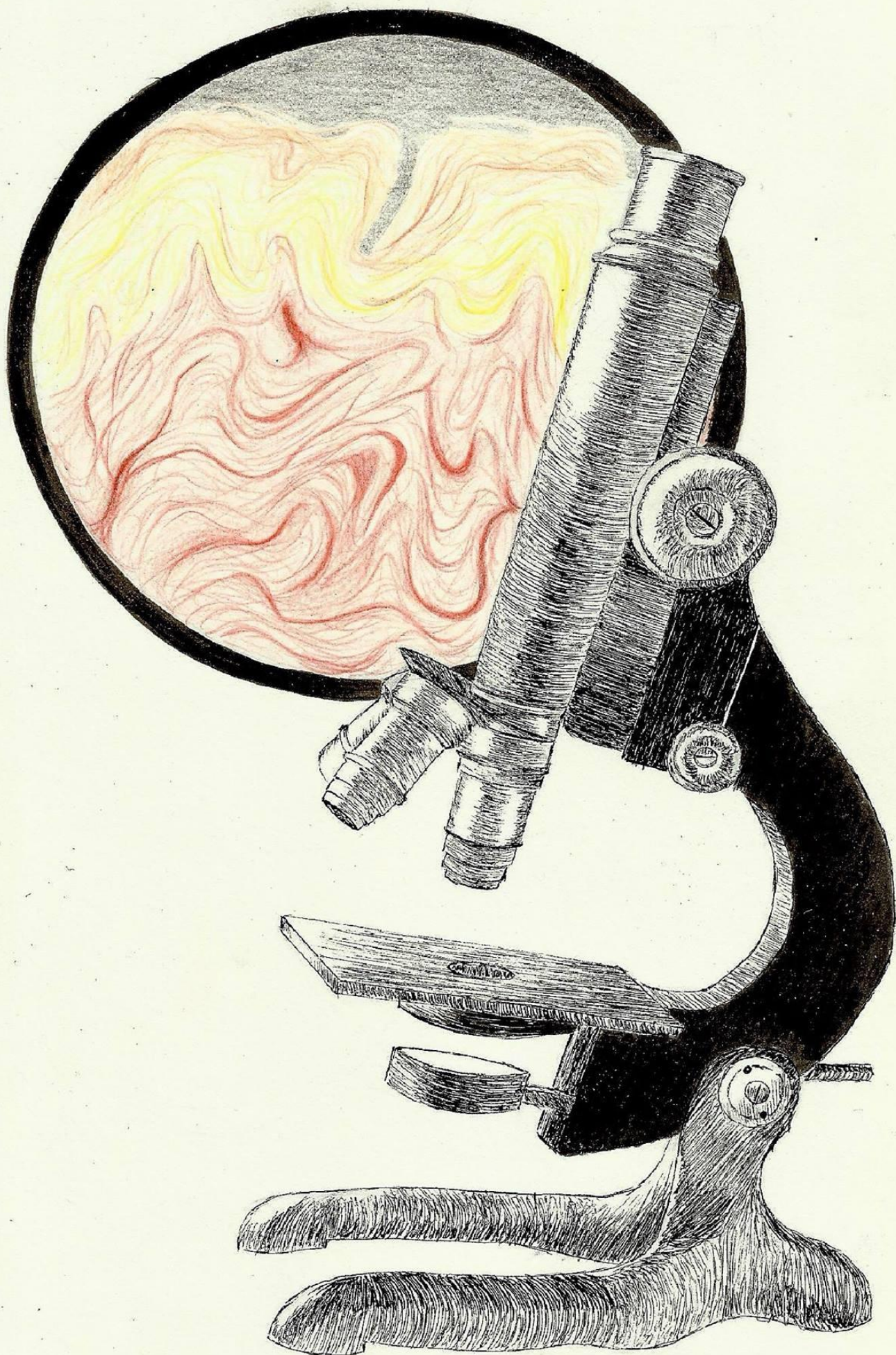


# EFFECTS OF PENETRATION ENHANCERS ON THE ARCHITECTURE AND BARRIER FUNCTION OF HUMAN SKIN



Master Thesis in Nanobioscience

**EFFECTS OF PENETRATION ENHANCERS  
ON THE ARCHITECTURE AND  
BARRIER FUNCTION OF HUMAN SKIN**

**Irina-Elena Antonescu, MSc.Pharm.**

Supervisor

**Jonathan R. Brewer**

Associate professor

Institute for Biochemistry and Molecular Biology

Co-supervisor

**Judith Kuntsche**

Associate professor

Institute for Physics, Chemistry and Pharmacy



UNIVERSITY OF SOUTHERN DENMARK

2016

# Acknowledgments

This present paper reflects the experimental research I have performed during my Master's project in Nanobioscience, for a period of 9 months. Most of the work has been undergone in the laboratories and the microscope facility at the Centre for Biomembrane Physics (MEMPHYS), University of Southern Denmark.

Assoc. prof. Jonathan R. Brewer from the Department of Biochemistry and Molecular Biology has been the initiator of this project and my main scientific support throughout the study. I must say I am really proud and lucky to have had Jonathan as a supervisor. I believe what makes Jonathan unique as a mentor is not only his problem-solving skills and creativity, but also his endless positivity and most importantly, his ability to nurture trust and confidence in his students. I am extremely grateful for his unlimited patience and guidance, which came together with a great attitude.

A great scientific support for this study has been as well my co-supervisor Judith Kuntsche, assoc. prof. in the Department of Physics, Chemistry and Pharmacy. Judith was very kind to share with me her vast knowledge in pharmaceutical design and formulation. During our collaboration, I have really seen Judith as role model, both due to her professionalism and to her dedication as a pedagogue. She has been a great help with the second part of my project and I am very thankful for her support. Also, I would like to thank Pierre-Alain Monnard for his help with one of the experimental methods in the study.

Besides my main supervisors there were actually many other scientists at MEMPHYS that provided me with advice and valuable help during this study. Among others, I would like to thank Christian Code, Jes Dreier, Jonas Jeppesen and Gustavo Scanavachi for the support and lab training they have offered me in my project. Also, I would like to thank my all my wonderful colleagues from the Bioimaging research group for the countless amounts of fruitful discussions (and cake!) we have enjoyed together in the last period. Cheers to all the scientists at MEMPHYS for creating such an inspiring environment to work in.

And not the least, deeply thankful wishes go to my lovely family and friends who have unconditionally supported me all along the way.

\*Sending heartfelt gratitude to Ida Scharla Løjmand for being so kind to hand-draw the front cover for this thesis.

# Abstract

The skin is the largest organ in the human body and a highly appealing target for drug delivery. Understanding the structural and dynamical features of the skin is essential for creating innovation in dermatological research and drug discovery. This project explores the diffusion routes of hydrophilic and hydrophobic fluorescent dyes through the skin barrier.

The first part of this project was focused on optimizing Förster resonance energy transfer (FRET) methods to measure the interactions of fluorescent molecules in stratum corneum. An additional focus was on setting up a time-resolved fluorescence anisotropy assay to determine the rotational mobility of the dyes in the skin. Similar studies were employed on artificial membranes, which were used as simple biomimetic models for the stacked lipid bilayers in the stratum corneum. The second part of the project focused on the development and characterization of a surfactant nano-carrier system for topical drug delivery. *Ex vivo* diffusion testing and confocal microscopy were used to investigate the ability of the nano-carrier to deliver fluorescent dyes through the skin barrier. A microneedle device was furtherly investigated as a physical penetration enhancer.

The FRET study demonstrated that the hydrophilic compound rhodamine B can diffuse in between the bilayers of the intercellular lipids found in the stratum corneum. It was measured to be situated at a distance of 5-8 nm from the hydrophobic dye TopFluor-PC. Time-resolved fluorescence anisotropy studies showed that rhodamine B is bound in the stratum corneum and this might influence the results obtained from the FRET studies. Stable surfactant nano-carrier systems were developed and they managed to increase ~2.9-fold the amount of the hydrophobic probe Laurdan in the epidermis and ~1.7-fold in the dermis, compared to the free dye solution. The best skin penetration of Laurdan was obtained when using a combination of the surfactant nano-carrier and a microneedle device. In this case, the penetration of the dye was increased ~5.8-fold in the epidermis and ~6.9-fold in the dermis.

# Resumé

Huden er den største organ i den menneskelige krop og en højt tiltalende mål for lægemiddeladministration. Forståelse af de strukturelle og dynamiske egenskaber af huden er afgørende for at skabe innovation i dermatologiske forskning og lægemiddelopdagelse. Dette projekt udforsker diffusionsruter af hydrofile og hydrofobe fluorescerende farvestoffer gennem hudbarrieren.

Den første del af dette projekt var fokuseret på at optimere Förster resonans energi transfer (FRET) metoder til at måle interaktioner af fluorescerende molekyler i stratum corneum. En yderligere fokus var sæt på etablering af en tidsopløst fluorescens anisotropi assay til at bestemme den roterende mobilitet af farvestoffer i huden. Lignende undersøgelser blev anvendt på kunstige membraner, som blev anvendt som simple biomimetiske modeller for de lipid dobbeltlag i stratum corneum. Den anden del af projektet var fokuseret på udvikling og karakterisering af et overfladeaktivt nano-carrier system til lægemiddeladministration til huden. *Ex vivo* diffusion test og konfokal mikroskopi blev anvendt til at undersøge hvis nano-carriers til kan øge leveringem af fluorescerende farvestoffer på hudniveau. En microneedle device blev yderligere undersøgt som en fysisk penetration forstærker.

FRET studiet viste, at den hydrofile stof rhodamin B kan diffundere til de stærkt hydrofobe dobbeltlagede stakke i stratum corneum og det beliggende på en 5-8 nm afstand fra det hydrofobe farvestof TopFluor-PC. Tidsopløst fluorescensanisotropi undersøgelser viste, at rhodamin B er bundet i stratum corneum og dette kan påvirke de opnåede resultater fra FRET undersøgelser. Stabil overfladeaktive nano-carrier systemer blev udviklet og det lykkedes dem at øge ~ 2.9 gange mængden af den hydrofobe probe Laurdan i epidermis og ~ 1.7 gange i dermis, sammenlignet med det frie farveopløsning. Den bedste hud gennemtrængning af Laurdan blev opnået ved anvendelse af en kombination af det overfladeaktive nano-bærer og en mikronål enhed. I dette tilfælde blev penetration af farvestoffet steget ~ 5.8 gange i overhuden og ~ 6.9 gange i dermis.

# Abbreviations

2D = two-dimensional;

CHOL = cholesterol;

CPP = critical packing parameter;

DHPE = 1,2-dihexadecanoyl-*sn*-glycero-3-phosphoethanolamine;

DOPC = 1,2-dioleoyl-*sn*-glycero-3-phosphocholine;

DLS = dynamic light scattering;

DPPC = 1,2-dipalmitoyl-*sn*-glycero-3-phosphocholine;

DPPE = 1,2-dipalmitoyl-*sn*-glycero-3-phosphoethanolamine;

EE% = entrapment efficiency %;

FLIM = fluorescence lifetime imaging microscopy;

FRET = Förster resonance energy transfer;

HEPES = 4-(2-hydroxyethyl)-1-piperazineethanesulfonic acid;

HLB = hydrophilic-lipophilic balance;

HPD = hybrid photo detector;

HPLC = high performance liquid chromatography;

NIOSOME = non-ionic surfactant vesicle;

PC = phosphocholine;

PDI = polydispersity index;

PMT = photomultiplier tube;

POPC = 1-palmitoyl-2-oleoyl-*sn*-glycero-3-phosphocholine;

Rh-B = rhodamine-B;

TCSPC = time-correlated single photon counter;

TLH = thin-layer hydration;

SAXS = Small-angle X-ray scattering;

SC = stratum corneum;

# Table of contents

Acknowledgments .....	I
Abstract.....	II
Resumé.....	III
Abbreviations .....	IV
Table of contents.....	V
<b>Chapter I: Introduction and theory .....</b>	<b>1</b>
1.1. Overview of the project.....	1
1.2. The skin barrier .....	3
1.3. Nano-carriers for skin delivery.....	5
1.4. Physical penetration enhancers .....	9
1.5. Two-photon microscopy .....	10
1.6. Förster resonance energy transfer (FRET) .....	11
1.7. Polarization-resolved fluorescence imaging .....	13
1.7.1. The process of photoselection.....	14
1.7.2. Anisotropy imaging .....	14
<b>Chapter II: Materials and methods .....</b>	<b>15</b>
2.1. Materials .....	15
2.2. Methods.....	16
2.2.1. Preparation of supported lipid bilayers .....	16
2.2.2. Förster resonance energy transfer (FRET) measurements .....	17
2.2.3. FLIM setup for FRET studies.....	18
2.2.4. Fluorescence anisotropy measurements .....	18
2.2.5. Preparation of skin samples for the FRET and diffusion experiments.....	20
2.2.6. Preparation of non-ionic surfactant nano-vesicles .....	20
2.2.7. Niosome characterization .....	21
2.2.8. <i>Ex vivo</i> skin permeation study.....	23
<b>Chapter III: Results and discussion .....</b>	<b>27</b>
3.1. FLIM/FRET studies.....	27

3.1.1. Förster resonance electron transfer (FRET) in POPC supported bilayers .....	27
3.1.2. Förster resonance energy transfer (FRET) in human skin.....	31
3.2. Fluorescence anisotropy studies.....	36
3.2.1. Calibration of the polarization-resolved microscope.....	36
3.2.2. Fluorescence anisotropy in ternary supported lipid bilayers .....	37
3.2.3. Fluorescence anisotropy in human skin.....	38
3.3. Niosome formulation and characterisation .....	41
3.3.1. Shape and morphology of the niosomal formulations.....	41
3.3.2. Particle size.....	44
3.3.3. Physical stability.....	45
3.3.4. Encapsulation efficiency .....	46
3.4. <i>Ex vivo</i> skin diffusion testing of nano-formulations.....	48
<b>Chapter IV: Conclusions and future perspectives.....</b>	<b>52</b>
Bibliography .....	54
Appendix.....	59

# Chapter I: Introduction and theory

## 1.1. Overview of the project

The skin is an extremely attractive site for drug delivery, as it is the most accessible organ of the body, with a large surface area and it avoids the disadvantages linked with the invasive and costly parenteral route or the oral route, which can be weakly bioavailable for many classes of compounds [9, 10]. But there are many challenges that hinder the advances in dermal and transdermal drug delivery. Most of them are related to the low permeability of drug compounds through the highly effective barrier provided by the *stratum corneum* (SC), the outermost layer of the skin.

Many structural aspects of the stratum corneum are not yet fully understood. The main focus of this project was to investigate the lipid packing, barrier properties and drug diffusion through human SC and the inner skin layers. The skin was studied either in its native form or after treatment with pharmaceutical nano-formulations or physical penetration enhancers.

**In the first part of this project**, techniques like fluorescence lifetime imaging microscopy (FLIM) - Förster resonance energy transfer (FRET) and fluorescence anisotropy were applied to evaluate the properties of the stacked lipid layers that fill the extracellular space of the stratum corneum and play a key role in controlling its skin barrier capacity. FRET was employed to quantify the nanoscopic structure and dynamics in artificial membranes and in skin tissue. In particular, we have focused on exploring the nanoscopic diffusion routes of compounds hydrophilic and hydrophobic fluorescent dyes at the level of the stacked lipid bilayers in SC.

Fluorescence resonance energy transfer or Förster resonance energy transfer (FRET) is a distance-dependent interaction between the electronic excited states of two dye molecules, in which excitation is transferred from a donor molecule to an acceptor molecule, without the emission of a photon. The efficiency of FRET is dependent on the inverse sixth power of the intermolecular separation, making it useful over distances comparable to the dimensions of biological macromolecules. Thus, FRET is an important technique for investigating a variety of biological phenomena that produce changes in molecular proximity.

The FRET is highly dependent on the distances between molecules but also on the dipole orientation of the dyes added to the skin sample. In parallel with the FRET measurements, we have developed a time-resolved fluorescence anisotropy setup to study the rotational mobility of the molecules in the skin.

This first part of the study was intended to find answers to questions like: How do hydrophilic and hydrophobic dyes diffuse at the level of the stacked lipid bilayers in the SC? Can they interact with each other through FRET? If yes, does it happen in a concentration dependent manner? Do the dye molecules bind or interact with other

structures in the skin? Are FRET and anisotropy comparable in skin and artificial lipid bilayers?

**The second part of this project** was focused on designing a surfactant-based nano-carrier system and evaluating if it can alter the skin barrier function and deliver hydrophobic and hydrophilic compounds to the deeper layers of the skin. This effect was studied both on normal skin and on skin punctured with a microneedle device.

Surfactant-based nanoparticles (niosomes) can work as penetration enhancers by aiding the local fluidization of the *stratum corneum* lipids, which then allows for the nanoparticles to sit in the upper layers of the stratum corneum, where they can form a reservoir for prolonged effect [11]. Niosomes have been shown to provide enhanced drug penetration, sustained drug release, increased drug stability and ability work as a nano-carrier for both hydrophilic and lipophilic drugs through the skin [7, 12-15]. Microneedle devices are used to physically disrupt the skin barrier and promote the transfer of externally applied compounds towards the micro-capillary bed of the dermis, where they can become available to be taken up by the systemic circulation [16-18].

Research questions that formed the basis of this second part of this project included, but were not limited to: Can stable bilayer vesicles be prepared by using combinations of surfactants and cholesterol? What are the preferred type of surfactants and how does their critical packing parameter and hydrophilic-lipophilic balance influence the quality of the formed vesicles? Can these surfactant vesicles incorporate hydrophilic and lipophilic compounds and improve their delivery through the skin? Moreover, what happens when they are applied on punctured skin instead of normal skin?

The present paper is divided in four chapters. **The first chapter** introduces the theoretical background and motivation for performing the experimental research. **The second chapter** describes the methods and techniques employed and optimized to fit the aims of the study. **The third chapter** presents and discusses the results of both parts of the study as a whole. And lastly, **the fourth chapter** sums up the main findings of this study and describes how the work could be continued.

## 1.2. The skin barrier

The skin is the outermost organ of the body. It works both as an envelope, retaining water inside the body and as a barrier that limits the penetration of external agents. The skin constitutes of several layers which differ in their composition and structure (figure 1). The deepest skin layer is the hypodermis and it is composed of fatty tissues (adipocytes). The middle skin layer is the dermis, a hydrophilic layer having a gel-like composition. In the dermis, a dense network of fibers (elastin and collagen) provide mechanical strength to the skin. The dermis is irrigated by the blood circulation, therefore any substance reaching the dermis can pass into the systemic circulation. The epidermis, the outer layer of the skin, is an epithelium divided into two different areas: the viable epidermis, a living hydrophilic layer containing 70% of water, and the stratum corneum (SC) a hydrophobic layer containing only 13% of water.

The layered structure of skin is continuously renewed and provides efficient protection against the penetration of most kinds of xenobiotics. Hydrophilic compounds are not able to easily penetrate the skin as they cannot enter the hydrophobic SC layer. On the other side, when a compound is hydrophobic, it has a good chance to overpass the SC but it will not be able to advance much deeper since the next layer is hydrophilic. [19]

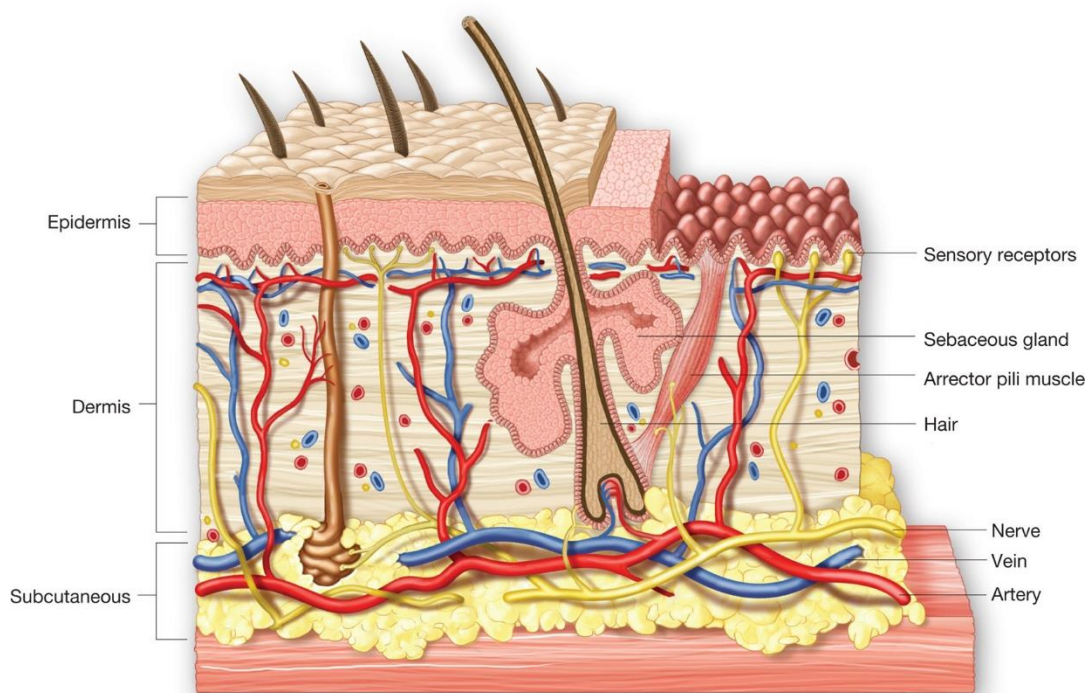


**Figure 1.** The structure of the skin. The image depicts the three layers of the skin (epidermis, dermis, subcutaneous tissue) and the accessory organs (sweat gland, sebaceous gland, and hair) [20].

*Dermal drug delivery* is the topical application of therapeutic compounds to the skin in the treatment of skin diseases. A notable advantage of this route is that increased levels

of drugs can be localized at this action site, with a reduction in the systemic drug levels and therefore also reducing the systemic side effects.

Opposed to dermal delivery, *transdermal drug delivery* employs the skin as an alternative route for the delivery of drugs that can act at a systemic level. This route is in many cases preferred to the oral route of administration, due to the many advantages it presents. Firstly, it avoids factors that could affect gastro-intestinal drug absorption such as pH, gastro-intestinal motility and food intake. Secondly, it can be suitable for drugs with reduced bioavailability as it circumvents the hepatic first-pass effect. Thirdly, the transdermal drug delivery can provide a controlled, constant flux of drug with reduced plasma level variations, which is especially relevant for reducing the adverse reactions of medicines with a narrow therapeutic window [21].

Despite the fact that the skin is a highly desired target for drug delivery, only a few drugs on the market have been accepted for transdermal application. This is mainly due to the low permeability of drugs through the *stratum corneum* [17], the outermost layer of skin which acts as a highly effective barrier against the diffusion of xenobiotics through skin [21].

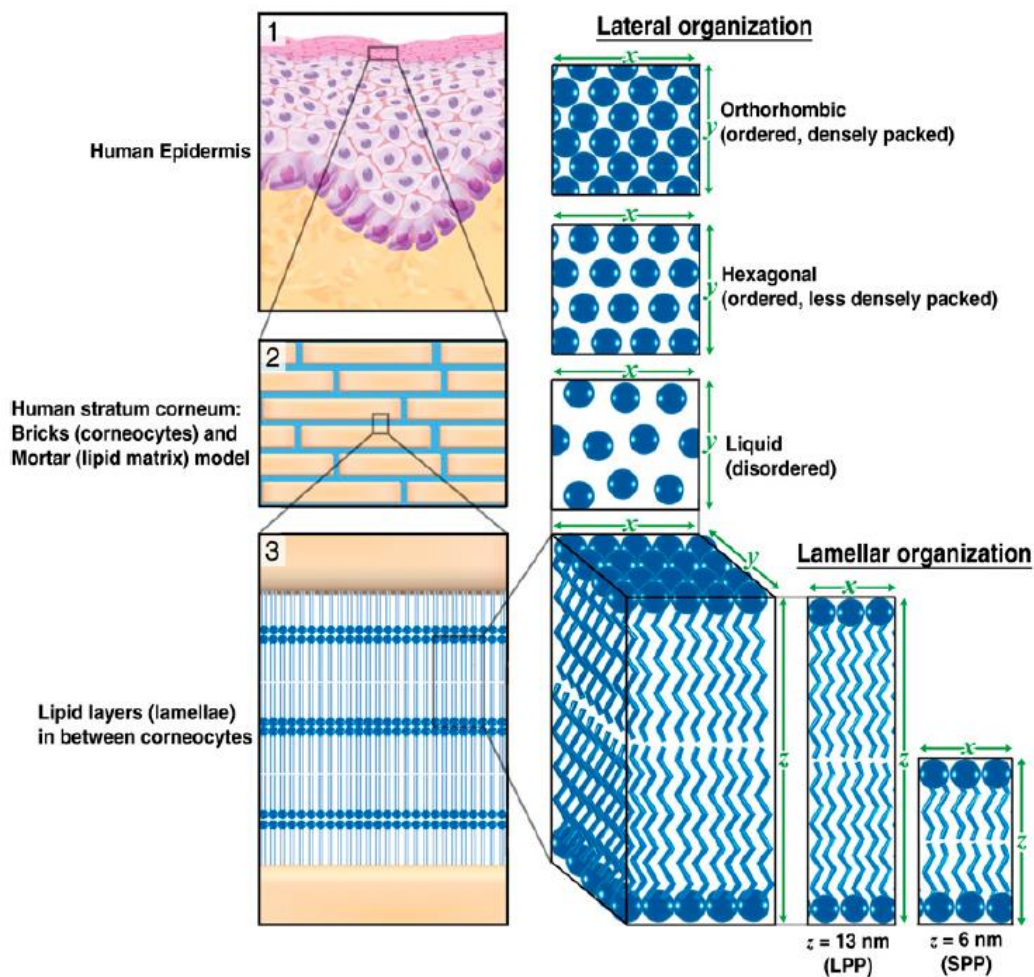


**Figure 2.** Lamellar and lateral organization in human stratum corneum [8].

Even though the stratum corneum is only 10-20  $\mu\text{m}$  thick, its highly organised structure plays the major role in skin's formidable barrier capacity. SC is highly hydrophobic and contains 10-15 layers of dead cells called corneocytes. Its "brick and mortar" structure is analogous to a wall (figure 2.2.). In this structure, the corneocytes of hydrated keratin comprise the "bricks". They are embedded in a "mortar" which consists of multiple intercellular lipid bilayers that contain a heterogeneous mixture of saturated, long-chain ceramides (CERs), cholesterol and free fatty acids in an approximately 1:1:1 molar ratio [22]. The intercellular lipids are arranged in layers (lamellae), pictured in figure 2.3, with two coexisting lamellar phases. These lamellar phases have a repeat distance of 6 nm (referred to as the SPP) or 13 nm (referred to as the LPP). The lateral organization is the plane perpendicular to the direction of the lamellar organization. There are three possible arrangements of the lipids: a very dense, ordered orthorhombic organization; a less dense, ordered hexagonal organization; and a disordered liquid organization [8]. Most molecules penetrate through skin *via* this intercellular micro-route and therefore many penetration enhancing techniques aim to disrupt or bypass its highly organized structure [23].

A broad variety of dermal and transdermal penetration enhancing and skin delivery methods have been designed. These include chemical penetration enhancers (*i.e.* DMSO, free surfactants or fatty acids)[24], nano-carriers (figure 3), and physical enhancers like microneedles, iontophoresis or electroporation [17]. The present study was focused on surfactant-based nano-carriers and microneedle-mediated penetration enhancement.

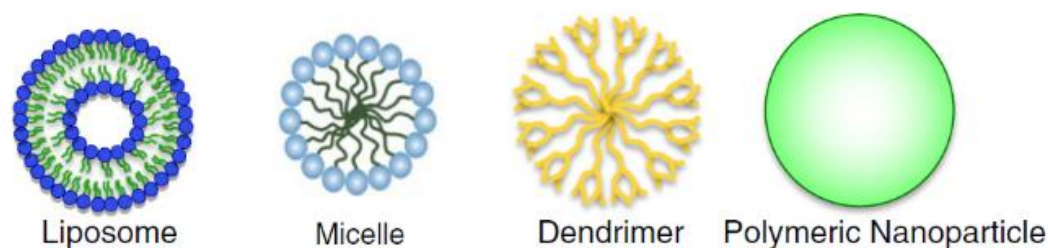


**Figure 3.** The main classes of nano-carriers employed as drug delivery systems [12].

## 1.3. Nano-carriers for skin delivery

### 1.3.1. Elastic vesicles: mechanisms of improved topical delivery

During the last decades of skin delivery research, it has been proved that the behaviour of vesicles applied on the *stratum corneum* is not only influenced by the liquid-state of the vesicle bilayer, but also by the bilayer elasticity [21]. Transfersomes®, the first generation of elastic vesicles introduced by Cevc et al. in 1992, were reported to penetrate intact skin carrying therapeutic concentrations of drugs, when applied under non-occluded conditions [25]. They are composed of lipids, such as phosphatidylcholine and an edge activator. The edge activator is often a single chain surfactant which increases the deformability of the bilayers by having a destabilizing effect on the lipid

bilayers of the vesicles. Sodium cholate, Span 80, Tween 80 and dipotassium glycyrrhizinate have been investigated as edge activators [26].

The second generation of elastic vesicles is composed only of mixtures of surfactants and was developed by Van den Bergh [27]. Their elasticity is achieved by the same principle as for the first generation of elastic vesicles: the combination of both stabilizing and destabilizing agents which are able to redistribute within the same vesicle bilayer. By using multiphoton excitation microscopy, Van den Bergh has showed that fluorescent dye-loaded elastic vesicles manage to penetrate into the deeper layers of the stratum corneum by creating a fine meshwork of thread-like channels, but do not enter systemic circulation.

The mechanisms by which vesicles interact with stratum corneum and aid the (trans)dermal diffusion of drugs have been long time debated, with three central mechanisms having been described: **a)** the vesicles fuse with or are being adsorbed on the skin surface; **b)** constituents of the vesicle penetrate into the skin and alter the ultrastructure of the intercellular space in the stratum corneum; **c)** the vesicles penetrate intact through the stratum corneum and localize into the stratum corneum or diffuse to the dermis [28].

### 1.3.2. Non-ionic surfactant particles: properties and formulation

The present study aimed at formulating and characterizing non-ionic surfactant vesicles as skin penetration enhancers. Non-ionic surfactant vesicles, more simply known as *niosomes*, are synthetic vesicles composed mainly of hydrated surfactants in addition to, in many cases, cholesterol or other amphiphilic molecules. Niosomes are formed by the self-assembly of the amphiphilic molecules into double bilayers which form spherical vesicles (figure 4). Due to their unique structure, niosomes can incorporate both hydrophilic and lipophilic compounds. The water-soluble compounds are entrapped in the aqueous core of the vesicle or adsorbed on the surface of the bilayer, while lipophilic compounds are loaded by partitioning in the hydrophobic domain of the bilayer [7].

Niosomes have received great attention as nano-carrier systems or penetration enhancers for dermal and transdermal drug delivery. They have been studied as an alternative to liposomes as they have proven to overcome many of the challenges presented by phospholipid-based systems. Surfactants can be easily derivatized and provide a higher versatility to the vesicular structures compared to phospholipids. Also, niosomes are more cost-effective and relatively straight forward for routine and large scale production, which makes them a better choice when considering industrial manufacturing [7, 29-31].

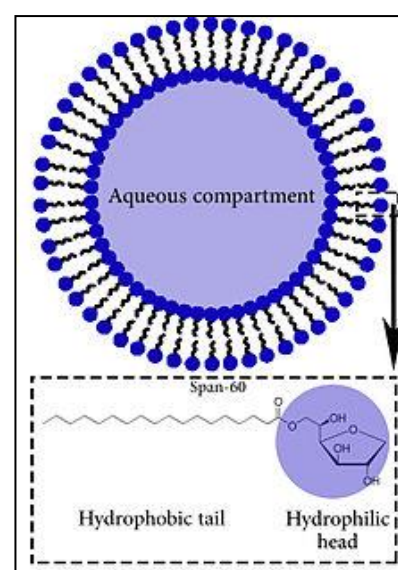


**Figure 4.** 2D structure of a niosomal vesicle composed of sorbitan monostearate (Span 60)

The formulation aspects of niosomes dictates their physico-chemical properties such as size, lamellarity, thermodynamic phase, electric charge and bilayer elasticity. These characteristics influence the behaviour of the vesicles on skin and thus their efficacy as drug delivery systems [21]. Thermodynamically stable vesicles can be formed only in the presence of appropriate mixtures of surfactants and other stabilisers such as cholesterol. Central factors that determine the self-assembly of amphiphiles are parameters like the hydrophilic-lipophilic balance (HLB) and the geometrical features of the molecules.

The HLB number can predict whether a compound is able to form vesicles. For sorbitan monostearate surfactants, a HLB value between 4 and 8 was found to be compatible with the formation of vesicles. On the other side, surfactants with a high HLB value, between 14 and 17, and not able to form free hydrated units (vesicles). Due to their high water solubility, these free units aggregate to form lamellar structures.

The geometrical properties of the single vesicle-forming unit is another important factor dictating the type of structure formed upon the interaction of surfactant films with water environments. The critical packing parameter (CPP) value indicates whether the shape and size of the equilibrium aggregate should evolve from spherical micelles at low CPP values ( $\leq 1/3$ ) to cylindrical micelles ( $1/3 \leq \text{CPP} \leq 1/2$ ), bilayers ( $1/2 \leq \text{CPP} \leq 1$ ) or inverse micelles at high CPP values ( $> 1$ ). Figure 5 shows a schematic representation of these macromolecular assemblies and the relation used to determine CPP [12].

$$CPP = \frac{V}{a_0 l_c}$$

CPP = critical packing parameter; V = tail volume of the molecule;  $a_0$  = the polar head area;  $l_c$  = the critical lipophilic tail length;

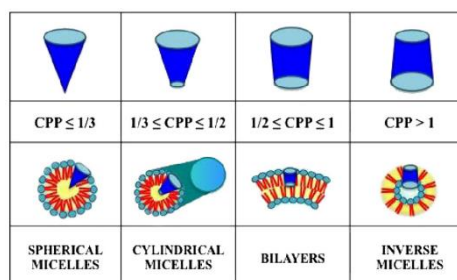


**Figure 5.** Left: The geometrical parameters used to calculate the critical packing parameter (CPP). Right: The influence of CPP of amphiphilic molecules on the morphology of self-assembled structures [12].

**Table I.** Properties of the surfactants used in the present study [11].

<i>Surfactant</i>	<i>Chemical identity</i>	<i>Alkyl chain length</i>	<i>HLB</i>	<i>CPP</i>
Tween 60	PEG-20 sorbitane monostearate	18:0	14.9	< 0.33 [32]
Tween 80	PEG-20 sorbitane monooleate	18:1	15	
Span 60	Sorbitane monostearate	18:0	4.7	0.5-1 [33]
Span 80	Sorbitane monooleate	18:1	4.3	

The CPP and HLB values of the surfactants used in this study is present in table I and their structures can be found in figure 6. By combining different ratios of sorbitan esters (Span 60 and Span 80) and polyethoxylated sorbitan esters (Tween 60 and Tween 80) in the formulation of niosomes, one can achieve systems with a wide range of HLB values and packing morphologies, which can affect the encapsulation and delivery of compounds. Sorbitan esters and their ethoxylated derivatives are easily accessible and have a low toxicity. They are widely used in cosmetics, some pharmaceutical preparations and even as food additives [34].

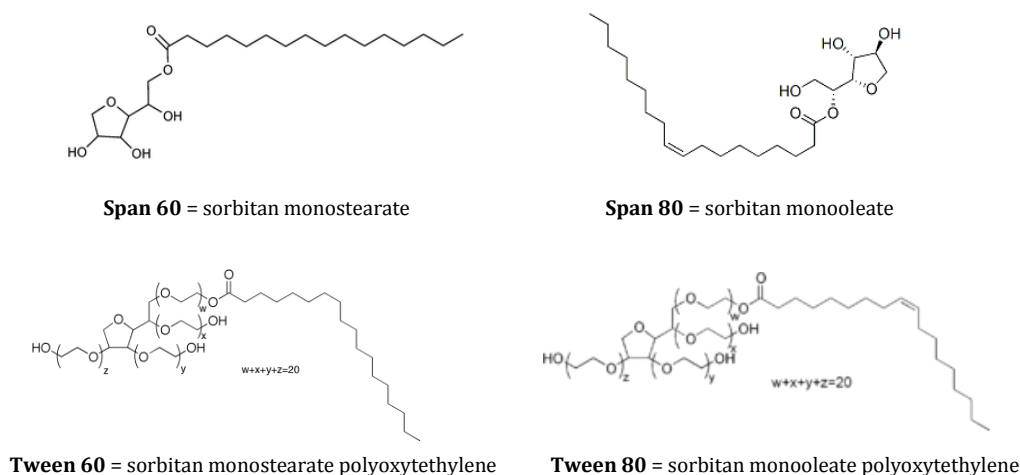


**Figure 6.** Chemical structures of the surfactants. Source: chemicalize.org

Cholesterol is used as an additive in large number of niosomal formulations. For surfactants with HLB > 6, cholesterol must be added to the formulations in order to obtain bilayers. For surfactants with lower HLB values, cholesterol can as well enhance the stability of the vesicles by promoting the gel liquid transition temperature (T<sub>c</sub>) of the vesicles [7, 35].

Several research initiatives have been successful at developing niosomes composed of mixtures of Span and Tween surfactants [31, 36] and some of them have been tested as dermal and transdermal drug delivery systems. Junyaprasert et al has shown that niosomes composed of a mixture of 2:1 Span 60: Tween 60 have proved to increase the skin delivery of ellagic acid. [14] The same author reports the combination of niosomes with different chemical penetration enhancers to achieve epidermal and dermal delivery [37]. Tavano et al have designed niosomes where they mixed different ratios of Span 80 and Tween 80 to obtain a series of HLB values in the formulations. They have shown that the niosome formulations can successfully deliver capsaicin to the skin and proved to be superior to microemulsions. The formulation with an HLB of 12 showed to be the most effective at improving the skin delivery of capsaicin [15].

## 1.4. Physical penetration enhancers

Many skin penetration enhancement techniques are based on the use of physical approaches like the application of electric energy (iontophoresis and electroporation), ultrasound (phonophoresis) or minimally invasive techniques as skin micro-poration (microneedles, thermal micro-poration and radiofrequency ablation). Each technique has been pursued by a variety of pharmaceutical companies and they all have the potential to enable the skin delivery of drugs, even with bioavailabilities of  $\geq 50\%$  [9, 10, 38].

One exciting physical penetration enhancing technology is the skin micro-poration with the use of microneedles, which is intensely investigated for the delivery through the skin of small water-soluble drugs or macromolecules such as proteins and vaccines. As a bridge between conventional hypodermic needles and passive transdermal patches, microneedles act by inducing reversible micron-sized transport pathways in the skin, which are much smaller than the holes created by hypodermic needles, but considerably larger than most macromolecules, allowing the skin permeation of dissolved APIs of any size [9, 10, 16]. The most usual mode of microneedle application is micro-poration of the skin followed by the application of a liquid formulation or drug-loaded patch. The aqueous pores in the skin subsequently allow the diffusion of the drug from the liquid formulation or patch into the deeper layers of the skin [9].

In terms of progress towards clinical application of the microneedle technology, the majority of the ongoing human trials are focused on vaccine delivery. Vaccination is a very attractive option for the first attempt to bring this technology to the market due to several factors: there is a very low active dose required, administration is not necessary on a continuous basis, there is a relatively large therapeutic window and skin can provide an excellent “amplification” system for the desired immune response [39].

Various microneedle approaches have been studied *ex vivo*, *in vivo* and/or in phase II clinical trials for the transdermal delivery of proteins like insulin or heparin [40-44], with promising results.

Furthermore, combinations of two or more penetration-enhancing chemical and physical techniques might result in a synergistic effect which provides increased drug delivery to the skin [9].

## 1.5. Two-photon microscopy

Multiphoton excitation microscopy is a type of optical microscopy that has seen a continuous growing interest among the microscopy techniques used for studying biological matter. Even though it has a lower resolution with respect to techniques like electron microscopy, optical microscopy offers the unique advantage of allowing the visualization of biological systems in conditions that are very close to their natural biological states. Together with the possibility to perform fluorescence labelling and other molecular biology advances, optical microscopy can provide an efficient way to tackle the complicated challenge of finding the structure-function relations in biological systems [45].

The phenomenon of multiphoton excitation can be visualized in a Jablonski diagram (figure 7). Two-photon excitation is a non-linear process based on the possibility of a fluorophore to absorb simultaneously two photons in the infrared (IR) range whose total energy is equal to the energy needed for the one-photon excitation in the visible or ultraviolet (UV) range. This brings the advantage that deep UV microscopy can be realised without the disadvantages of UV-matter interactions [45, 46].

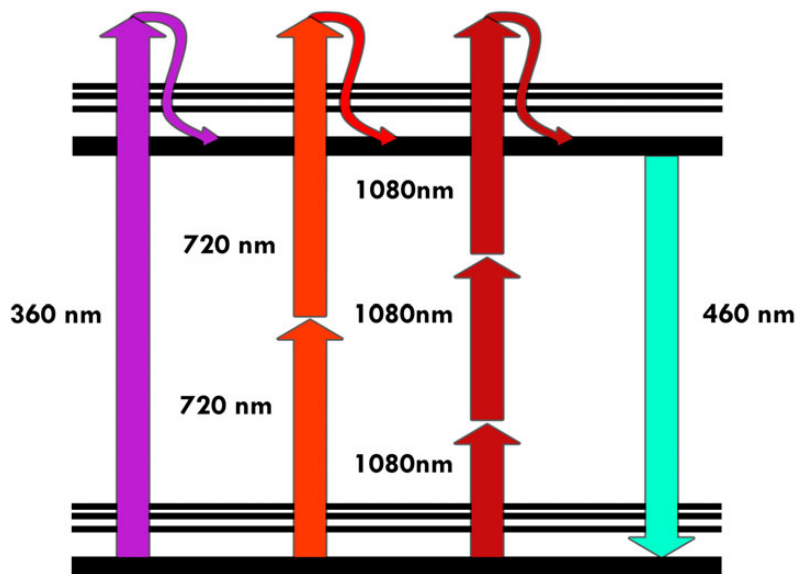


**Figure 7.** Simplified Perrin-Jablonski fluorescence diagram illustrating the principle of one-, two- and three-photon excitation. Once the excited state is reached, the following emission of fluorescence is the same for all the three excitation modalities [45].

Other notable advantages of two-photon microscopy include an inherent optical sectioning capability. This is due to the fact that it excites just one small femtoliter volume around the focus of the focusing lens. This will also cause less bleaching of the fluorophores in the samples. Also, in two-photon microscopy a relatively high depth penetration into the tissue can be achieved due to the use of NIR light which has a much lower scattering through the skin compared to light in the visible or UV range. And not lastly, by using two-photon microscopy there is no need to suppress the out of focus light as in the case of one-photon 3D microscopy [46].

## 1.6. Förster resonance energy transfer (FRET)

Förster Resonance Energy transfer (FRET) is an electrodynamic phenomena that involves the non-radiative transfer of energy between a donor molecule in its excited state and an acceptor molecule in its ground state (figure 8). The latter may be fluorescent or non-fluorescent.

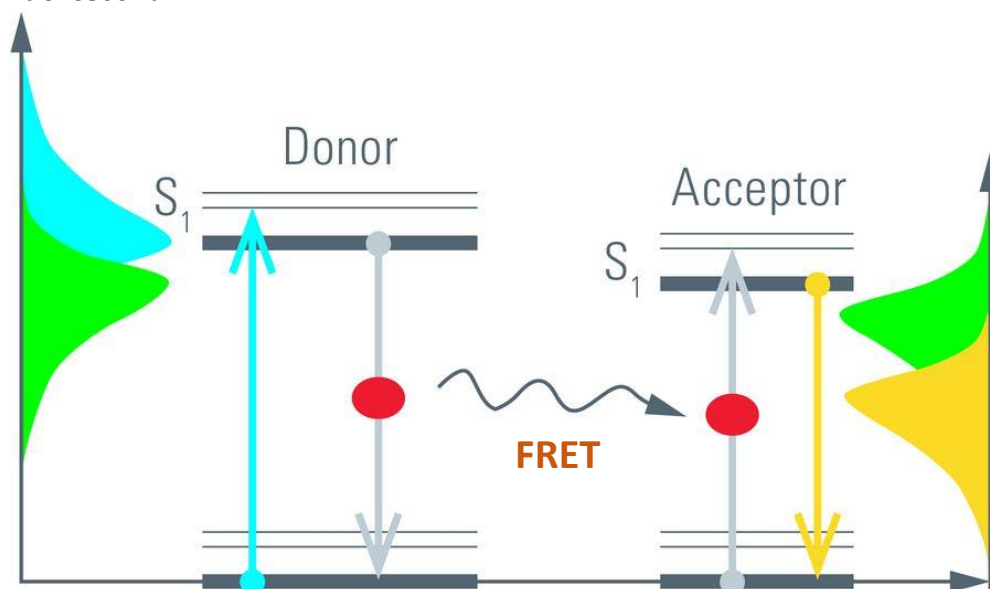


**Figure 8.** Schematic illustration of the Förster resonance energy transfer from a donor molecule to an acceptor molecule [47].

This energy transfer is possible due to long range dipole-dipole interactions between the donor and the acceptor molecules. Usually, the donor molecule emits at a shorter wavelength, which matches the absorption spectra of the acceptor. The transfer occurs without the emission of a photon. In some cases, the same fluorophore can function as both a donor and acceptor. This phenomena it is called homo-FRET [48, 49].

The rate at which FRET occurs depends on many aspects, including the donor-acceptor spectral overlap, the relative orientation of the donor and acceptor dipoles and the distance between the donor and acceptor molecules. There is a term that defines the distance at which FRET is 50% efficient. This is called the Förster distance ( $R_0$ ) and is usually in the range of 2-6 nm. The rate of energy transfer from a donor to an acceptor  $k_T(r)$  is given by equation 1.

$$k_T(r) = \frac{1}{\tau_D} \left(\frac{R_0}{R}\right)^6 \quad (\text{eq. 1})$$

Where  $\tau_D$  is the lifetime of the donor fluorophore,  $R_0$  is the Förster distance and  $R$  is the donor-acceptor distance. Hence, when the fluorophores are separated by a distance equal to their Förster radius ( $R = R_0$ ), the transfer rate is equal to the rate of decay of the fluorophore [48]. The equation shows the high dependency of the rate of FRET on the donor-to-acceptor distance, as it varies inversely with the 6<sup>th</sup> power of the distance  $R$  between the donor-acceptor separation, over a range of 1-10 nm [49].

The fraction of the photons absorbed by the donor which get transferred to the acceptor is called the efficiency of energy transfer ( $E_{FRET}$ ) and is given by equation 2.

$$E_{FRET} = \frac{k_T(r)}{\tau_D^{-1} + k_T(r)} \quad (\text{eq. 2})$$

By replacing  $k_T(r)$  from eq. 1 one can easily rearrange eq. 2 to yield equation 3.

$$E_{FRET} = \frac{R_0^6}{R_0^6 + r^6} \quad (\text{eq. 3})$$

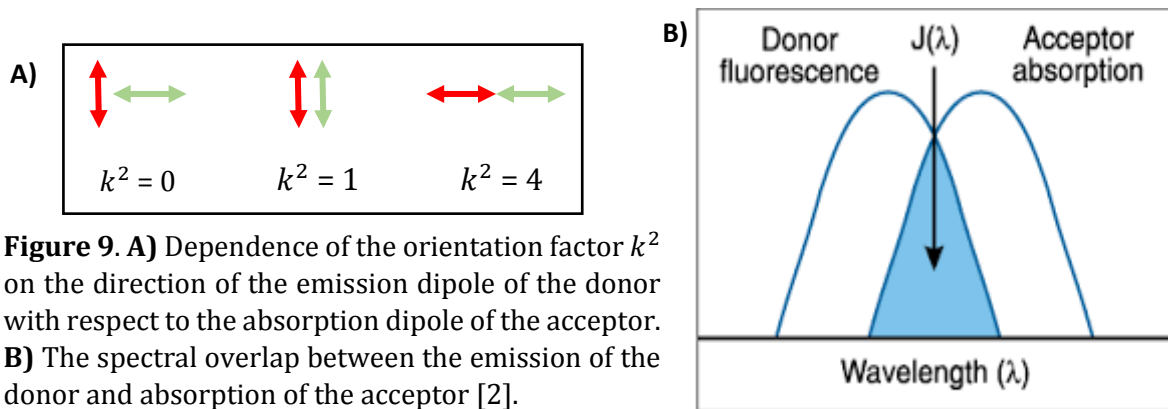
By knowing the FRET efficiency in the system, one can calculate the distance between two molecules, which is equal to:

$$R = \left(\frac{1}{E} - 1\right)^{\frac{1}{6}} * R_0 \quad (\text{eq. 4})$$

The Förster distance  $R_0$  is typical for any FRET pair in a defined environment and is defined as:

$$R_0 = 0.211(k^2 n^{-4} Q_D J(\lambda))^{1/6} \quad (\text{eq. 5})$$

Where  $R_0$  is the Förster distance in Å,  $k^2$  is the orientation factor describing the relative orientation in space of the transition dipoles of the donor and acceptor. Even though  $k^2$  can have values from 0 to 4 (figure 9A), it is generally assumed equal to 2/3, which is the value for donors and acceptors that randomize by rotational diffusion prior to the energy transfer;  $n$  is the refractive index of the medium;  $Q_D$  is the lifetime of the donor in the absence of the acceptor and  $J(\lambda)$  is the spectral overlap integral of the pair [48]. The spectral overlap for each FRET pair can be obtained by calculating the surface where the donor emission spectrum overlaps with the donor absorption spectrum, as shown in figure 9B.



$R_0$  can be theoretically estimated for each donor-acceptor pair and it has values in the range of 2-10 nm. By calculating this constant and determining the  $E_{FRET}$  between the dyes, one can calculate very small distances between molecules, usually between  $\sim 0.5 R_0$  and  $\sim 1.5 R_0$ . These distances are much below the resolution limit of optical microscopy [48].

## 1.7. Polarization-resolved fluorescence imaging

Polarization measurements can bring information on the characteristics of a fluorophore that cannot be not be quantified by fluorescence intensity or lifetime methods. Some of the features that can be investigated using polarization measurements include molecular orientation, energy migration (homo-FRET), and rotational diffusion. All these phenomena lead to a depolarization of the light emitted by the fluorophore [50].

For anisotropy measurements, polarization can be discussed in terms of the fluorescence anisotropy,  $r$ , which is defined by the Jablonski-Perrin equation in equation 6.

$$\frac{r_0}{r} = 1 + \frac{\tau}{\theta} \quad (\text{eq. 6})$$

Where  $r_0$  is a fixed molecular property of the fluorophore and it represents the anisotropy that would be measured in the absence of rotational diffusion (also called initial anisotropy);  $\tau$  is the fluorescence lifetime of the molecule;  $\theta$  is the rotational correlation time for the diffusion process and it describes the molecular tumbling in the molecule [46].

For the rotational correlation time, the use of the Stokes–Einstein equation gives equation 7:

$$\theta = \frac{4\pi a^3 \eta}{3kT} \quad (\text{eq. 7})$$

Where  $\theta$  is the rotational correlation time of the molecule (the time it takes for a molecule to rotate one radian, on average,  $a$  is the apparent molecular radius of the molecule,  $k$  is the Boltzmann constant, and  $T$  is the absolute temperature [51].

By knowing the fluorescence anisotropy and the lifetime of a fluorescent molecule, one can calculate  $\theta$  using the Jablonski-Perrin equation and then use it to deduce the hydrodynamic volume of a fluorophore or the viscosity of the medium where the molecule is situated.

In practice, fluorescence anisotropy is measured by exciting the sample using a linearly polarized light source and then measuring the time-resolved intensities of the components of the fluorescence polarized parallel,  $I_{\parallel}(t)$ , and perpendicular,  $I_{\perp}(t)$ , with respect to the polarization vector of the excitation source. The time-resolved fluorescence anisotropy is then calculated by applying equation 8.

$$r(t) = \frac{I_{\parallel}(t) * G - I_{\perp}(t)}{I_{\parallel}(t) * G + 2 * I_{\perp}(t)} \quad (\text{eq. 8})$$

Where  $G$  is a factor that takes into account the variations in detection sensitivity between the two orthogonal polarizations. By calculating the extent of polarization of the fluorescence emission, it is possible to describe the rotational motion, the nature of the environment and energy transfer processes. Two-photon excitation can provide an improved dynamic range for fluorescence anisotropy measurements, due to the fact that the absorption process has a photoselective nature [50, 52].

### 1.7.1. The process of photoselection

When polarized light is used to excite a population of randomly oriented fluorophores, not all the molecules have the same probability to become excited. This is because fluorophores prefer to absorb photons whose electric fields are aligned to the absorption dipole of the fluorophore, therefore the molecules whose transition moment is parallel to the electric field of the polarized light source will be preferentially excited (figure 10). The fluorophores whose absorption dipole is perpendicular to the electric field of the excitation light cannot be excited. This excitation biased by the orientation of the fluorophore is termed *photoselection* [46, 48]. The selective excitation yields a partially oriented population of fluorophores which emit partially polarized fluorescent light.

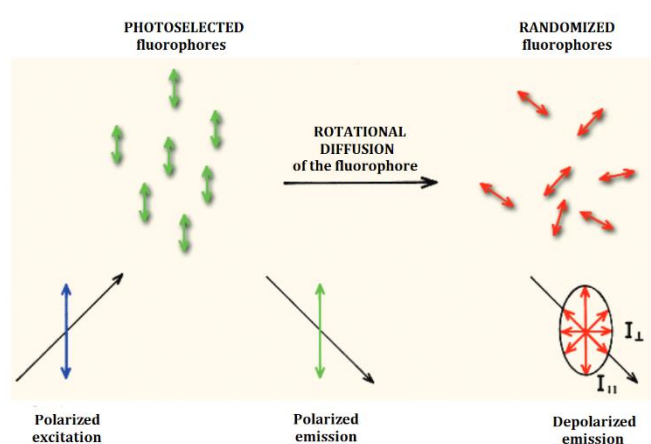


**Figure 10.** The principle of photoselection [48]

### 1.7.2. Anisotropy imaging

The experimental geometry for anisotropy imaging involves a polarizing beam splitter in the case of two-detector (simultaneous) polarization-resolved measurements or a polarizer for one-detector measurements. The main advantage of using two detectors or a polarizing beamsplitter is that the orthogonal polarization components are acquired simultaneously. This reduces the artefacts due to movement or changes in the sample, photobleaching or the drift of the instrument. Moreover, two-detector measurements are faster than the sequential acquisitions.

There are a variety of options when setting up imaging anisotropy measurements. One can perform these measurements as steady-state or time-resolved measurements, in the time-domain or frequency domain and by using either scanning or wide-field methods. When performing time-resolved measurements, an important requirement are that the excitation source is pulsed or modulated. The detection can be either modulated or based on time-gating or TSCPC [52].

# Chapter II: Materials and methods

## 2.1. Materials

Cholesterol (Corden Pharma, Switzerland), 1-palmitoyl-2-oleoyl-sn-glycero-3-phosphocholine, 1,2-dipalmitoyl-sn-glycero-3-phosphocholine (Avanti Polar Lipids), 1,2-dioleoyl-sn-glycero-3-phosphocholine (Corden Pharma, Switzerland), Chloroform (Rathburn Chemicals, UK), Sodium hydroxide (VWR Chemicals), Clorhexidine (Medic team, Denmark), Iodine solution (21.5 mg/ml, Sygehus apotekerne i Danmark), Rely+On™Virkon® (DuPont). 2-methylbutane ( $\geq 99.9\%$ ), Methanol, DMSO ( $\geq 99.9\%$ ), Glycerol Reagent Plus™, Span 60, Span 80, Tween 60, Tween 80 were purchased from Sigma Aldrich.

The fluorescent dyes used in the study are listed in table I. Detailed information about the probes can be found in Appendix II.

**Table I.** Fluorescent probes used in the study of supported bilayer membranes and skin.

<i>Probe</i>	<i>Supplier</i>
Rhodamine B	Exciton, USA
Laurdan	Thermo Fisher Scientific
Oregon Green	
ATTO647N	ATTO-TEC GmbH
Top Fluor-PC	Avanti Polar Lipids
Fluorescein	Sigma-Aldrich

Citrate buffer (pH 5.46) was prepared by mixing citric acid monohydrate 0.1 M (Sigma) with trisodium citrate dihydrate 0.1 M (Sigma) in a ratio of 2:8 and the pH was adjusted to  $\sim 5.5$  with a 1 M NaOH solution. Sodium azide (Aldrich) was added in a concentration of 0.02% to the buffer.

Phosphate buffered saline (PBS) was prepared from tablets purchased from Sigma. One tablet dissolved in 200 mL of Milli-Q water yielded 0.01 M phosphate buffer, 0.0027 M potassium chloride and 0.137 M sodium chloride, pH 7.4, at 25 °C. Sodium azide (Aldrich) was added in a concentration of 0.02% to the buffer.

HEPES buffer (0.01 M, pKa = 7.66, pH = 7 and ionic strength = 0.15 M) was prepared by mixing 0.008 mol of HEPES (4-(2-hydroxyethyl)-1-piperazineethanesulfonic acid, purchased from Sigma) with 0.0019 mol of HEPES sodium salt (basic component, purchased from Sigma) and 8.665 g NaCl with Milli-Q water, up to 1000 mL. The pH was adjusted to 7 with a 1M NaOH solution.

All other reagents used in the study were of analytical grade and commercially available.

## 2.2. Methods

### 2.2.1. Preparation of supported lipid bilayers

Supported lipid bilayers were employed as bilayer model systems. They were prepared by hydration of dry lipid films formed by the spin-coating technique as described by Simonson et al. [53] and Mennicke et al. [5].

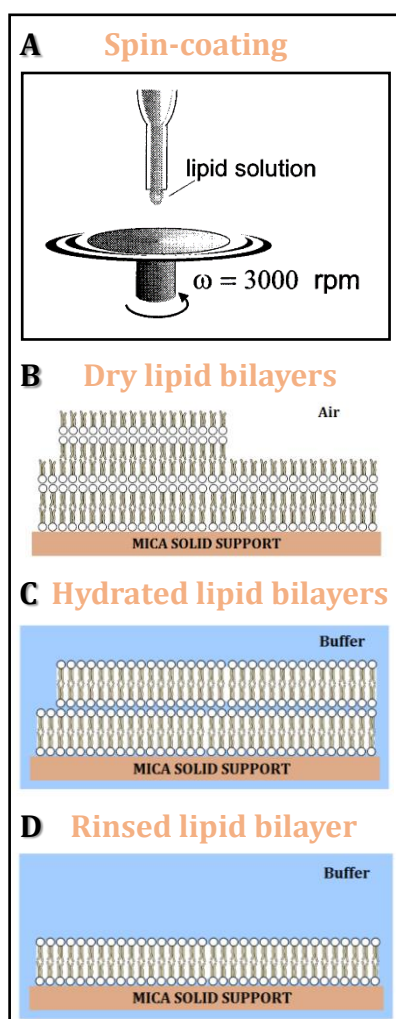


**Figure 11.** Preparation of supported lipid bilayers. Adapted from [5, 6].

In this technique, 30  $\mu\text{l}$  of a 10 mM lipid (POPC or a 25:50:25 mixture of DOPC:DPPC:CHOL) stock solution in methanol, containing the fluorescent probe(s) in a concentration of 0.5 mole% related to the lipid(s), was pipetted with a Hamiltonian syringe on a freshly cleaved slice of mica with a surface of 0.8 x 0.8 cm. This was then spun on a KW-4A spin-coater (Chemat Technology, CA, USA) at 3000 rpm for 40 s to spread the lipid solution uniformly on the mica surface (figure 11A). The coated sample was then placed under vacuum for 12 - 24 h to ensure complete evaporation of the solvents and yield dry multi-lamellar lipid films (figure 11B).

The dry films on mica were then hydrated in a commercial fluid cell for microscopy (BioCell, JPK Instruments AG, Berlin, Germany) with 2 ml HEPES buffer at 60  $^{\circ}\text{C}$  and kept above the melting point of the lipids for one hour. The hydrated lipid films (figure 11C) were afterwards carefully rinsed with HEPES buffer at 80  $^{\circ}\text{C}$  to mechanically remove the excess bilayers and leave only a single lipid bilayer on the mica substrate (figure 11D). After each flushing step, the buffer was replaced in order to remove membrane debris in suspension. The presence of a single bilayer was confirmed by fluorescence microscopy. The contrast between a hole in the bilayer and the surrounding bilayer represents the fluorescence signal of a single bilayer [6, 54, 55].

A widefield microscope (Nikon ECLIPSE Ti) with a CoolLED pE-300 white light source, a 60x WI objective and an Andor Zyla sCMOS camera was used. A green diode together with a TRITC filter were used to image the red dyes and a blue diode together with a FITC filter to image the green dyes.  $\mu\text{Manager}$  1.4.21 software [56] was used to control the microscope. The samples were carefully flipped with the membrane facing the buffer solution and microscope cell (figure 12) to avoid imaging the sample through the birefringent mica. The obtained images were analysed by using with Fiji - ImageJ [57] software.

## 2.2.2. Förster resonance energy transfer (FRET) measurements

### 2.2.2.1. Lipid bilayers

The lipid bilayers for the FRET measurements were prepared according to the method described in section 2.2.1. POPC supported lipid bilayers were used to study the FRET interaction of two types of donor-acceptor pairs:

i. The donor molecule, TopFluor-PC, was added at a concentration of 0.5 mol% to a 10 mM POPC solution that was spun-coated to form the lipid bilayer. The acceptor molecule, rhodamine-B, was added with increasing concentrations (0, 1, 10, 20, 30, 40, 50, 60  $\mu\text{M}$ ) in the buffer used to hydrate the bilayer containing the donor fluorophore. The lifetime image of the bilayer was acquired firstly in the absence of the Rhodamine-B and then at each acceptor concentration level.

The same donor-acceptor FRET pair was studied in an alternative setup, where Rhodamine-DHPE (a lipid conjugate of Rh-B) was inserted in the lipid bilayer together with the TopFluor-PC probe. Here, four supported bilayers were prepared. The first bilayer contained TopFluor-PC only while the others were composed of both TopFluor-PC and Rhodamine-DHPE. The acceptor fluorophore was added at three different concentrations in the bilayer: 0.81, 1.83 and 4.89 mol% related to the lipid.

ii. The donor molecule, ATTO488-DPPE, was added at a concentration of 0.5 mol% to the lipid mixture that was spun-coated to form the lipid bilayer. The acceptor molecule, Rhodamine-B, was added with increasing concentrations (0, 1, 10, 20,  $\mu\text{M}$ ) in the buffer used to hydrate the bilayer containing the donor. The lifetime image of the bilayer was acquired firstly in the absence of the Rhodamine-B and then at each acceptor concentration level.

### 2.2.2.2. Human skin

Skin samples obtained from abdominoplasty operations were sliced and labelled with different concentrations of both TopFluor-PC (FRET donor) and Rhodamine-B (FRET acceptor) by using the protocol described in Appendix xy. A total number of 12 skin slices from the same donor were labelled according to table II.

**Table II.** Skin labelling for the FRET experiments.

Doubly labelled skin samples	Rhodamine-B 0 $\mu\text{M}$ (donor only)	Rhodamine-B 10 $\mu\text{M}$	Rhodamine-B 20 $\mu\text{M}$	Rhodamine-B 30 $\mu\text{M}$
TopFluor 1.75 $\mu\text{M}$	✓	✓	✓	✓
TopFluor 3.5 $\mu\text{M}$	✓	✓	✓	✓
TopFluor 7 $\mu\text{M}$	✓	✓	✓	✓

FLIM images of 6 different areas of each labelled skin slice were acquired as described in section 2.2.3.

### 2.2.3. FLIM setup for FRET studies

The fluorescence lifetime imaging microscopy (FLIM)/ Förster resonance electron transfer (FRET) measurements for both the lipid bilayers and skin samples were carried out on a custom built multiphoton excitation microscope based on a Nikon TI Eclipse microscope equipped with a Mai Tai DeepSee Ti:Sapphire femto-pulsed laser. The samples were excited at 920 nm, a two-photon cross-section where the donor fluorophore (ATTO488-DPPE or TopFluor-PC) is excited well, with minimized direct excitation of the acceptor fluorophore (see two-photon cross-sections in Appendix II). The same laser power (30%) was used for all the experiments. A 60x WI objective was used. The microscope was controlled with the software Micromanager [56].

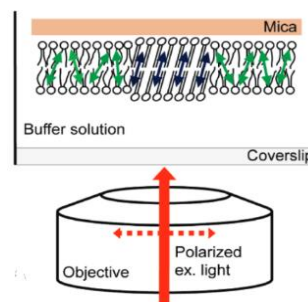


**Figure 12.** Experimental configuration for microscopy studies [4]

The detection was done by using hybrid photo detectors (HPDs) and a SPC-150 TCSPC module from Becker & Hickl GmbH or by h7422p Photomultiplier tubes (PMTs) (Hamamatsu) and using a FastFLIM board from ISS (frequency 80 MHz). The gain of the detectors was set to constant throughout the experiments.

The system was calibrated at the beginning of each experiment. This was done with a fluorescein 5  $\mu\text{M}$  solution in ammonium acetate, whose lifetime is known to be 4.0 ns, and rhodamine-B 20  $\mu\text{M}$  solution in water, with a lifetime of 1.7 ns [58]. The lifetimes of the standard solutions were verified again at the end of each experiment.

Image acquisition was performed with the SPC image software when using the SPC-150 TCSPC Module or with the ISS software when using the FastFLIM board from ISS. Images were acquired with enough pixels to comply with the Nyquist criteria [59], with a 20  $\mu\text{s}$  pixel dwell time and an averaging of 20 frames. The decay matrix and lifetime of each pixel in the sample was acquired to form the FLIM image. Areas of about 50x50  $\mu\text{m}$  were measured in the skin or the lipid bilayers.

The FLIM data was analysed using the phasor approach in the SimFCS software, where each pixel of the FLIM image is transformed into a pixel on the phasor plot. The FRET efficiency was measured by using the FRET calculator in SimFCS [60].

### 2.2.4. Fluorescence anisotropy measurements

#### 2.2.4.1. Steady-state fluorescence anisotropy

The steady-state fluorescence anisotropy was measured on the same microscope used for the FLIM measurements. The samples were excited at a two-photon cross section of 840 nm for the samples containing Rhodamine-B and a cross section of 880 nm for the samples containing Oregon Green® 488-DHPE. A polarizer was used to split the parallel emission light from the perpendicular emission light. The light from each plane was

detected with the help of two PMT detectors. The detector gains were adjusted by analysing a Rhodamine-B solution in water, where the fluorescence anisotropy is equal to 0.

Two types of samples were analysed using this method. Firstly, the anisotropy of a series of solutions of Rhodamine-B with increasing concentrations of glycerol in water (0%, 25%, 50%, 75%) or glycerol 100% were investigated. Secondly, domain-forming supported bilayers were analysed. They were composed of a mixture of DOPC:DPPC:CHOL 25:50:25 in which 0.5 mol% Oregon Green® 488-DHPE was added.

#### 2.2.4.2. Time-resolved two-photon fluorescence anisotropy

The time-resolved fluorescence anisotropy studies were performed on a custom-built system similar to the one used for the steady-state anisotropy and FLIM measurements, but employing a Glan-Taylor polarizer to split the light between the hybrid detectors (HPDs). A scheme of the setup is represented in figure 13. The relative intensities of the detectors were calibrated by using an aqueous solution of 4  $\mu\text{M}$  rhodamine-B. A Nikon objective with a 100x magnification and a numerical aperture of 1.4 was used.

The anisotropy at each time point was calculated using equation 9.

$$r(t) = \frac{I_{\parallel}(t) - I_{\perp}(t)}{I(t)} \quad (\text{eq. 9})$$

with  $I_{\parallel}(t)$  representing the fluorescence intensity at the detector with polarization parallel to the polarization of the excitation beam,  $I_{\perp}(t)$  the fluorescence intensity for the detector with perpendicular polarization with respect to the polarization of the excitation source and  $I(t)$  the total fluorescence intensity at the two detectors.

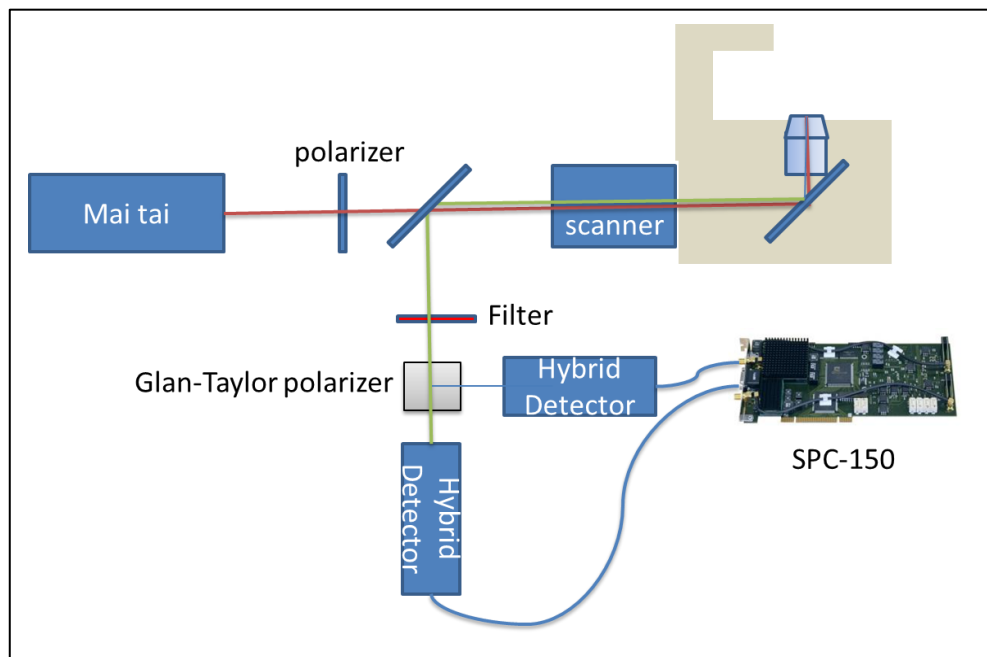


**Figure 13.** Schematic presentation of the setup used for the time-resolved fluorescence anisotropy studies.

#### 2.2.5. Preparation of skin samples for the FRET and diffusion experiments

Fresh human skin was provided from plastic surgeries at Odense University Hospital, Odense, Denmark. The experiments performed in this project involving the use of human tissue were approved by the Regional Research Ethics Committee of Southern Denmark and were adherent to the Declaration of Helsinki Principles (2008). No informed consent from patients was obtained (Danish regulations consider human tissue left over from surgery as discarded material), and no personal data were collected except the sex and age of the patient.

The skin was wiped with colour-free iodine-alcohol prior to surgery and the excised skin was stored at 4°C in a sealed plastic bag for a maximum of 16 h. Subcutaneous fat was trimmed away, tissue within 2 cm from the cut was discarded and remaining tissue was rinsed with tap water and patted dry on the surface. For the FLIM/FRET experiments, the skin was cut into pieces of ca. 1 cm<sup>2</sup>. Liquid nitrogen was used for the cryo-fixation of the skin pieces and the frozen skin samples were stored at – 80 °C until use.

#### 2.2.6. Preparation of non-ionic surfactant nano-vesicles

Both fluorescent dye-loaded and non-loaded niosome suspension were prepared by the thin-film hydration method, followed by extrusion through polycarbonate filters. The niosome formulations (table III) were composed of different ratios of surfactants. Accurately weighed quantities of surfactants (Tween 60/80 and Span 60/80), Laurdan (for the loaded niosomes) and cholesterol were dissolved in 5 ml chloroform in a 250 ml round-bottom (RB) flask. The chloroform was evaporated at 60 °C under reduced pressure using a rotary flask evaporator (Büchi Rotavapor R-210, Switzerland). The pressure in the flask was kept at 500 mBar for 5 minutes, then it was reduced to 200 mBar for 15-20 minutes until the solution got viscous. The rotation speed was also increased gradually from 3 in the equilibration phase to maximum speed when the solution got viscous. The vacuum strength was then decreased to about 80 mBar until the exhaustive evaporation of the solvent could be seen. The solvent evaporation was followed by vacuum drying at 25 °C to obtain a dry film.

The thin films were hydrated with 5 ml of Rhodamine B solution in citrate buffer pH 5.46, preserved with 0.02% sodium azide. For the non-loaded niosomes, the films were hydrated with preserved citrate buffer without fluorescent dye. The RB flasks were gently shaken in a water bath at 60°C for the first 30 minutes and then attached to the rotavapor and left rotating overnight, at low rotation speed and ambient temperature.

After hydration, the formulations were extruded through Whatman polycarbonate filters at 60 °C and 20 bar. Each formulation was passed 5 times through stacks of two membranes with a pore size of 400 nm, 200 nm and 100 nm filters, consecutively. A 800 nm filter was additionally used for the non-loaded formulations.

Figure 14 summarizes the preparation steps used for the niosome formulations.

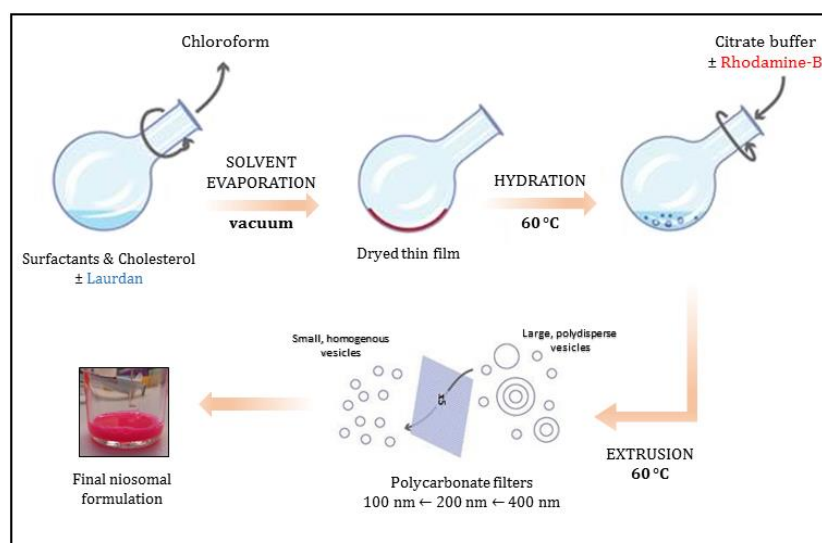


**Figure 14.** Preparation of niosomes by the thin film hydration method, followed by extrusion. Adapted from [61].

A total number of nine formulations was prepared, out of which six were based on Span 60/Tween 60 (named Nio60) and three were based on Span 80/Tween 80 (named Nio80) with different ratios of Span and Tween (table III). Four of the formulations were loaded with the red hydrophilic dye rhodamine B (rhB) and the blue lipophilic dye Laurdan. The loaded formulations are marked with “-FL” in their name.

## 2.2.7. Niosome characterization

### 2.2.7.1. Optical microscopy

Microscopic images of the non-loaded formulations before and after extrusion through the 800 nm filter were taken by using a bright field microscope (Nikon ECLIPSE Ti), with a 60x WI objective and a Andor Zyla sCMOS camera.

### 2.2.7.2. Laser scanning confocal microscopy

Laser scanning confocal microscopy (LSCM; Zeiss LSM 510 laser scanning confocal microscope) was used to image the non-extruded niosomal formulations doubly-loaded with fluorescent dyes. The samples were excited by a Mai Tai DeepSee Ti:Sapphire femto-pulsed laser at a cross-section of 780 nm, where both Rhodamine-B and Laurdan are excited (see two-photon cross-sections in Appendix II). The laser power was set to 30% in all experiments. A C-apochromat 63x/1.2 WI corr objective was used. A band-pass 390-465 filter was used to image Laurdan and a BP 565-615 for Rhodamine-B. The pinholes were held constant opening of 1000  $\mu\text{m}$  for both channels. The image acquisition was done with the Zeiss LSM image browser software. The image size was 636x636  $\mu\text{m}$ , pixel time: 2.06  $\mu\text{s}$ , averaging: 16 images.

The LCSM images were analysed by using the Fiji-Image J software.

**Table III.** Composition of the niosomal formulations.

#	Formulation code	Surfactant molar ratio (Span:Tween)	Span 60/80 (mM)	Tween 60/80 (mM)	Chol (mM)	Rh-B (mM)	Laurdan (mM)
1	Nio60-a	Span 60	80	-	20		
2	Nio60-b	9:1 Span 60 : Tween 60	72	8	20	-	-
3	Nio60-c	8:2 Span 60 : Tween 60	64	16	20	-	-
4	Nio60-d	7:3 Span 60 : Tween 60	56	24	20	-	-
5	Nio60-d-FL	7:3 Span 60 : Tween 60	56	24	20	0.4	0.2
6	Nio60-e-FL	5:5 Span 60 : Tween 60	40	40	20	0.4	0.2
7	Nio80-d	7:3 Span 80 : Tween 80	56	24	20	-	-
8	Nio80-d-FL	7:3 Span 80 : Tween 80	56	24	20	0.4	0.2
9	Nio80-e-FL	5:5 Span 80 : Tween 80	40	40	20	0.4	0.2

### 2.2.7.3. Particle size (Dynamic light scattering)

The mean particle size and polydispersity index (PDI) of both non-extruded and extruded samples (after each extrusion step) were analysed by dynamic light scattering (DLS, DelsaMax Pro, Beckman Coulter). The analysis was carried out after adequate dilution (1:100) of the sample with citrate buffer (pH 5.46, 0.2% sodium azide) in a plastic cuvette. Each measurement was performed at 25 °C with 6 consecutive acquisitions over 10 s each. The mean particle size (z-average) and PDI were calculated by the instruments cumulant analysis. The PDI was used as an indicator for particle size distribution. The size and PDI results were expressed as the average value of at least triplicate (n=3) with standard deviation.

The physical stability of the niosomes was evaluated by analysing changes in particle size and PDI over time. A stability plan was designed for selected formulation, where the size and PDI were measured at day 1 and day 30 after the preparation and storage at 25 °C.

#### 2.2.7.4. Entrapment efficiency

Four formulations containing the fluorescence dyes were selected to be evaluated concerning the entrapment efficiency. For the evaluation of the entrapment efficiency of Rhodamine B, the niosomes were separated from the free dye by using spin column chromatography. Sephadex® G-25 spin columns were prepared in 1 ml insulin syringes. Biogel A 1,5 m (producer) was packed into the syringes by centrifugation (700 rpm, 1 minute) to a final volume of about 900 µl. Care was taken to avoid inclusion of air bubbles in the gel structure. The syringes were then inserted into plastic centrifugation tubes of appropriate size. The columns were equilibrated with 200 µl and subsequently 3 times 50 µl of the elution buffer (citrate buffer pH=5.46, preserved with 0.2% sodium azide) with centrifugation steps in between (30 seconds, 700 rpm).

200 µl of niosomal formulation was loaded onto each column and the column was centrifuged for 1 minute at 700 rpm. The sample was exhaustively eluted by repeating the following steps: a) Add 50 µL elution buffer. b) Spin 30 seconds at 700 rpm. c) Collect fraction into a 0.5 mL Eppendorf tube. Collection of sample fractions was done in 0.5 mL Eppendorf tubes. A total amount of 12 fractions was collected for each eluted sample.

To quantify the non-entrapped rhodamine B (free dye), the fractions (fraction 6-12) were analysed both independently and combined using a FLUOStar Omega plate reader (BMG Labtech). An excitation filter of 550 ± 10 nm and an emission filter of 590 ± 10 nm was used, and the detector gain was set to 500. A black Nunc 96 (VWR, Denmark) plate was used. A rhodamine-B in citrate buffer pH 5.46 solution was used to measure a calibration curve for the concentration range 1-6 µM (see Appendix).

The Rhodamine-B entrapment efficiency (EE%) was calculated by using equation 11:

$$EE\% = \frac{(W_{RhB \text{ initial}} - W_{RhB \text{ free}})}{W_{RhB \text{ initial}}} \times 100\% \quad (\text{eq. 11})$$

Where  $W_{RhB \text{ initial}}$  is the theoretical mass of rhodamine-B in the 200 µL niosomal formulation that was added on the column and  $W_{RhB \text{ free}}$  is the amount of free Rhodamine-B in the formulation.

#### 2.2.8. Ex vivo skin permeation study

The *ex vivo* drug permeation studies were performed according to the OECD guidelines for skin absorption studies [62] on a multi-station cell system with 10 Franz diffusion cells (SES GmbH Analysesysteme, Germany) with a diameter of 20 mm and a 15 ml receptor volume (figure 15, adapted from [1]).

### 2.2.8.1. Skin preparation and handling

All the human skin samples used in the experiment were obtained, as described in section 2.2.5., from the same patient (female, 56 years old) and same body area (upper arm). Seven skin samples with a diameter of 3.5 cm were punched out with the help of a sterile metal mould and a hammer.

Two of the skin samples were treated (sample 6 and 7 in table IV) with a derma roller (DRS®) figure 16 A, a microneedle device with 720 needles of 1 mm length. The device, previously disinfected with Virkon disinfection agent (supplier), was rolled five times in four directions over the skin surface, as depicted in figure 16 B.

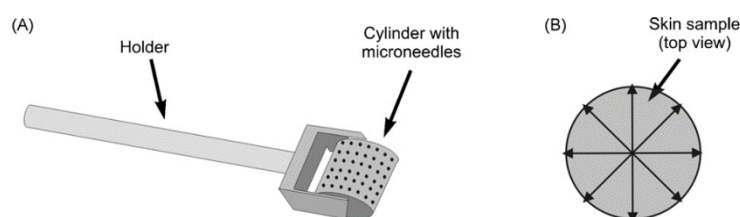


**Figure 16.** A) Schematic presentation of the microneedle device. B) Directions of application of the microneedle device on the skin [16].

Both the skin treated with the dermaroller and the normal skin was placed on a filter paper (Whatman, 90 mm Ø) wetted with PBS and used immediately for the *in vitro* diffusion experiment.

### 2.2.8.2. Ex vivo diffusion experiment

The skin sections were mounted on the Franz cells with nominal surface areas of 3.14 cm<sup>2</sup>. The epidermal side of the skin was exposed to ambient conditions, while the dermal side was bathed by phosphate buffer saline (PBS), pH 7.41. The receptor fluid was mixed with a magnetic stirring bar at 300 rpm and was kept at 32 °C by a thermostat. All air bubbles were carefully removed below the skin by carefully tilting the chamber and directing the air bubbles out through the lateral sampling port.

80 µl/cm<sup>2</sup> of niosomal formulation or control were applied with the help of a micropipette. The formulations used for the permeation experiments are summarized in table IV. All experiments were carried out with non-occluded donor compartments.

Permeation (analysis of receptor)

After 24 h, 1 ml aliquots from the receptor media of each diffusion cell were collected and the diffusion setup was dismantled. All the equipment and surfaces were disinfected with ethanol disinfection tissues and Virkon disinfection solution.

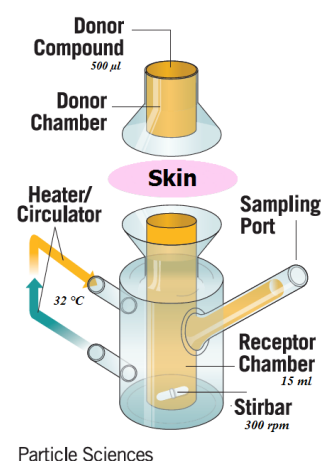


**Figure 15.** Components of a Franz diffusion cell [1]

The amount of fluorescent dye in the collected aliquots was quantified using a FLUOStar Omega plate reader (BMG Labtech). The aliquots were filtered through 0.22  $\mu\text{m}$  filters before analysis. An excitation filter of  $550 \pm 10$  nm and an emission filter of  $590 \pm 10$  nm was used, and the detector gain was set to 500. A black Nunc 96 (VWR, Denmark) plate was used.

**Table IV.** Controls and test samples in the *ex vivo* skin diffusion experiment.

#	Sample type	Sample	Penetration enhancer	
			Nano-carrier	Physical
1	Blank	Untreated skin	-	-
2	Control	rhodamine B 400 $\mu\text{M}$ in citrate buffer, pH 5.46	-	-
3	Control	Laurdan 200 $\mu\text{M}$ in DMSO	-	-
4	Test dyes outside niosomes	Nio80-d + Rhodamine B 400 $\mu\text{M}$ + Laurdan 200 $\mu\text{M}$	Non-loaded niosomes	-
5	Test dyes inside + outside niosomes	Nio80-d-FL	Fluorescent dye-loaded niosomes	-
6	Test dyes inside + outside niosomes	Nio80-d-FL on punctured skin	Fluorescent dye-loaded niosomes	Microneedle device
7	Test dyes inside + outside niosomes	Nio80-e-FL	Fluorescent dye-loaded niosomes	-
8	Test dyes inside + outside niosomes	Nio80-e-FL on punctured skin	Fluorescent dye-loaded niosomes	Microneedle device

### 2.2.8.3. Preparation of skin for imaging

Immediately after the diffusion experiment, the skin tissues were tapped with a clean paper tissue to remove the remaining formulation and pieces of  $\sim 0.5$  cm x 0.5 cm were carefully cut with a sterile cutter from the areas where the formulations were in contact with the skin. The cut samples were introduced into small open containers made of aluminium foil and covered completely with Tissue-tek™ mounting medium for cryotomy (Sakura, Copenhagen, Denmark). The skin was cryopreserved by immersing the samples into 2-methylbutane cooled by liquid nitrogen for 60 seconds. The samples were then immediately placed on dry ice followed by storage at  $-80$  °C until use.

One day before the imaging experiment, the samples were cut into 20  $\mu\text{m}$  slices (cross-sections) using a cryotome (Cryotome FSE, Thermo Scientific, Denmark) and transferred to SuperFrost®Plus microscope slides (VWR, Denmark). The skin samples were mounted with Prolong®Gold antifade reagent (Life Technologies, USA) and cover slips (# 1.5) and left overnight at 4 °C to harden the mounting media.

#### 2.2.8.4. Confocal laser scanning microscopy

Four slices from two different areas of each skin sample exposed to the skin diffusion experiment were imaged using LCSM with the same setting as used as for the LCSM imaging of the non-extruded niosomes (section 2.2.7.2.). As the aim of the experiment was to obtain quantitative information and to compare the different samples, detector gains were held constant at 621 for the red channel and 798 for the blue channel throughout imaging of all samples.

For each skin slice, images were taken of at least three different areas in each skin sample resulting from the diffusion experiment. The average fluorescence intensity and histograms were analysed using the Fiji-Image J software. This was done by analysing at least 9 polygonal selections of areas representing epidermis, dermis and background. An example of a polygonal selection for the epidermis area is shown in figure 17.

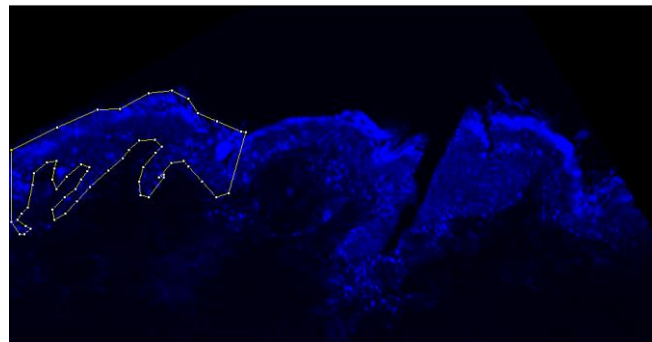


**Figure 17.** Polygonal selections in Image J for the semi-quantitative evaluation of fluorescent dyes accumulated in skin tissue.

The background in each polygon was subtracted using equation 12:

$$I_{\text{TOTAL CORR}} = I_{\text{TOTAL}} - (P_{\text{area}} \times I_{\text{BACKGROUND}}) \quad (\text{eq. 12})$$

Where  $I_{\text{TOTAL CORR}}$  is the corrected integrated intensity in the polygonal selection;  $I_{\text{TOTAL}}$  is the integrated intensity of the selection;  $P_{\text{area}}$  is the number of pixels (area) of the polygonal selection;  $I_{\text{BACKGROUND}}$  is the average intensity of one polygonal selection in the background area of the same image.

# Chapter III: Results and discussion

## 3.1. FLIM/FRET studies

### 3.1.1. Förster resonance electron transfer (FRET) in POPC supported bilayers

POPC supported bilayers were used as a simple model system to compare with the FRET studies in human skin. Studies on more simple systems can help us gain a better understanding of the interactions and proximity of fluorophores that work as FRET donor-acceptor pairs. The FRET donor molecule studied was TopFluor-PC, a green dye which is attached to one of the lipid tails of the phosphatidylcholine lipid (structure in Appendix II). The donor was incorporated into the POPC lipid bilayer prepared by the spin-coating technique described in the methods section 2.2.1. The acceptor molecule was rhodamine B (structure in Appendix II), a hydrophilic red dye which was added at increasing concentrations in the hydration buffer of the donor-containing bilayer.

Firstly, FLIM images were recorded for the bilayer containing donor only in order to measure the lifetime of the donor when no FRET is occurring. Afterwards, successive images containing FLIM data for each pixel were captured each time more Rhodamine-B was added to the hydration buffer to increase its concentration from 0  $\mu\text{M}$  to 1  $\mu\text{M}$ , 10  $\mu\text{M}$ , 20  $\mu\text{M}$ , 30  $\mu\text{M}$ , 40  $\mu\text{M}$ , 50  $\mu\text{M}$  and 60  $\mu\text{M}$ .

Six images were taken for each concentration level from different areas of the labelled POPC bilayer. The recorded images were loaded into the simFCS software which has a FLIM analysis function. In this software, the lifetime information of each pixels is transferred to a mathematical space called the phasor space. The phasor space is a vector representation of the lifetime data which shows a global representation of the fluorescence decay in an image by transforming the histogram of time decays in each pixel into a phasor. The phasor of each pixel are plotted in a universal plot denoted the phasor diagram. Each phasor position in the plot is characteristic of a molecular species and its local environment [63]. In the phasor diagram (shown in figure 18 A) the pixels from the FLIM images are clustered together according to their lifetimes on the universal circle of the phasor diagram, which has values from 0 (left) to 1 (right). In this way, populations of pixels with individual lifetimes will be positioned together on the plot and single exponential lifetimes can be resolved.

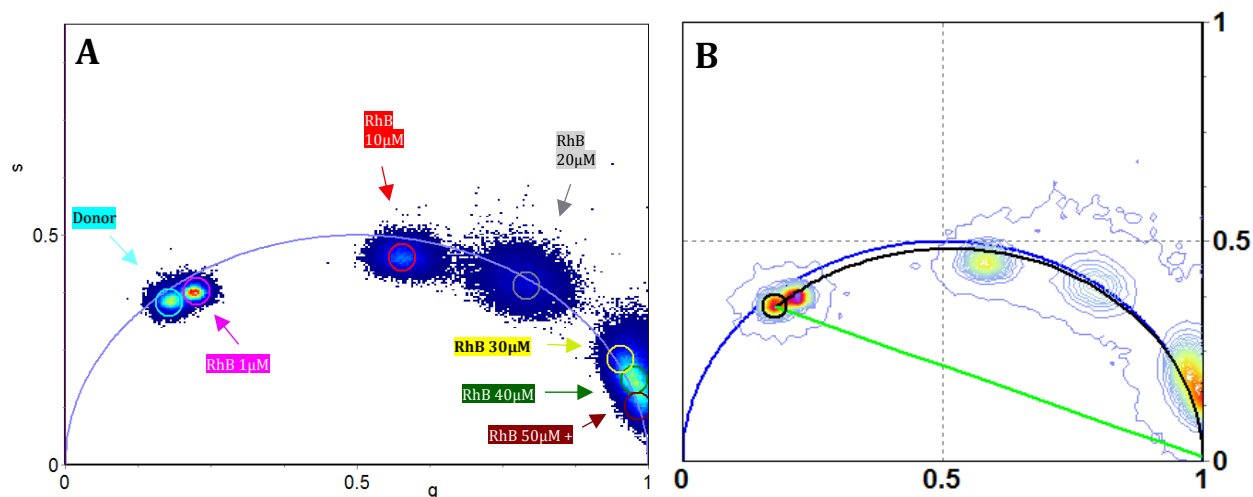


**Figure 18.** Phasor-plot analysis of the FLIM data obtained for POPC supported bilayers labelled with TopFluor-PC 0.5 mole% and with increasing concentrations of Rhodamine-B in the hydration buffer. Each point on the phasor plot represents one pixel of the images in figure 19, and is positioned on the plot according to its lifetime. The points on the plot represent only the lifetimes of the TopFluor donor molecule.

**Table V.** Changes in the donor lifetime, FRET efficiency and average distance between the donor-acceptor pair TopFluor-PC – Rhodamine-B when increasing concentrations of acceptor are added.  $R_0$  represents the Förster radius of the pair and it has been theoretically calculated by a previous student in our group to be 5.8 nm [64].

<i>Rhodamine-B</i> $\mu M$	<i>Top Fluor lifetime</i> <i>ns</i>		$E_{FRET}$	$R_0$ <i>nm</i>	<i>Average distance</i> <i>nm</i>
	<b>T<sub>m</sub></b>	<b>T<sub>φ</sub></b>			
0	4.83	4.11	-	5.8	-
1	4.23	3.46	0.101	5.8	8.3
10	2.05	1.57	0.619	5.8	5.3
20	1.04	0.78	0.766	5.8	4.7
30	0.58	0.40	0.894	5.8	4.0
40	0.44	0.32	0.913	5.8	3.9
50	0.41	0.28	0.915	5.8	3.9
60	0.37	0.26	0.915	5.8	3.9

The FRET calculator in simFCS fits all the experimental points on the phasor plot on a black line that represents the FRET trajectory, as shown in figure 18. The figure shows data for POPC membranes with donor TopFluor and increasing concentrations of the acceptor rhodamine B. The calculator helps to determine the FRET efficiencies by fitting the differences in lifetimes between the population of pixels that represents the sample where there is no FRET (donor only sample) and the ones that represent the samples where FRET has occurred. As the donor molecule transfers energy through FRET to the acceptor molecule, it will lose fluorescence faster so its lifetime will decrease. The more efficient the FRET transfer is, as the acceptor and donor molecules get closer together in

space, the lower the lifetime be and the experimental points will be moved on the right of the phasor plot in figure 18B.

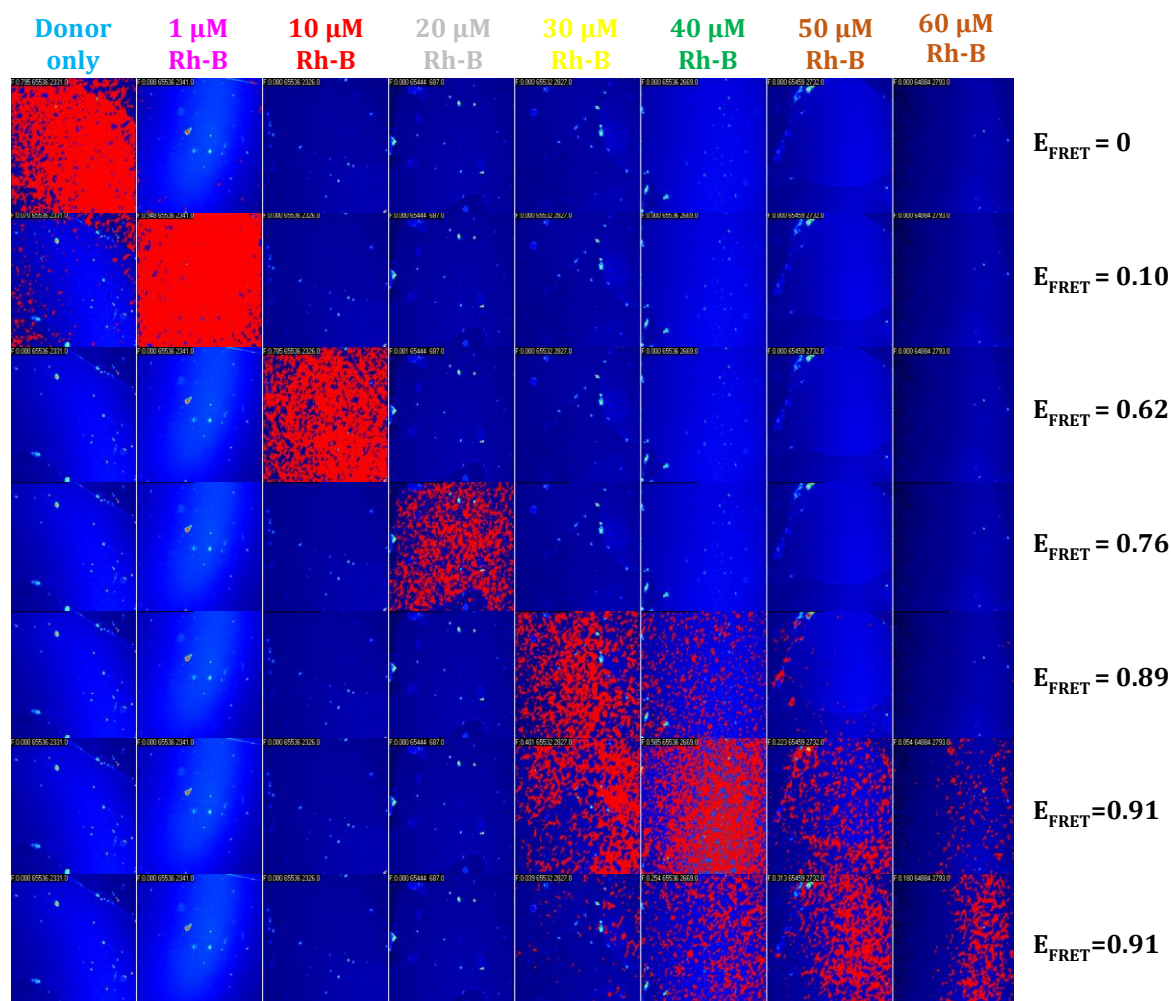


**Figure 19.** Intensity images of POPC supported bilayers labelled with TopFluor-PC 0.5 mole% and with increasing concentrations of Rhodamine-B in the hydration buffer. **One** of a total of 6 images acquired for each concentration level is shown. The highlighted red pixels show the areas with the  $E_{\text{FRET}}$  measured on the phasor plot in figure 18.

Table V summarizes the lifetimes recorded for the donor molecule and the FRET efficiencies calculated for each concentration level. As a frequency domain method was used for the FLIM imaging, two different lifetimes were obtained. One is the modulation lifetime ( $T_m$ ) and the other one is the phase lifetime ( $T_\phi$ ). The fact that they have different values is a sign of multi-exponential lifetime decays in the samples. This explains also the fact that the pixel populations are not aligned perfectly on the phasor plot in figure 18 A.

Figure 19 shows which areas in the bilayer have the FRET efficiencies calculated with the help of the phasor plot in figure 18. It can be observed that the FRET efficiency increases abruptly at lower rhodamine B concentrations and reaches a plateau at a concentration of  $\sim 30\mu\text{M}$ . Over this rhodamine B concentration, the FRET efficiency stops being homogeneous throughout the lipid bilayer.

By using the obtained FRET efficiencies and the Förster radius - which is typical for each donor-acceptor pair in a defined environment -, the average distance separating the donor and acceptor molecules at each concentration step was calculated. The efficiency of the FRET process ( $E_{FRET}$ ) depends on the sixth power of the distance between the donor and acceptor in the pair, according to the equation 13 which gives equation 14.

$$E_{FRET} = \frac{R_0^6}{(R_0^6 + R^6)} \quad [48] \quad (\text{eq. 13})$$

$$R = \sqrt[6]{\left(\frac{1}{E} - 1\right)} * R_0 \quad (\text{eq. 14})$$

It is expected to see an increase in FRET efficiency once there is more available acceptor to interact with the donor. This effect has been as well described by Lunz et al [65],

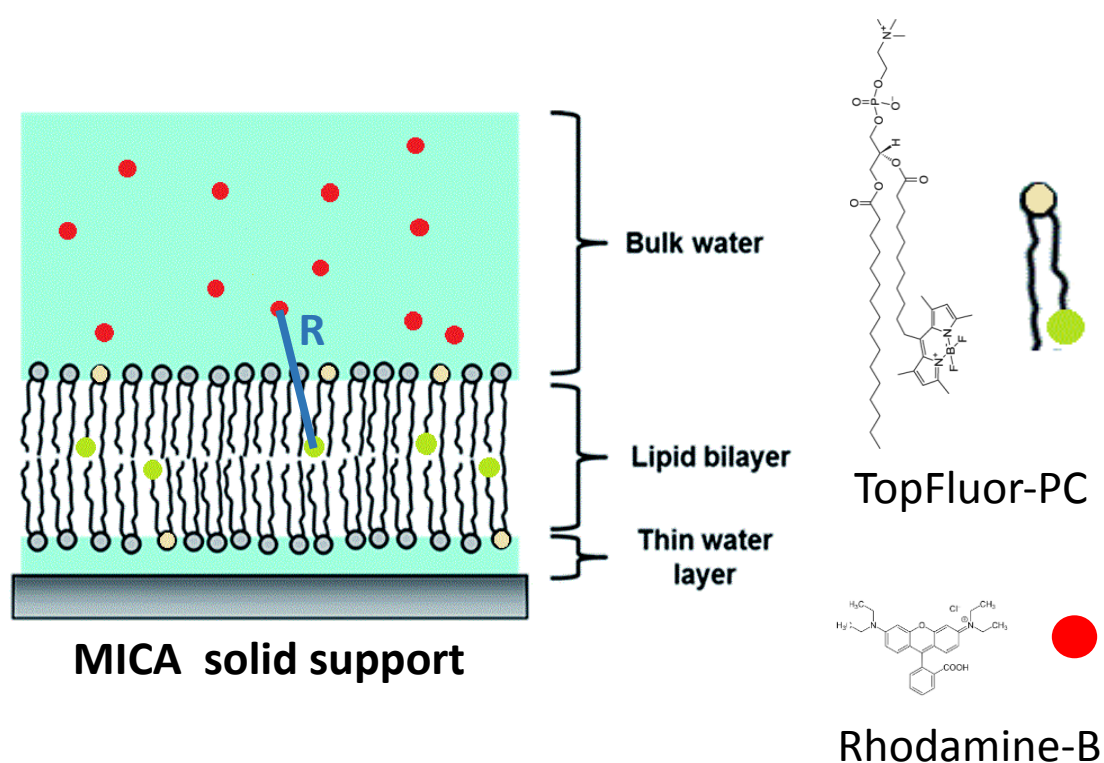


**Figure 20.** The donor and acceptor molecules of a FRET system in a POPC supported membrane. The red dots represent the Rhodamine-B molecules which are randomly distributed in the hydration buffer. TopFluor-PC will be included in the double bilayer of the supported membrane. The lipids in the membrane are represented by POPC.  $R$  is the average distance between the donor-acceptor pair. The bilayer model was adapted from [66].

Figure 20 represents a proposed distribution of the fluorescent dyes in our system based on their physico-chemical properties. Rhodamine-B is a small hydrophilic molecule which has a water solubility of 1 mg/mL [67]. Since it is soluble in the PBS buffer used for the membrane hydration, it will be distributed randomly throughout the buffer and it can interact only with the head groups of the lipids in the membrane.

TopFluor-PC is a lipid dye which will be incorporated in the lipid bilayer due to its hydrophobic nature. Kay et al. has demonstrated by using fluorescence quenching methods that the TopFluor label is buried in the hydrophobic bilayer and will sit at a 19.6 Å distance from the bilayer centre [68]. A smaller distance from the bilayer centre (15 Å) has been obtained in molecular dynamics studies by Song et al. [69].

One proposed mechanism for the observed effect is: as the number of molecules of Rhodamine-B in the hydration buffer increases, the probability of having a Rhodamine-B molecule in the proximity of a TopFluor molecule increases as well, therefore we should get a smaller average distance between the molecules, which translates into a higher FRET efficiency. At a very high concentration of the acceptor, the bilayer surface becomes saturated with the acceptor, so there always is an acceptor molecule in very close proximity of the TopFluor molecules. As the TopFluor label is buried in the membrane, the direct interaction between the two labels becomes spatially hindered and the FRET efficiency reaches a maximum which is determined by how close the acceptor and donor can get.

### 3.1.2. Förster resonance energy transfer (FRET) in human skin

The same study performed for the supported bilayers was employed in human skin to detect the diffusion route of the dyes in the complex environment created by the tissue. Skin slices were labelled successively with the lipid dye TopFluor-PC followed by the hydrophilic dye Rhodamine-B, as described in the methods section, and then imaged and analysed the same way as the POPC supported bilayers.

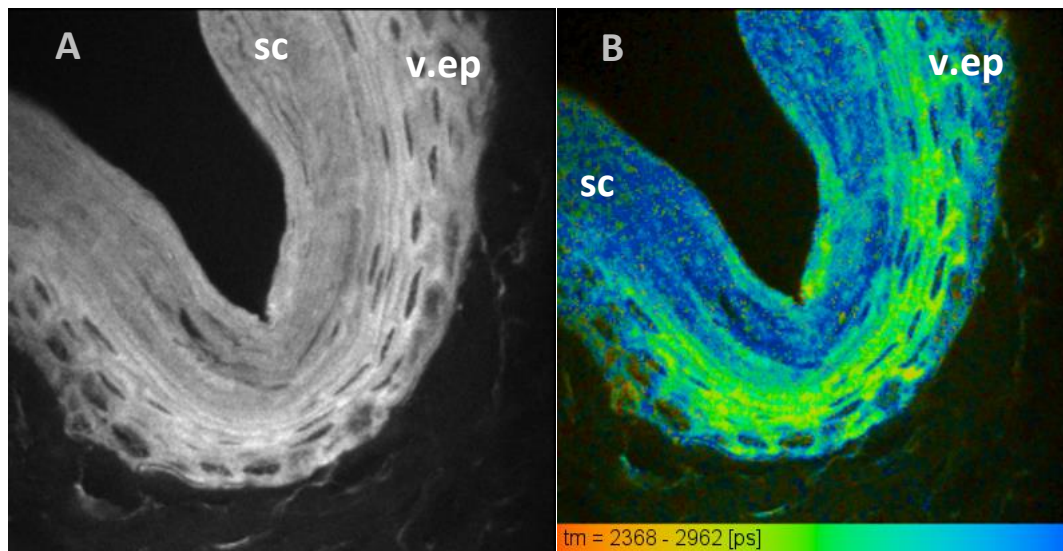


**Figure 21.** **A:** Intensity image of a 20 µm thick human skin slice labelled with 7 µM TopFluor-PC and 10 µM Rhodamine-B; **B:** Corresponding lifetime image of the same skin slice. sc = stratum corneum; v.ep.= viable epidermis. Courtesy to Jonathan Brewer for recording these images.

The intensity image of the labelled skin slice (figure 21 A) shows that the epidermis has been successfully labelled with TopFluor-PC. The stratum corneum (sc) appears to be relatively uniformly stained. The viable epidermis (v.ep) appears to be labelled predominantly in the extracellular matrix and less in the keratinocytes. Figure 21 B represents the corresponding lifetime image, where a lifetime of between 2.2 and 2.9 ns was detected for TopFluor-PC. It can be easily noticed that TopFluor has lower lifetimes in the sc (lifetime around 2.2 ns, blue area) than in the viable epidermis (lifetime around 2.9 ns, green area).

The lifetimes of TopFluor-PC were also measured in the skin sample where no acceptor is present and here they also proved to be different. In the viable epidermis, TopFluor had a lifetime of about 4.58 ns whereas in the the SC is was around 3.73 ns.

Figure 22 presents intensity images of epidermis labelled with an increased concentration of Rhodamine-B. It can be observed that the FRET transfer efficiency ( $E_{\text{FRET}}$ ) increases gradually from 0 in the samples when only TopFluor-PC is present (column A) to a maximum FRET efficiency of 0.78 for the sample where the skin was labelled with 30 and 50  $\mu\text{M}$  rhodamine-B. It is interesting to notice that for the samples with lower rhodamine-B concentration, the FRET efficiency grows abruptly and relatively homogeneous FRET efficiencies are noticed throughout the samples (columns A, B, C in figure 22). At concentrations of 30  $\mu\text{M}$  and higher, the FRET efficiency seems to not depend on the concentrations. Moreover, there seems to be a lack in the homogeneity of the FRET effects throughout the stratum corneum of the same sample, with a interval of FRET efficiencies between 0.68 and 0.78 for both the 30  $\mu\text{M}$  and the 50  $\mu\text{M}$  samples (columns D and E in figure 22).

These values of the FRET efficiencies were used to calculate the average distances between the donor and acceptor for each concentration step.

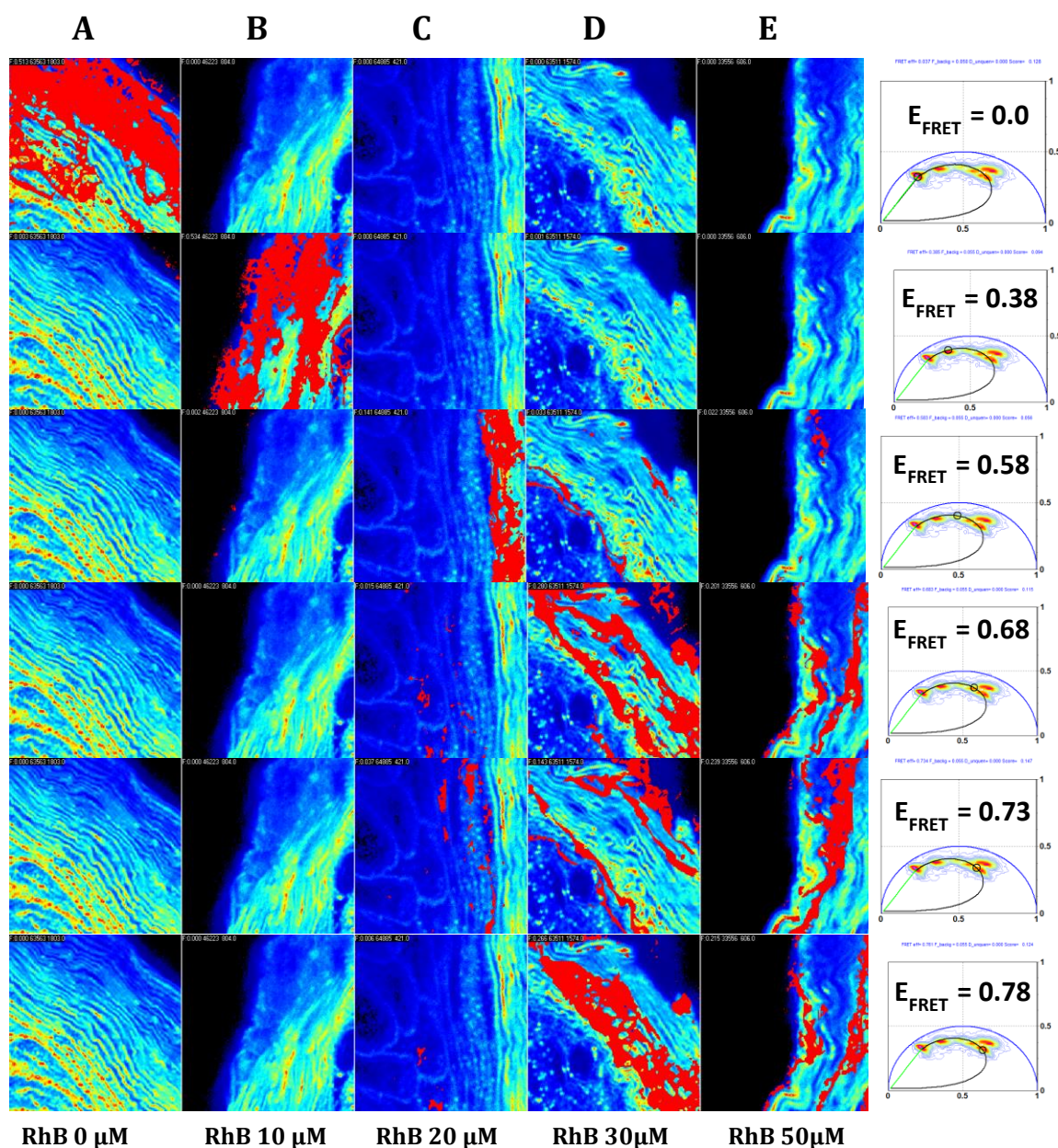


**Figure 22.** Intensity images of human epidermis labelled with: Column **A**: 7  $\mu\text{M}$  TopFluor-PC. Columns **B**, **C**, **D**, **E**: 7  $\mu\text{M}$  TopFluor-PC and 10  $\mu\text{M}$ , 20  $\mu\text{M}$ , 30  $\mu\text{M}$  and 50  $\mu\text{M}$  rhodamine B, respectively. The red highlight maps the pixels in the image which have the  $E_{\text{FRET}}$  measured on the phasor diagram on the right.

The FRET efficiencies and distances obtained in this experiment are present in table VI. By comparing the data obtained from a duplicate experiment on different skin samples (images in figure S4 in appendix III, FRET efficiencies in table VI), it can be observed there is a lack of consistency between the FRET efficiencies obtained for the lower rhodamine B concentrations, whereas for the 30  $\mu\text{M}$  samples the results seem to agree. The highest FRET efficiency measured was in the 50  $\mu\text{M}$  sample and it corresponds to a distance of 4.69 nm between the fluorophores. A comparison between the FRET efficiencies obtained for the donor-acceptor pair in skin vs. POPC bilayers is shown in figure 23. Higher FRET efficiencies were achieved in POPC bilayers, with the highest efficiency corresponding to a distance of 3.9 nm between the fluorophores.

Table VI. Changes in the FRET efficiency and average distance between the donor-acceptor pair TopFluor-PC – Rhodamine-B when increasing concentrations of acceptor are added.

<i>TopFluor-PC</i> $\mu M$	<i>Rhodamine-B</i> $\mu M$	$E_{FRET}$ <i>I</i>	$E_{FRET}$ <i>II</i>	$R_0$ <i>nm</i>	<i>Average distance</i> <i>nm</i>
7	0	0	0	5.8	-
7	10	0.252	0.38	5.8	6.62 ±0.46
7	20	0.361	0.58	5.8	5.93 ±0.62
7	30	0.693	0.68	5.8	5.06±0.03
7	50	-	0.78	5.8	4.69

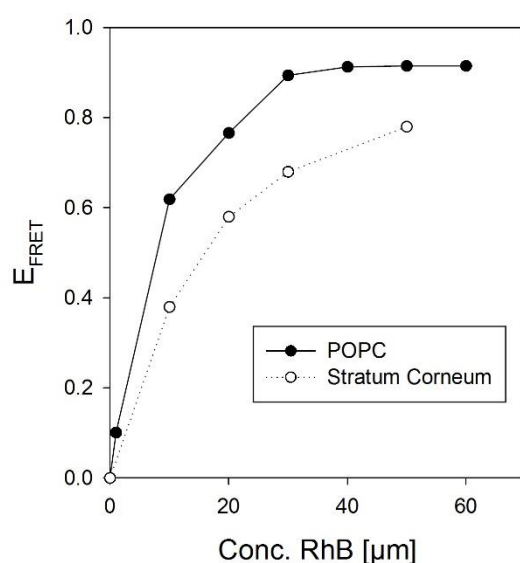


**Figure 23.** Comparison of the dependency of the FRET efficiency in the concentration of the acceptor.

In order to test if the concentration-dependent FRET effects are preserved at lower donor levels, the same set of samples were prepared where the TopFluor-PC concentration was reduced to half (3.5  $\mu M$ ). The obtained images and approximate FRET efficiencies can be found figure S5 in Appendix II. In this case, there were obtained FRET efficiencies with values of 0.2-0.6 but no correlation could be found between the acceptor concentration and the observed FRET efficiency. Interestingly, when an even lower donor concentration was used to label the skin (1.75  $\mu M$  TopFluor-PC), no FRET effect could be observed, even for the samples with a high rhodamine-B concentration.

The complexity of the fluorophore distribution and FRET interactions in human skin was obviously higher than in the lipid bilayers. Firstly, there could be observed changes in the lifetime of the donor fluorophore with respect to the area of the skin where the fluorophore was localized. It is known that the fluorescence lifetime of a probe depends on the environment that the compound is situated in [70]. Ariola et al. [71] has used two-photon lifetime imaging studies in giant unilamellar vesicles to show that BODIPY-PC has a specific lifetime according to the lipid phase it is situated in. In the

ordered gel phase, BODIPY-PC had a lower lifetime (about 3.8 ns) compared to the fluid phase (about 5.2 ns). They attributed this phase-specificity of excited-state lifetime to the stacking of the lipid ordered molecules, which can possibly enhance the homo-FRET between the donor molecules. BODIPY-PC is a probe very similar to TopFluor-PC. In our study, it was observed that the lifetime of TopFluor-PC, is higher in the viable epidermis (4.58 ns) compared to the stratum corneum (3.73 ns). This can be attributed to the more liquid membranes present in the lower layers of the epidermis, compared to the tightly packed and ordered lipid stacks in the stratum corneum.

Researchers in our group have proved that lipid dyes similar to TopFluor-PC are very good at labelling the stratum corneum and that they have a specific affinity for the stacked bilayers formed in between the corneocytes in the horny layer [72]. Since these layers are highly hydrophobic, they should not permit any hydrophilic compound to access it. Still, a FRET effect could be observed at the level of stratum corneum when the skin was labelled with both the hydrophobic TopFluor and the hydrophilic rhodamine-B. This means that the molecules should be in close proximity to each other, as FRET is not sensitive at long distances between the donor and acceptor. Therefore, rhodamine-B must diffuse in between the stacked intercellular lipid bilayers in order for FRET to occur. We suppose that it should be situated at the polar head groups of the molecules. Here it is close enough to accept energy from the TopFluor-PC which sits buried in the highly hydrophobic regions of the bilayers. Our study reports that rhodamine-B diffuses to a distance of 5-8 nm from the TopFluor molecules and this distance varies with the concentration of both dyes.

Also, we have shown that a minimum of 3.5  $\mu\text{M}$  of TopFluor should be used to label the skin if it is desired to obtain a FRET effect.

The study did not manage to obtain a quantitative analysis of the probe concentration influence on the FRET effect between a donor and acceptor. Even though a trend of increasing FRET efficiency at higher levels of acceptor was observed in duplicate samples, the results were not consistent enough to create a model for this effect. The inability to obtain perfectly reproducible results may be due to the many factors that can influence the FRET effect in such a complex tissue, *e.g.* intra-ensemble FRET, inhomogeneous labelling of the skin, or diversity of skin belonging to different body parts or different patients.

By comparing the FRET efficiencies obtained in the skin and the bilayer models, it can be seen rhodamine B is 0.8 nm closer to TopFluor-PC in the artificial bilayer compared to the stratum corneum. But still, not the same maximum concentration was used for the skin samples as for the supported bilayers. Therefore, a skin experiment with even higher rhodamine B concentrations might show if the minimum distance between the fluorophores in the stratum corneum could get even lower than 4.69 nm.

## 3.2. Fluorescence anisotropy studies

### 3.2.1. Calibration of the polarization-resolved microscope

In order to test the microscope setup for the steady-state anisotropy studies, fluorescence anisotropy measurements of solutions of Rhodamine-B 10  $\mu\text{M}$  in PBS buffer with increasing concentrations of glycerol (0%, 25%, 50%, 75%, 100%) were performed. A higher amount of glycerol provides an increase in the viscosity of the system. This should lead to an increase in anisotropy due to a decrease in the mobility of the fluorophore. The anisotropy measurements of the same solutions were performed on both a two-photon excitation microscope and a fluorometer with a one-photon excitation light source. The solutions were prepared and analysed in triplicate.

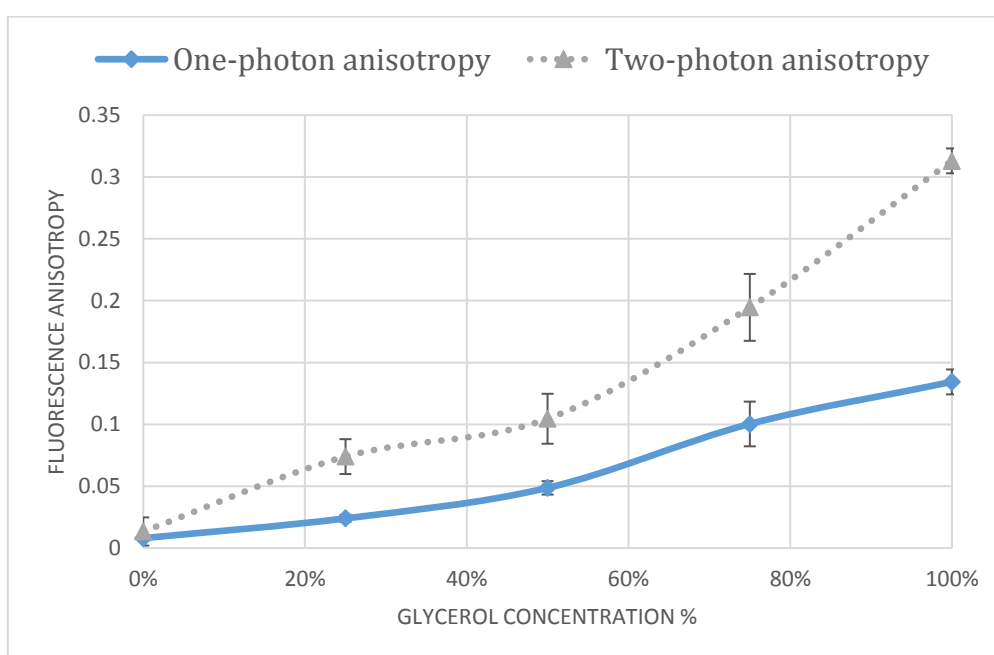


**Figure 24.** Comparison of the two-photon versus one-photon excitation anisotropy values for a 4  $\mu\text{M}$  Rhodamine-B solution in water with 0%, 25%, 50%, 75%, 100% added glycerol.

The anisotropy values for the two-photon experiments grew from 0.02 for the Rhodamine-B in PBS buffer to 0.31 for Rhodamine-B in 100% glycerol, which indicates that an increased glycerol concentration results in an increase in the anisotropy of the system. The same trend is observed in case of the one-photon experiment, but in this case the anisotropy grows slower, to reach a value of 0.14 for the Rhodamine-B sample in glycerol. This is less than half than the anisotropy value obtained in the two-photon experiment (figure 24).

The value of anisotropy obtained for rhodamine-B in glycerol are almost identical to the ones obtained in two articles by Mathews et al. [73, 74]. This suggested that the anisotropy system functions correctly and it can be used for further studies.

By comparing the anisotropy values obtained in the fluorometer to the ones obtained in the two-photon excitation microscope, it can be seen that the two photon microscope gave higher anisotropy values. This was an expected and positive result, as it

is known from theory that two-photon excitation gives higher anisotropies [46]. This is due to the fact that two-photon excitation has an inherent bias towards exciting fluorophores that are oriented at small angles  $\theta$  with respect to the electric field of the polarization light.

### 3.2.2. Fluorescence anisotropy in ternary supported lipid bilayers

The steady-state anisotropy in a ternary lipid supported bilayer was measured with a two-photon microscope. The ternary lipid bilayer was composed of a mixture of 1:2 DOPC:DPPC with 40% CHOL and 0.5  $\mu\text{M}$  Oregon Green<sup>®</sup>488-DHPE (OG). This mixture can form lipid domains due to the different transition temperatures of the lipids present in the bilayer [75]. Figure 25 A and Figure 25 B show that circular lipid domains were formed on the lipid bilayer of DOPC, DPPC and cholesterol by annealing the bilayer at 60°C followed by controlled cooling to 25 °C. The lipid dye is situated on the entire surface of the bilayer, but a higher green fluorescence intensity can be observed in the circular domains, which suggests that there is the area where the green dye Oregon Green<sup>®</sup> 488-DHPE accumulates.

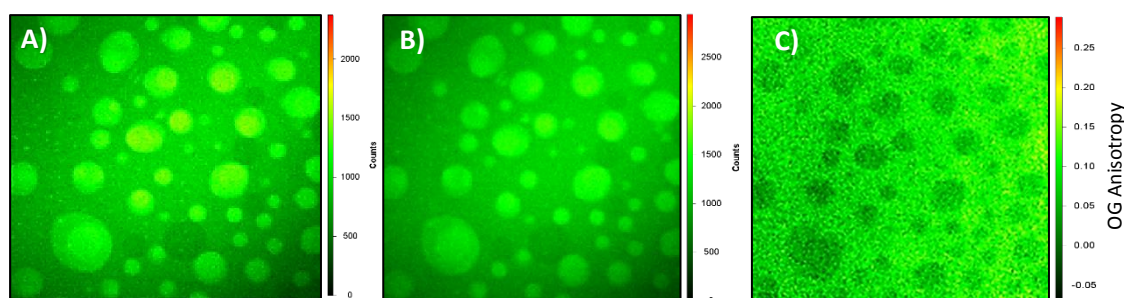


**Figure 25.** A) and B) represent fluorescence intensity images of Oregon Green incorporated in DOPC:DPPC:CHOL (20:40:40) supported lipid bilayers. Figure A) represents channel 1 ( $\perp$ ) and figure B) represents channel 2 ( $\parallel$ ). Figure C) represents the calculated anisotropy of Oregon Green 488-DHPE in the lipid bilayer.

Figure 25 C represents the calculated anisotropy of Oregon Green in the ternary lipid bilayer. It can be easily noticed that the circular areas, where the green dye accumulates, have a lower anisotropy (around  $r = 0$ ) compared to the surrounding matrix where the anisotropy has a positive value of about 0.15.

The regions with a lower anisotropy suggest an increased mobility of the fluorophore, which is representative for a less ordered phase in the lipid bilayer. A higher anisotropy is typical for a more ordered lipid phase, where the fluorophore's rotation is hindered by the increased rigidity of the bilayer.

Our results suggest that the bright areas are corresponding to the liquid disordered (LD) lipid phase due to a lower anisotropy. There are at least two arguments that can confirm our assumption: a) the phase diagram published in literature by Keller et al. [75] shows that for the lipid mixture of 20:40:40 DOPC:DPPC:CHOL it is expected to obtain a continuous liquid ordered (LO) phase which surrounds circular islets where the liquid disordered (LD) phase exists. b) Zhu et al. [76] have discussed the preferential

accumulation of the OG fluorophore in the LD phase, so the areas with a stronger OG fluorescence intensity corresponds to the LD areas.

This success of this experiment shows again that our fluorescence anisotropy setup is working properly and can be used to discriminate between lipid phases in supported bilayers.

### 3.2.3. Fluorescence anisotropy in human skin

The time-resolved anisotropy curves were determined on 20  $\mu\text{m}$  thick skin slices labelled with Rhodamine-B and for solutions of free dyes Rhodamine-B and ATTO647N in PBS buffer.

A rhodamine B sample in PBS was used to calibrate the system. The signal from the parallel detector channel was scaled by a correction factor  $G$  so that the anisotropy went to zero for longer times as is expected for a free dye. A plot of the fluorescence intensities  $I_{\parallel}(t)$  for the parallel ( $\parallel$ ) and  $I_{\perp}(t)$  for the perpendicular ( $\perp$ ) detectors is represented in figure 26 A. The time-resolved anisotropy for Rhodamine-B in water was determined by calculating the anisotropy ( $r$ ) for each time point, by applying the equation 15:

$$r(t) = \frac{I_{\parallel}(t) * G - I_{\perp}(t)}{I_{\parallel}(t) * G + 2 * I_{\perp}(t)} \quad (\text{eq. 15})$$

The anisotropy values were then plotted as (figure 26 B). The anisotropy of rhodamine B in PBS decays from a value of ca. 0.4 and equilibrates to around  $r = 0$  in about 0.6 ns. A value of anisotropy around 0 is a sign of free rotation of the dye molecules. To test the system the ATTO647N sample was measured and analysed using the correction factor  $G$  found from the RhB measurements. A similar decay to an equilibrium value of  $r(t) = 0$  was also observed for the solution of ATTO647N in PBS.

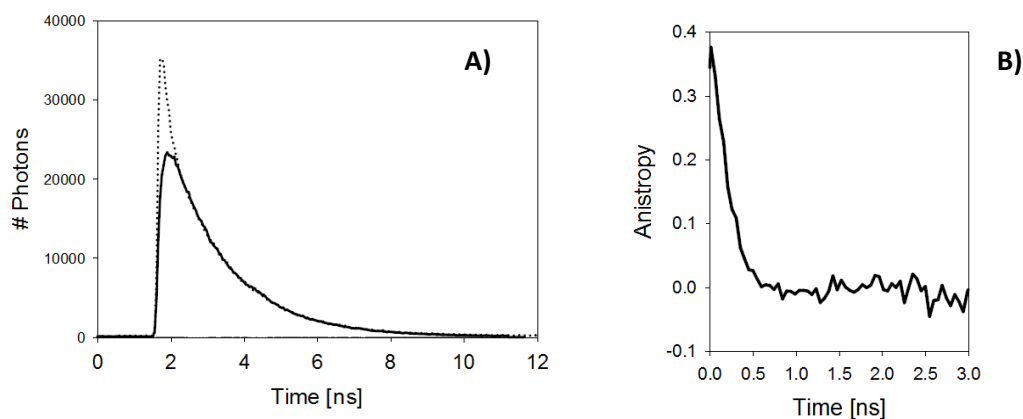


**Figure 26. A)** Plot of the fluorescence intensities vs. time at the parallel ( $\parallel$ ) and perpendicular ( $\perp$ ) detectors for RhB in water. The dotted line is  $I_{\parallel}(t)$  while the solid line is  $I_{\perp}(t)$ ; **B)** The time-resolved anisotropy decay for Rhodamine-B in water.

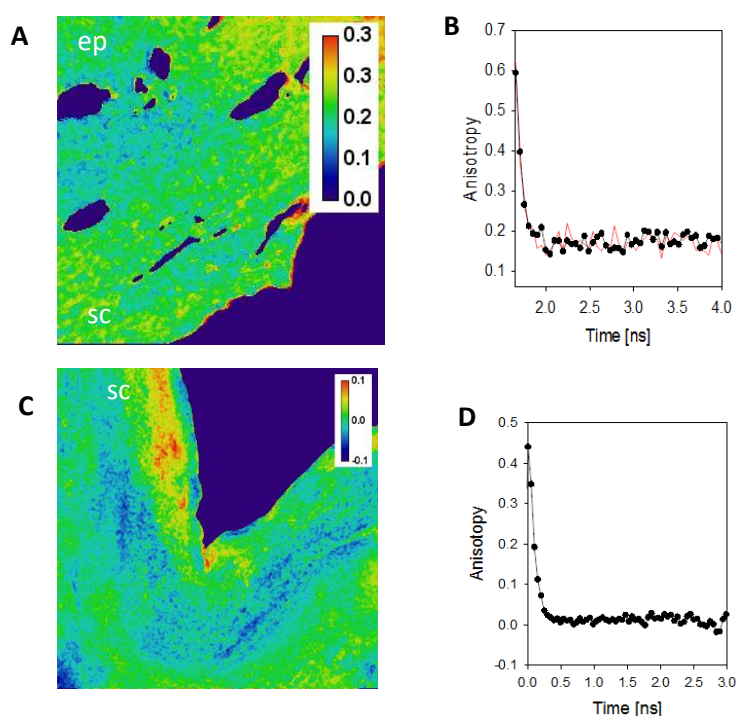


**Figure 27.** Steady-state and time-resolved anisotropy of the red fluorescent dyes Rhodamine-B and ATTO647N. **A)** A color map of the steady-state anisotropy for RhB in human skin. **B)** The time-resolved anisotropy for RhB in the SC of human skin. **C)** The steady-state anisotropy for Atto647N in human skin. **D)** The time-resolved anisotropy for Atto647N in the SC of human skin; sc – stratum corneum; ep – viable epidermi. Please note the different scale bars for figures A) and C).

By measuring the steady-state anisotropy of a skin slice labelled with rhodamine B, a colour map of the anisotropy in the outer and inner layers of the epidermis was obtained (figure 27 A). It can be observed that the anisotropy goes from 0 in the background (blue) to around 0.3 in the viable dermis. In the color map, Rhodamine-B anisotropies appear to be higher in the stratum corneum compared to the dermis.

When looking at the time-resolved anisotropy in figure 27 B, it can be observed that the anisotropy has a value of about 0.6 at the first time-point, which is then decaying and remaining stable around an average value of 0.19. As opposite to the Rhodamine-B solution in water, the anisotropy  $r(t)$  of Rhodamine-B in skin does not go to 0, which suggests that the rotational mobility of the molecule is decreased when it is situated in the stratum corneum.

For the skin slices labelled with the red probe ATTO647N, the colour map of the steady-state anisotropy can be observed in figure 27 C. Across the skin sample, the anisotropy varies from around -0.05 to around 0.1. The anisotropies seem to have lower values for ATTO647N than for Rhodamine-B, but the same increased anisotropy in the stratum corneum is observed. By looking at the time-resolved anisotropy for ATTO647N in skin (figure 27 D), it can be noticed that the anisotropy decays to an average value of about 0 which means that ATTO647N becomes depolarized. This results suggests that ATTO647N has a free rotational mobility when situated in the skin.

This study shows that rhodamine B does not have free rotation in the SC, as opposed to ATTO647N which moves freely. The hindered rotation of rhodamine-B might be due to binding to the keratin present in SC [77].

The rotation of the dye molecules with respect to each other are an important parameters when evaluating FRET efficiencies of donor-acceptor pairs. This is because

the Förster distance  $R_0$  depends on a term called  $k^2$  which is a constant that is defined by the orientation between the acceptor and donor fluorophore. In calculating the Förster distance, it is common to use a value of  $2/3$  for  $k^2$ , which assumes a random orientation of the molecules [49].

As we can see in this study, rhodamine B has a hindered rotation so if we use a value of  $2/3$  for  $k^2$  for calculating the Förster distance, the interpretation of the results might not be accurate. On the other side, for ATTO647N we could demonstrate that it does not bind to structures in the SC, therefore this would not be a source of inaccuracy when evaluating FRET effects in the skin.

### 3.3. Niosome formulation and characterisation

The non-ionic surfactant vesicles (niosomes) were composed of Span 80 (or Span 60) and Tween 80 (or Tween 60) in different ratios. Cholesterol was added to stabilize the membrane [78] in all formulations at a constant ratio of 4:1 surfactants:CHOL. Preliminary studies were performed to find an appropriate preparation method. A total of nine different formulations have finally been prepared by the thin film hydration method, followed by repeated extrusion through polycarbonate filters with decreasing pore size down to 100 nm.

Five non-loaded formulations (Nio60-a, Nio60-b, Nio60-c, Nio50-d and Nio80-d) were prepared to find the optimal ratio between the two types of surfactants (Span and Tween) that takes to the formation of small, monodisperse and stable vesicles.

Based on the results, four formulations (Nio60-d-FL, Nio60-e-FL, Nio80-d-FL and Nio80-e-FL) were doubly-loaded with both a lipophilic fluorescent probe (Laurdan 200  $\mu\text{M}$ , blue) and a hydrophilic probe (Rhodamine-B  $\mu\text{M}$ , red). The loaded formulations were prepared with the aim to investigate the niosomes' capacity to incorporate hydrophobic and hydrophilic probes and to deliver them into the skin.

#### 3.3.1. Shape and morphology of the niosomal formulations

Figure 28 represents the microscopic images of the non-extruded Nio60-c formulations (left image) and the Nio60-c formulation extruded 5 times through a stack of two 800 nm polycarbonate filters (right image). Particles in the  $\mu\text{m}$ -size range were formed after applying the thin layer hydration (TLH) method and before forcing the particles to pass through polycarbonate filters. All the particles were round-shaped and rather diverse in size. Extrusion through 800 nm filters resulted in size reduction of the particles and more homogeneous particles, but which are still large enough to be observed in the optical microscope.

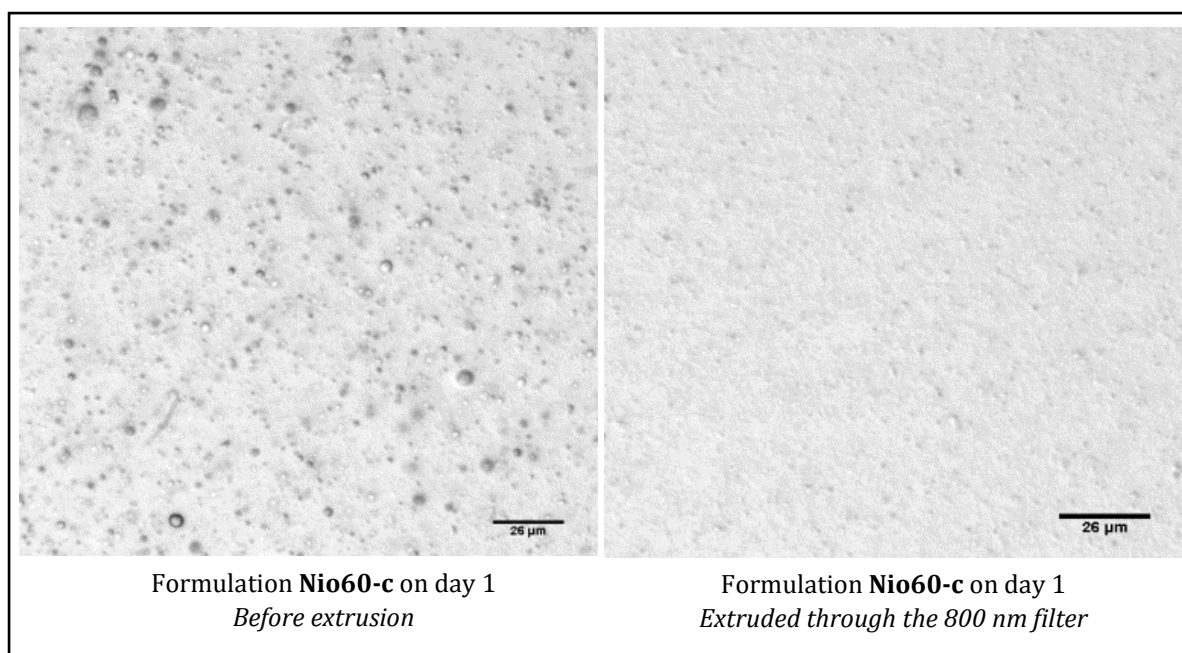


**Figure 28.** Microscopic images of non-extruded, empty niosomes. Left: before extrusion. Right: After extrusion through 800 nm polycarbonate filters

No structures could be observed in the formulations extruded through 400 nm, 200 nm or 100 nm. This proves that the particles got down to sizes which were smaller than the resolution limit of the optical microscope.

Figure 29 represents confocal laser scanning microscopy (CLSM) images of the four niosomal formulations loaded with fluorescent dyes (Nio60d-FL, Nio60e-FL, Nio80-d-FL, Nio80-e-FL), prior extrusion.

Laurdan and rhodamine B appear to be included in spherical structures, which suggests that they have been incorporated into the vesicles. The vesicles have sizes in the  $\mu\text{m}$ -size range for all formulations, but the unextruded Nio60-d-FL and Nio60-e-FL (based on Span 60 and Tween 60) appear to have generally a larger size than the Nio80-d-FL and Nio80-e-FL formulations (based on Span 80 and Tween 80).

Another interesting information provided by the confocal imaging of the niosomes is the distribution of the fluorescent dyes throughout the vesicles, which provides information about the vesicle morphology. The formulations based on Span 60 and Tween 60 (Nio60-d-FL and Nio60-e-FL, first two rows in figure 29) appear to have the lipophilic blue probe localized only at the outer layer of the vesicles, while the hydrophilic red dye is localized inside the vesicles. This suggests the formation of giant unilamellar vesicles (GUVs) that have the lipophilic Laurdan accumulated in the bilayer membrane and the hydrophilic rhodamine B in the aqueous compartment.

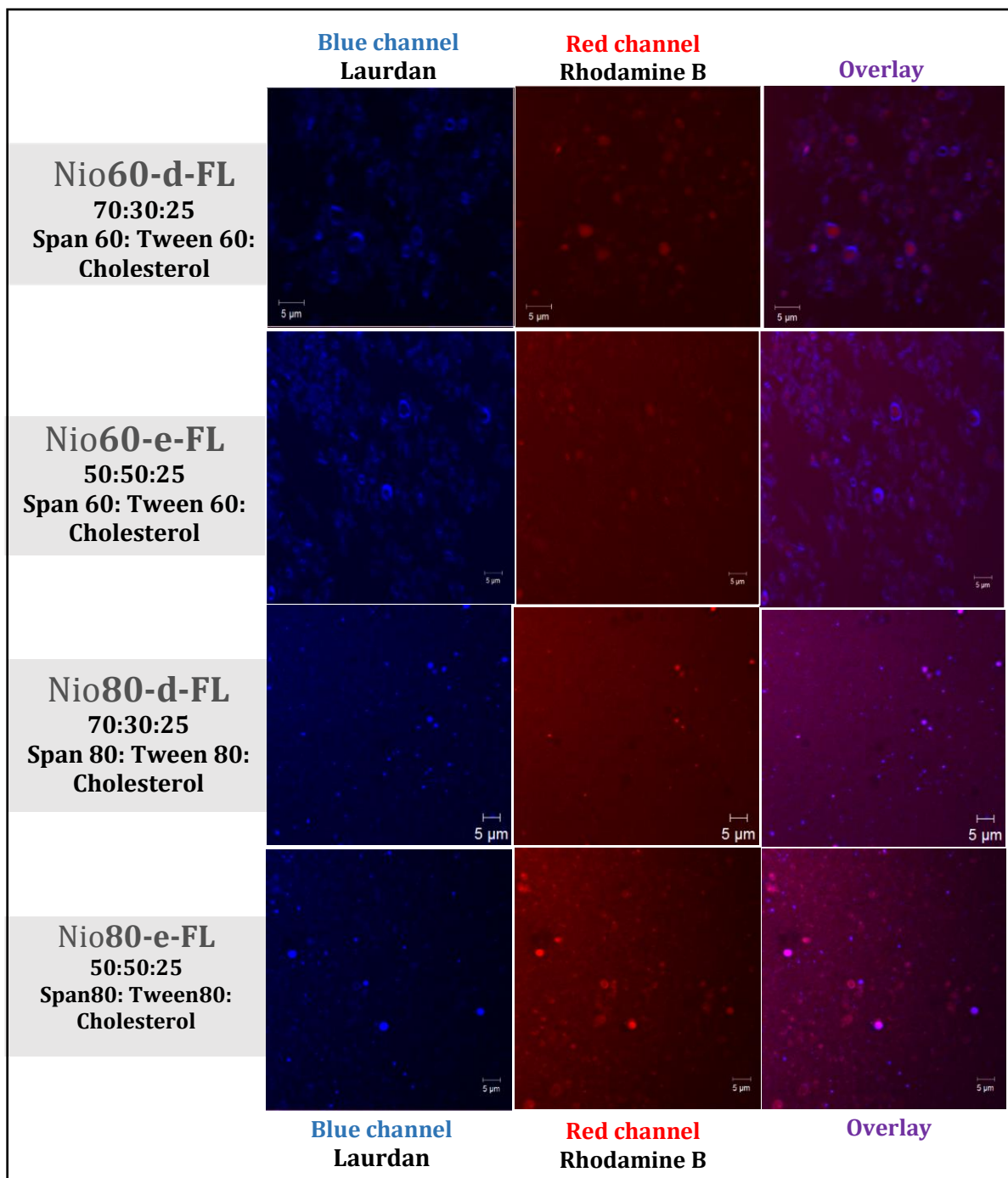


**Figure 29.** Laser scanning confocal microscopic images of non-extruded niosomes loaded with fluorescent dyes. From left to right: blue channel (Laurdan), red channel (Rhodamine B) and merged channels (overlay). Images were taken with a 63x water immersion objective.

On the other side, the structures formed by the Span 80 and Tween 80 (Nio80-d-FL and Nio80-e-FL, last two rows in figure 29) do not show the same distribution of the dyes in their structure. The lipophilic and hydrophilic dye seems to be distributed homogeneously throughout the particles. This may imply that more complex structures have been formed (e.g. multilamellar structures or vesicles).

It is important to note that the information presented by the bright field and confocal microscopic experiments is only related to the non-extruded vesicles. As the vesicle shape, lamellarity and loading capacities may dramatically change during the extrusion process, the above described observations cannot be necessarily attributed to the extruded niosome formulations which have been used in the skin penetration experiments.

### 3.3.2. Particle size

Table VIII indicates the composition and physical properties of the niosome formulations measured by dynamic light scattering (DLS). Formulation Nio60-a, which contained only Span 60 and cholesterol, could not be analysed in the DLS due to visible instability observed during the preparation process. Formulation Nio60-b, which contained Span 60: Tween 60 in a ratio of 9:1 had a PDI > 0.571 and was thus too polydisperse to be analysed by DLS. Due to insufficient quality, Nio60-a and Nio60-b were not considered for any other further tests.

**Table VIII.** Characteristics of the niosome formulations.

	<b>Nio 60-a</b>	<b>Nio 60-b</b>	<b>Nio 60-c</b>	<b>Nio 60-d</b>	<b>Nio 60-d-FL</b>	<b>Nio 60-d-FL</b>	<b>Nio 80-d</b>	<b>Nio 80-d-FL</b>	<b>Nio 80-e-FL</b>
<b>Span: Tween ratio</b>	10:0	9:1	8:2	7:3	7:3	5:5	7:3	7:3	5:5
<b>Components (mM)</b>									
Span 60	80	72	64	56	56	40	-	-	-
Span 80	-	-	-	-	-	-	56	56	40
Tween 60	-	8	16	24	24	40	-	-	-
Tween 80	-	-	-	-	-	-	24	24	40
Cholesterol	20	20	20	20	20	20	20	20	20
Rhodamine B	-	-	-	-	0.4	0.4	-	0.4	0.4
Laurdan	-	-	-	-	0.2	0.2	-	0.2	0.2
<b>Size (nm)</b> ± stdev	N/A	<b>272</b> ± 32	<b>233</b> ± 1	<b>133</b> ± 0.3	<b>80</b> ± 0.5	<b>66</b> ± 1	<b>126</b> ± 1	<b>117</b> ± 2	<b>83</b> ± 1.5
<b>PDI</b> ± stdev	N/A	N/A	<b>0.239</b>	<b>0.218</b>	<b>0.17</b> ± 0.01	<b>0.20</b> ± 0.01	<b>0.19</b>	<b>0.11</b> ± 0.03	<b>0.05</b> ± 0.03
<b>% Rh-B entrapped</b> ± stdev	-	-	-	-	N/A	N/A	-	<b>13.1</b> ± 1.2	<b>5.5</b> ± 0.7

Nio60-a, Nio60-b, Nio60-c, Nio60-d and Nio80-d – empty niosomes;

Nio60-d-FL, Nio60-e-FL, Nio80-d-FL and Nio80-e-FL – loaded niosomes.

Stable niosomes with a mean particle sizes that ranged between  $66 \pm 1$  nm and  $233 \pm 1$  nm were obtained in the formulations where the Tween was added into a ratio  $\geq 20\%$ . The PDI was < 0.24 for the empty vesicles and < 0.2 for the fluorescent dye-loaded

niosomes. Only Nio80-d-FL and Nio80-e-FL can be considered to be rather homogeneous. Interesting to note that PDI was much lower for the loaded formulations.

By looking at the average size and PDI of all loaded and non-loaded formulations in table VIII, a clear trend can be observed towards a decrease in average size and PDI of the vesicles with increasing amount of Tween, in the case of both Span 60/Tween 60 and Span 80/Tween 80 formulations. This Tween-induced reduction in vesicle size might be attributed to the fact that polysorbate is able to increase the deformability of the vesicle bilayer due to its hydrophilicity, increased radius of curvature and mobility [79]. This may result in a more efficient size reduction upon extrusion even through the 100 nm and thus more stable and more homogeneous dispersions, with smaller vesicle sizes.

An unexpected observation was that the formulations with identical surfactant composition showed differences in size and PDI when the fluorescent dyes were incorporated. Both in the case of the Nio60-d/Nio60-d-FL and Nio80-d/Nio80-d-FL, the encapsulation of the dyes resulted in a small decrease in the size and PDI of the vesicles. This aspect should be investigated more in detail (e.g. repeatability of results).

The four niosome formulations loaded with fluorescent dyes have a size that makes them promising for delivery to the inner skin layers. Verma et.al. [80] demonstrated for liposomes that vesicles with a size  $\leq 300$  nm delivered their contents to some extent through the deeper skin layers, while vesicles with a size  $\leq 70$  nm show and even higher fluorescence intensity, both in the viable epidermis and the dermis.

### 3.3.3. Physical stability

After 30 days of storage at 25 °C, the vesicle size and PDI were measured again in order to evaluate the physical stability. All formulations were also checked for visual changes, in parallel to the DLS analysis. Figure 30 compares the size and PDI of the formulations measured at the day 1 and day 30 after the preparation. Nio60-a and Nio60-b were not included as they were unstable already the day after preparation.

The size of the particles did not change dramatically upon storage and only variations of maximum 5-10 nm could be noticed for most formulations. For Nio60-c, which contained 7:3 Span 60: Tween 60, a fine white sediment of a very small volume was observed upon visual inspection at day 30. This sediment was re-dispersed before the DLS analysis. Probably the presence of these large particles resulted in the larger z-average diameter of around 40 nm (figure 30). The sedimentation and increase in particle size indicates a lack of physical stability and this formulation was, therefore, not considered for further studies.

When looking at the variations in particle diameter observed between day 1 and day 30, the changes in size are so small that they can be considered negligible.

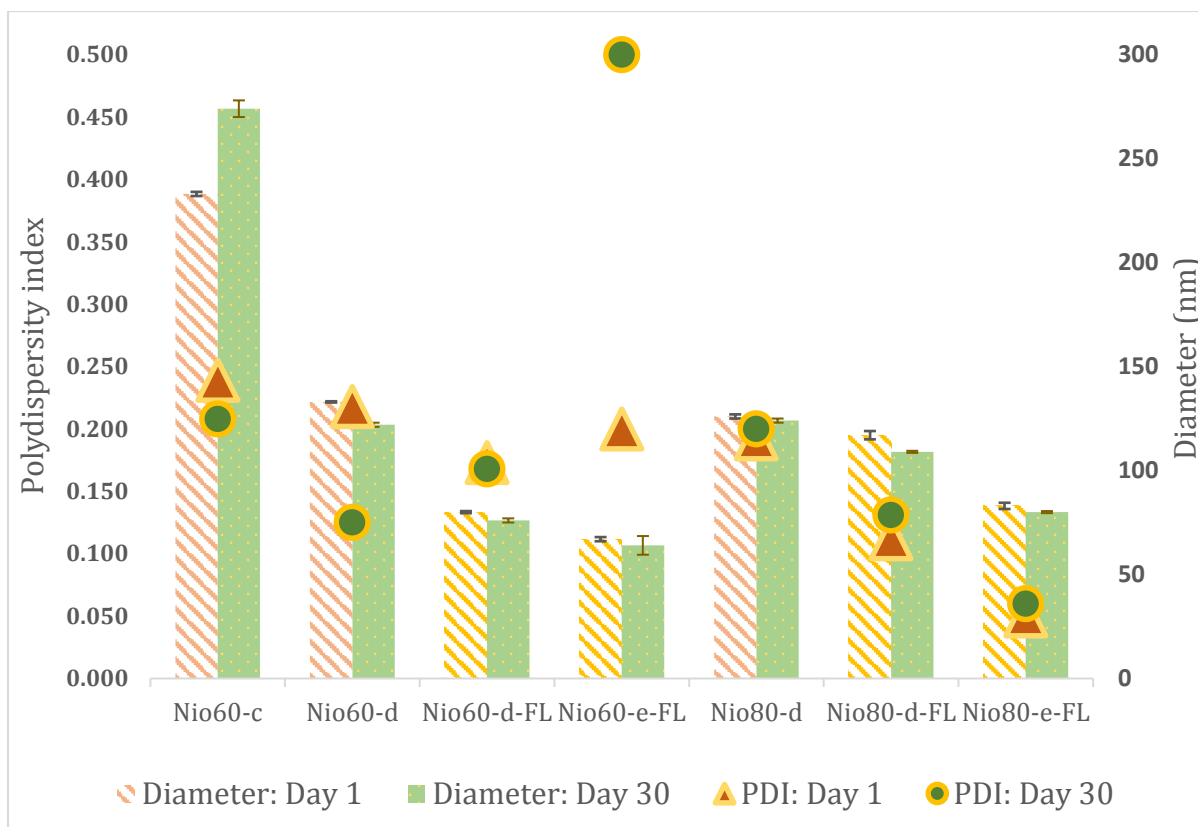


**Figure 30.** Stability of the niosome formulations over 30 days of storage at 25 °C. The columns on the left (striped pattern) represent the average diameter of the particles at day 1 of the preparation. The columns on the right represent the average size at day 30 of the preparation. The triangles represent the PDI at day 1, while the dots show the PDI at day 30.

The polydispersity index (PDI) was as well an important parameter that needed to be taken into consideration when evaluating the physical stability of niosomes. As it can be observed in figure 30, for almost all the formulations, the PDI was more or less unchanged after storage. The only exception was Nio60-e-FL containing a ratio of 5:5 Span 60: Tween 60 where a PDI of 0.571 was measured after 30 days of storage. This increase in polydispersity might suggest that a too high amount of the flexible and hydrophilic Tween 60 in the niosome composition might destabilize the vesicular bilayers. Due to its short shelf time, this formulation has not been selected for experiments on skin.

On the other side, the formulation with the same ratio of the two types of surfactants, but where the hydrophobic tail is composed of oleic acid instead of stearic acid (Nio80-e-FL composed of 5:5 Span 80:Tween 80) did not show the same lack of physical stability in time, as the PDI remained constant at a value < 0.1.

### 3.3.4. Encapsulation efficiency

The encapsulation efficiency of the loaded vesicles was determined in order to evaluate how much rhodamine-B was entrapped inside the vesicles and how much of it remained in the hydration buffer. The spin-column technique was employed for all four

formulations containing rhodamine B and it was successful for separating the niosomes containing Span 80 and Tween 80 from the free dye. A clear separation was observed where the niosome-containing fractions were eluted first, followed by fractions that did not contain either dye or vesicles and then by fractions that contained the free rhodamine B.

An encapsulation efficiency of  $13.1 \pm 1.2$  % was obtained for the formulation Nio80-d-FL and of  $5.5 \pm 0.7$  % for the formulation Nio80-e-FL. Niosomes with sizes around 100 nm (Nio80-e-FL) which have very small inner compartments, and a lower encapsulation efficiency can, therefore, be expected. In table VIII it can be seen that the Nio80-d-FL niosomes with an average size of 117 nm incorporated more than double the amount of rhodamine-B than the Nio80-e-FL niosomes with an about  $\sim 34$  nm smaller vesicle size.

No data is presented for the niosomes based on Span 60 and Tween 60 because the separation process was not successful. In this case, it could not be observed that rhodamine B eluted in two successive steps as it could be seen for the Nio80 vesicles. This is probably due to micelles present in the samples, which elute after the vesicles and before the free dye, so the separation of niosomes cannot be clearly distinguished. Therefore it was concluded that all the fractions contained mixed vesicles and free dye due to insufficient separation. A different elution protocol or method should be developed in the future to separate these vesicles from non-encapsulated dye.

Alternatively, a direct method for quantifying the Rhodamine-B in the vesicles could have been employed, where a solubilizing agent like Triton X or methanol would have been employed to disrupt the vesicles and free up the incorporated dye. But in this case, another separation step (*i.e.* HPLC) would have been needed to separate the dye from the surfactants, lipids and solvents in the mixture, as they can have a strong influence on the fluorescent properties of the dye. Another approach would have been to create a calibration curve where all the compounds of the mixture are added, except the molecule of interest. The development of an HPLC method for separating the dye from the niosome components or adding an organic solvent to the mixture/calibration curve would also have been useful for the solubilisation and quantification of Laurdan in the niosomes. Laurdan is a lipophilic dye which cannot be measured indirectly as a free dye, as it is not soluble in the citric acid buffer that forms the external phase of the system.

### 3.4. *Ex vivo* skin diffusion testing of nano-formulations

Non-ionic surfactants function as penetration enhancers being able to increase cutaneous drug absorption [78, 81-83]. Niosomes have demonstrated to improve (trans)dermal drug delivery by fusing with the lipids in the stratum corneum thus creating a high drug concentration gradient at the surface of the skin. This creates a driving force for the permeation of the drug into the skin [84].

In the present study, the ability of non-ionic surfactant vesicles to penetrate human skin has been investigated using Franz diffusion chambers, where the formulations were applied non-occlusively. The obtained images are then analysed to obtain a semi-quantitative evaluation of the dye penetration in the epidermis and dermis and back-up the visual observations.

Two formulations were selected for testing on the skin: **Nio80-d-FL** and **Nio80-e-FL**, both based on Span 80 and Tween 80 due to their good stability and adequate size (80-120nm) and polydispersity (<0.11), which makes them good candidates for topical delivery. Also, they could be successfully separated by the spin-column method to determine the encapsulation efficiency of the hydrophilic dye. For the skin diffusion testing, formulations that contained both the fluorescent niosomes and the free dyes were employed. This is because the batches of niosomes prepared were not large enough to extract an appropriate amount of pure niosomes for all the skin experiments.

The experiments included one blank sample where only the citrate buffer solution was applied on the skin (termed untreated skin) and two control experiments where both fluorescent dyes were applied as dye solution.

Figures 31 A-O show a comparison between the fluorescence intensities of Laurdan and rhodamine B present in the epidermis and dermis of each skin slice obtained from the diffusion to the experiment.

Figure 31 A and 31 B represent the control experiments, where the free dye solutions were tested. From the control experiment, it can be clearly observed that Rhodamine B (red dye, hydrophilic) accumulated very well in the epidermis and is also present in the dermis (figure 31 A). However, as the control sample was altered during the experiment, it will not be used for further comparison.

In figure 31 B it can be seen Laurdan (blue dye, lipophilic) did not penetrate the epidermis when applied as solution, even though a methanol solution was applied and methanol has an inherent penetration enhancing effect [85]. Still, due its high toxicity, methanol is not appropriate as an additive in skin formulations (figure 31 B). Figure 31C is a schematic representation of the skin layers [3] added to help interpret the confocal images.

Figures 31 D and 31 G represent samples where the skin has been treated with the surfactant-based formulations (**Nio60-d-FL** and **Nio60-e-FL**, respectively). For both formulations, it can be clearly observed that the dye encapsulation in nanoparticles resulted in an increase in the diffusion of the lipophilic fluorescent dye through the skin, compared to the free Laurdan solutions. The fluorescent dye appears to be preferentially

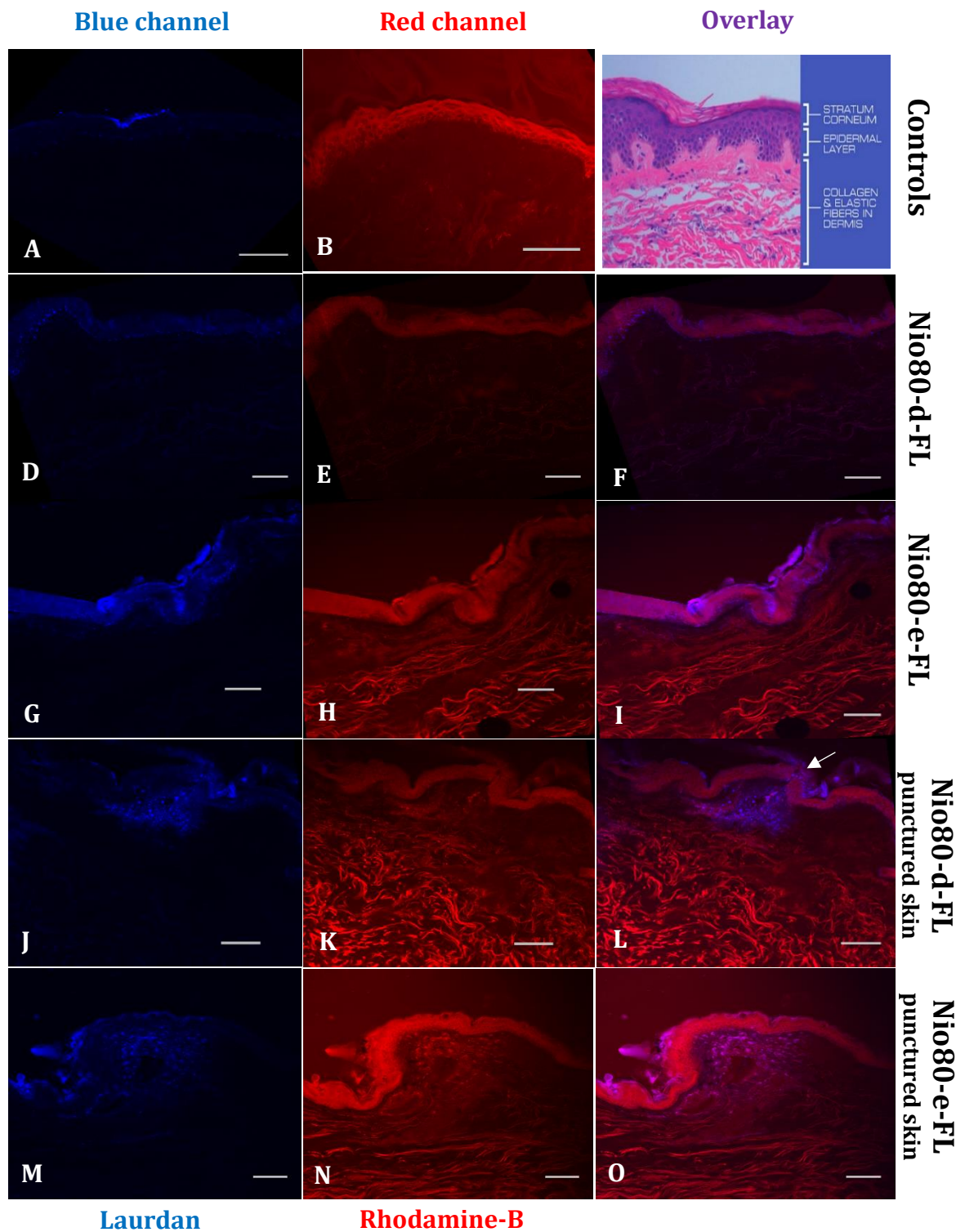


**Figure 31.** Images D-O: CLSM micrographs of cross-sections of human skin incubated in Franz diffusion cells with niosomes containing a lipophilic label, Laurdan and a hydrophilic label, Rhodamine-B. The niosomes have been applied on the skin non-occlusively for 24 h. Images A and B presents the samples where free Laurdan and Rhodamine-B solutions were applied as controls. Image C contains a schematic representation of the skin layers present in the micrographs [3]. Normal skin: Images D-I. Punctured skin: Images J-O. A puncture in the skin is pointed by a white arrow in image L. The scale bars represent 75  $\mu\text{m}$ .

distributed throughout the stratum corneum and viable epidermis and does not appear to reach the inner skin layers.

In the case of the **Nio60-d-FL** formulation, the lipophilic blue dye Laurdan penetrated slightly better the dermis (figure 31 D) compared to the **Nio60-e-FL** formulation, where Laurdan was mainly distributed in the epidermis (figure 31 G). This effect can be observed in the column plot which represents the data from the image analysis (figure 32). An opposite behaviour can be observed for the hydrophilic red dye rhodamine B, which penetrated better to the inner dermis in the case of **Nio60-e-FL** formulation (figure 31 H), compared to **Nio60-d-FL** formulation (figure 31 E).

Figures 31 J-O represents samples where the epidermis has been punctured by a physical penetration enhancer, represented by a commercial cosmetic microneedle device (needle diameter of 10  $\mu\text{m}$ ). In this case, the most intense rhodamine B penetration at the dermis level was observed. Also, the images 31 J-L show a puncture created by the microneedles is a diffusion route for Laurdan further through the dermis. The puncture created by the microneedles and it represented by a white arrow in figure 31 L.

At the end of the diffusion experiment, aliquots were sampled from the receptor compartment to evaluate if any amount of the fluorescent dyes applied on the skin surface has reached the receptor compartment. Rhodamine B was found in the receptor in the skin samples treated with the Dermaroller, but was not detectable for the other samples. The final concentration of Rhodamine-B in the acceptor compartment was 0.105  $\mu\text{M}$  and 0.170  $\mu\text{M}$  for **Nio80-d-FL** and **Nio80-e-FL**, respectively. This shows that physical enhancers like microneedles are able to disrupt completely the skin barrier and allow the applied formulations to reach systemic distribution.

The results suggest that incorporating lipophilic fluorescent dyes in surfactant-based formulations leads to an increase of their deposition at the skin level. For Laurdan, the amounts of fluorescence in the sample increases in the following order: blank < free Laurdan < empty niosomes + dyes outside < Nio80-d-FL < Nio80-e-FL < Nio80-d-FL + microneedles < Nio80-e-FL + microneedles (figure 32). It appears that all the formulations where nano-carriers or penetration enhancers were used showed an increase in the penetration of the lipophilic dye compared to the control. The highest penetrated amounts were present in the cases where a combination of nano-carrier and physical enhancer is used. A higher Laurdan fluorescence in the epidermis is observed for the Nio-e-FL niosomes compared to the Nio-d-FL niosomes and this might be due to the fact they are in average 34 nm smaller so they can squeeze better through the layers of the stratum corneum and accumulate in the epidermis.

Interesting to compare is the skin deposition of dyes in the case of the formulations where Rhodamine-B and Laurdan are only outside the vesicles (Nio80-d + dyes) or both inside and outside the vesicles (Nio80-d-FL). For both types of dyes, it can be observed a slight increase in the skin deposition of dyes both in the epidermis and dermis for the samples where the dyes were entrapped into niosomes. This suggests that the inclusion of the dyes in the vesicle structure plays a role in the mechanism of increased dye penetration to the skin. Similar results were obtained by Verma et al. for liposomes loaded with the hydrophilic dye carboxyfluorescein [86].

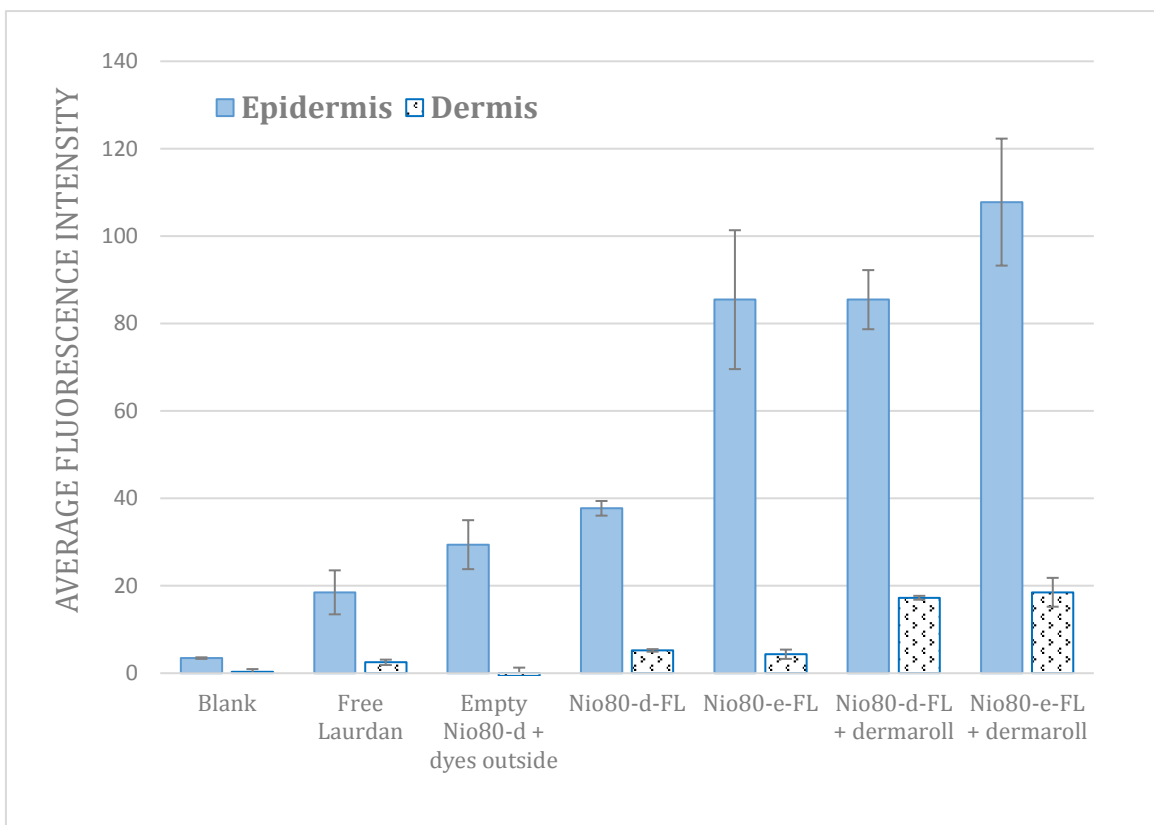


**Figure 32.** Average fluorescence intensities of **Laurdan** in skin epidermis (blue column, left) and dermis (white column, right), after the 24 h skin diffusion experiment, obtained by image analysis. The blank is represented by untreated skin.

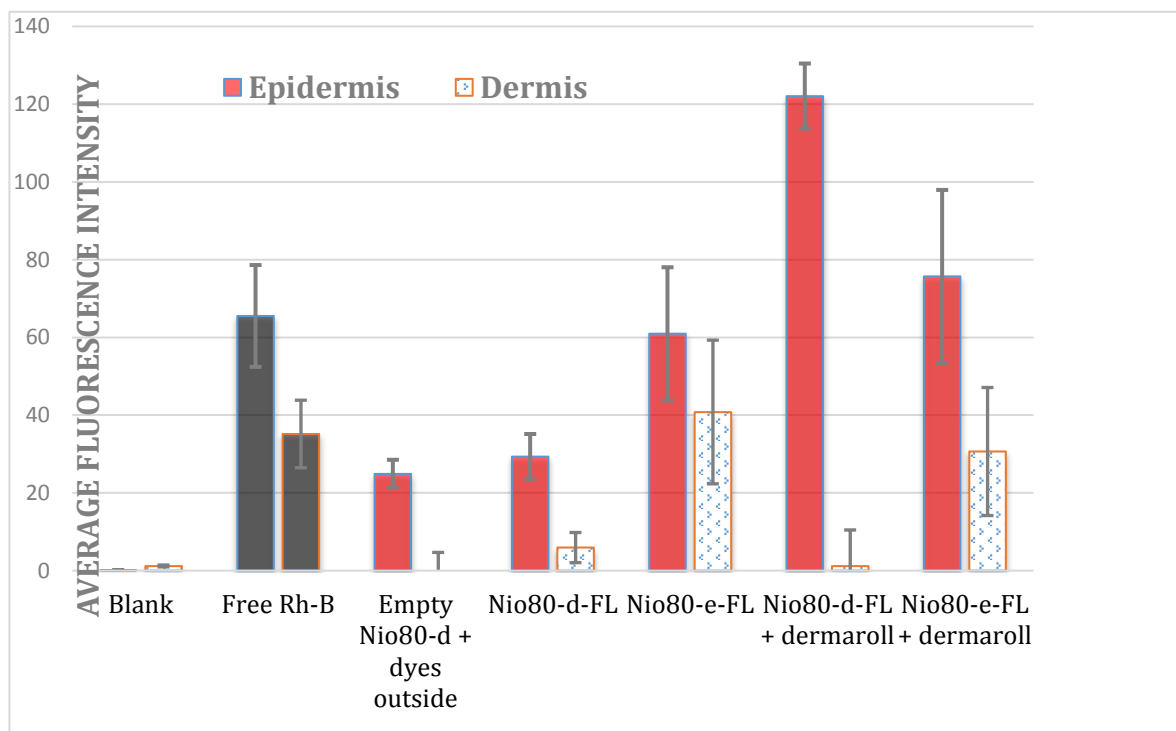


**Figure 33.** Average fluorescence intensities of **rhodamine B** in skin epidermis (red column, left) and dermis (white column, right), after the 24 h skin diffusion experiment. The blank is represented by untreated skin. The free Rhodamine-B control cannot be used for comparison as the sample was compromised (column is marked with black colour).

Figure 33 shows the accumulation of rhodamine B in the epidermis or dermis obtained from our study. One important mention is that the control rhodamine B solution was compromised due to the fact that the epidermis got detached from the dermis in many parts of the skin. This means that this sample should be re-done in order to be used as a reference, as due to its detachment two phenomena can happen: a) a gap can be formed between the epidermis and dermis so the skin diffusion is blocked; b) parts of the stratum corneum can flip during the skin cutting and cryofixing and transfer the dye from the external sc directly to the dermis.

The control experiment was not performed again due to the fact that no more skin from the same patient was available, and performing it on a different skin would still have provided limited significance in comparing the data. Therefore, in case of the figure 33, it is difficult to estimate the effect provided by loading the dyes into a nanocarrier system or using a microneedle device to alter the skin barrier.

## Chapter IV: Conclusions and future perspectives

A FLIM/FRET analysis method was optimized for calculating the distances between the FRET donor TopFluorPC and FRET acceptor rhodamine B in human stratum corneum (SC) and a POPC supported bilayer model. Our study reports that rhodamine B diffuses to a distance of 5-8 nm from the TopFluorPC molecules in the stacked lipid bilayers of the SC. An exact distance could not be determined, as it varied greatly with the concentration of both the donor and of the acceptor molecules. Still, it can be concluded that even though rhodamine B is a hydrophilic compound, it manages to penetrate to the highly hydrophobic lipid matrix of the stratum corneum. Rhodamine B diffuses 0.8 nm closer to TopFluorPC in artificial lipid bilayers compared to SC. Future skin studies with higher rhodamine B concentrations should be performed for a more accurate comparison with the supported bilayer studies.

By measuring the time-resolved anisotropy of rhodamine B and ATTO647N, it could be showed that rhodamine B molecules do not have a random orientation in the stratum corneum, probably due to binding of keratin. This might have a strong influence on the FRET interactions of rhodamine B at the skin level. For ATTO647N, a random orientation has been determined. This suggests that FRET interactions in skin could be calculated more accurately by using ATTO647N as a FRET acceptor molecule instead of rhodamine B.

The niosome formulation studies suggest that in order to obtain stable Span-based surfactant vesicles, the micelle-forming surfactant Tween should be added to the formulation in a ratio of at least 20%. Surprisingly, the incorporation of dyes in the vesicle structure lead to the formation of smaller-sized vesicles, with a decreased polydispersity index. This effect should be furtherly investigated by exploring analytical methods that can test the interactions of the fluorescent dyes with the surfactant bilayer.

Span 80/Tween 80 formulations have shown to have smaller size and increased stability compared to Span 60/ Tween 60 formulations and were selected for *ex vivo* penetration studies on human skin.

The Franz skin diffusion experiments suggest that the Span 80 /Tween 80 surfactant formulations can function as a nano-carrier for lipophilic compounds. They have proved the ability to increase the penetration of lipophilic compounds through the human skin barrier. This effect is influenced both by the size of the vesicles and the ratio of surfactants introduced in the formulation.

Moreover, a combination between a nano-carrier and a physical penetration enhancer might be even more powerful in overpassing the highly effective epidermal barrier, to deliver active compounds to the capillaries located in the dermal layers and make them available to be taken up by the systemic circulation.

# Bibliography

1. In Vitro Release Testing Methods for Semisolid Formulations [Internet]. 2009 [cited 25 may 2016]. Available from: <http://www.particlesciences.com/news/technical-briefs/2009/in-vitro-release-testing-methods.html>.
2. Wei T. Fluorescence Resonance Energy Transfer. Integrated DNA technologies, 2000.
3. Skin layers [Internet]. Scientific Rx. 2015 [cited 26 july 2016]. Available from: <https://www.scientificrx.com/layer-by-layer-each-plays-an-important-role/>.
4. Bernchou U, Brewer J, Midtiby HS, Ipsen JH, Bagatolli LA, Simonsen AC. Texture of lipid bilayer domains. *J Am Chem Soc.* 2009;131(40):14130-1.
5. Mennicke U, Salditt T. Preparation of Solid-Supported Lipid Bilayers by Spin-Coating. *Langmuir.* 2002;18(21):8172-7.
6. Jeppesen JC. Simulation and experimental study of texture in domains in lipid bilayers. Master Thesis: University of Southern Denmark; 2014.
7. Moghassemi S, Hadjizadeh A. Nano-niosomes as nanoscale drug delivery systems: an illustrated review. *J Control Release.* 2014;185:22-36.
8. Janssens M, van Smeden J, Gooris GS, Bras W, Portale G, Caspers PJ, et al. Increase in short-chain ceramides correlates with an altered lipid organization and decreased barrier function in atopic eczema patients. *J Lipid Res.* 2012;53(12):2755-66.
9. Kalluri H, Banga AK. Transdermal delivery of proteins. *AAPS PharmSciTech.* 2011;12(1):431-41.
10. Banga AK. Theme section: transdermal delivery of proteins. *Pharm Res.* 2007;24(7):1357-9.
11. Manosroi A, Khanrin P, Werner RG, Gotz F, Manosroi W, Manosroi J. Entrapment enhancement of peptide drugs in niosomes. *J Microencapsul.* 2010;27(3):272-80.
12. Marianecchi C, Di Marzio L, Rinaldi F, Celia C, Paolino D, Alhaique F, et al. Niosomes from 80s to present: the state of the art. *Adv Colloid Interface Sci.* 2014;205:187-206.
13. Sharma V, Anandhakumar S, Sasidharan M. Self-degrading niosomes for encapsulation of hydrophilic and hydrophobic drugs: An efficient carrier for cancer multi-drug delivery. *Mater Sci Eng C Mater Biol Appl.* 2015;56:393-400.
14. Junyaprasert VB, Singhsa P, Suksiriworapong J, Chantasart D. Physicochemical properties and skin permeation of Span 60/Tween 60 niosomes of ellagic acid. *International Journal of Pharmaceutics.* 2012;423(2):303-11.
15. Tavano L, Alfano P, Muzzalupo R, de Cindio B. Niosomes vs microemulsions: New carriers for topical delivery of Capsaicin. *Colloids and Surfaces B: Biointerfaces.* 2011;87(2):333-9.
16. Badran MM, Kuntsche J, Fahr A. Skin penetration enhancement by a microneedle device (Dermaroller) in vitro: dependency on needle size and applied formulation. *Eur J Pharm Sci.* 2009;36(4-5):511-23.
17. Schoellhammer CM, Blankschtein D, Langer R. Skin permeabilization for transdermal drug delivery: recent advances and future prospects. *Expert Opin Drug Deliv.* 2014;11(3):393-407.

18. Cheung K, Han T, Das DB. Effect of Force of Microneedle Insertion on the Permeability of Insulin in Skin. *Journal of Diabetes Science and Technology*. 2014;8(3):444-52.
19. Bolzinger M, Briançon S, Pelletier J, Chevalier Y. Penetration of drugs through skin, a complex rate-controlling membrane. *Current Opinion in Colloid & Interface Science*. 2012;17:156-65.
20. Skin structure [Internet]. *Biology-forums.com*. 2013 [cited 26 June 2016]. Available from: <http://biology-forums.com/index.php?action=gallery;sa=view;id=8753>.
21. Honeywell-Nguyen PL, Bouwstra JA. Vesicles as a tool for transdermal and dermal delivery. *Drug Discov Today Technol*. 2005;2(1):67-74.
22. Iwai I, Han H, den Hollander L, Svensson S, Ofverstedt LG, Anwar J, et al. The human skin barrier is organized as stacked bilayers of fully extended ceramides with cholesterol molecules associated with the ceramide sphingoid moiety. *J Invest Dermatol*. 2012;132(9):2215-25.
23. Rossetti F, Depieri LV, Bentley MV. *Confocal Laser Scanning Microscopy as a Tool for the Investigation of Skin Drug Delivery Systems and Diagnosis of Skin Disorders*. Intech Open. 2013.
24. Chen Y, Quan P, Liu X, Wang M, Fang L. Novel chemical permeation enhancers for transdermal drug delivery. *Asian Journal of Pharmaceutical Sciences*. 2014;9(2):51-64.
25. Cevc G, Blume G. Lipid vesicles penetrate into intact skin owing to the transdermal osmotic gradients and hydration force. *Biochim Biophys Acta*. 1992;1104(1):226-32.
26. Elsayed MM, Abdallah OY, Naggat VF, Khalafallah NM. Deformable liposomes and ethosomes: mechanism of enhanced skin delivery. *Int J Pharm*. 2006;322(1-2):60-6.
27. van den Bergh BA, Vroom J, Gerritsen H, Junginger HE, Bouwstra JA. Interactions of elastic and rigid vesicles with human skin in vitro: electron microscopy and two-photon excitation microscopy. *Biochim Biophys Acta*. 1999;1461(1):155-73.
28. Loan Honeywell-Nguyen P, Wouter Groenink HW, Bouwstra JA. Elastic vesicles as a tool for dermal and transdermal delivery. *J Liposome Res*. 2006;16(3):273-80.
29. Abdelkader H, Alani AW, Alany RG. Recent advances in non-ionic surfactant vesicles (niosomes): self-assembly, fabrication, characterization, drug delivery applications and limitations. *Drug Deliv*. 2014;21(2):87-100.
30. Pham TT, Jaafar-Maalej C, Charcosset C, Fessi H. Liposome and niosome preparation using a membrane contactor for scale-up. *Colloids Surf B Biointerfaces*. 2012;94:15-21.
31. Liu T, Guo R. Preparation of a Highly Stable Niosome and Its Hydrotrope-Solubilization Action to Drugs. *Langmuir*. 2005;21(24):11034-9.
32. Gregoriadis G, Florence A.T., Patel H.M., editor. *Liposomes in drug delivery*. Switzerland: Harwood Academic Publishers; 1993.
33. Nagarajan R. Molecular Packing Parameter and Surfactant Self-Assembly: The Neglected Role of the Surfactant Tail. *Langmuir*. 2002;18(1):31-8.
34. Tadros TF. *Applied surfactants: Principles and applications*. Weinheim, Germany: Wiley; 2005.
35. Kumar GP, Rajeshwarrao P. Nonionic surfactant vesicular systems for effective drug delivery—an overview. *Acta Pharmaceutica Sinica B*. 2011;1(4):208-19.
36. Manosroi A, Wongtrakul P, Manosroi J, Sakai H, Sugawara F, Yuasa M, et al. Characterization of vesicles prepared with various non-ionic surfactants mixed with cholesterol. *Colloids and Surfaces B: Biointerfaces*. 2003;30(1-2):129-38.

37. Junyaprasert VB, Singhsa P, Jintapattanakit A. Influence of chemical penetration enhancers on skin permeability of ellagic acid-loaded niosomes. *Asian Journal of Pharmaceutical Sciences*. 2013;8(2):110-7.
38. Gratieri T, Alberti I, Lapteva M, Kalia YN. Next generation intra- and transdermal therapeutic systems: using non- and minimally-invasive technologies to increase drug delivery into and across the skin. *Eur J Pharm Sci*. 2013;50(5):609-22.
39. Wiedersberg S, Guy RH. Transdermal drug delivery: 30+ years of war and still fighting! *J Control Release*. 2014;190:150-6.
40. Martanto W, Davis SP, Holiday NR, Wang J, Gill HS, Prausnitz MR. Transdermal delivery of insulin using microneedles in vivo. *Pharm Res*. 2004;21(6):947-52.
41. Narayan RJ. Transdermal delivery of insulin via microneedles. *J Biomed Nanotechnol*. 2014;10(9):2244-60.
42. Chen MC, Ling MH, Kusuma SJ. Poly-gamma-glutamic acid microneedles with a supporting structure design as a potential tool for transdermal delivery of insulin. *Acta Biomater*. 2015;24:106-16.
43. Ita K. Transdermal Delivery of Drugs with Microneedles-Potential and Challenges. *Pharmaceutics*. 2015;7(3):90-105.
44. Ita K. Transdermal delivery of heparin: Physical enhancement techniques. *Int J Pharm*. 2015;496(2):240-9.
45. Diaspro A, Bianchini P, Vicidomini G, Faretta M, Ramoino P, Usai C. Multi-photon excitation microscopy. *Biomed Eng Online*. 2006;5:36.
46. Periasamy A, Clegg RM. *FLIM Microscopy in Biology and Medicine*. USA: Taylor and Francis Group, LLC; 2010.
47. Kappel C. ScienceLab [Internet]. Kappel C, editor: Leica Microsystems. 2012. [cited 2016]. Available from: <http://www.leica-microsystems.com/science-lab/fret-with-flim/>.
48. Lakowicz JR. *Principles of Fluorescence Spectroscopy*, 3rd edition. Lakowitz JR, editor. Baltimore, USA: Springer; 2006.
49. Jares-Erijman EA, Jovin TM. FRET imaging. *Nat Biotech*. 2003;21(11):1387-95.
50. Levitt JA, Matthews DR, Ameer-Beg SM, Suhling K. Fluorescence lifetime and polarization-resolved imaging in cell biology. *Curr Opin Biotechnol*. 2009;20(1):28-36.
51. Siegel J, Suhling K, Lévêque-Fort S, Webb SED, Davis DM, Phillips D, et al. Wide-field time-resolved fluorescence anisotropy imaging (TR-FAIM): Imaging the rotational mobility of a fluorophore. *Review of Scientific Instruments*. 2003;74(1):182-92.
52. Birch DJS. Multiphoton excited fluorescence spectroscopy of biomolecular systems. *Spectrochimica Acta Part A: Molecular and Biomolecular Spectroscopy*. 2001;57(11):2313-36.
53. Simonsen AC, Bagatolli LA. Structure of spin-coated lipid films and domain formation in supported membranes formed by hydration. *Langmuir*. 2004;20(22):9720-8.
54. Jeppesen JC, Solovyeva V, Brewer JR, Johannes L, Hansen PL, Simonsen AC. Slow Relaxation of Shape and Orientational Texture in Membrane Gel Domains. *Langmuir*. 2015;31(46):12699-707.
55. Dreier J. *Orientational Texture of Lipid Bilayer and Monolayer Domains*. PhD thesis: University of Southern Denmark; 2012.
56. Edelstein A, Amodaj N, Hoover K, Vale R, Stuurman N. Computer control of microscopes using microManager. *Curr Protoc Mol Biol*. 2010;Chapter 14:Unit14 20.
57. Schneider CA, Rasband WS, Eliceiri KW. NIH Image to ImageJ: 25 years of image analysis. *Nat Meth*. 2012;9(7):671-5.

58. Berezin MY, Achilefu S. Fluorescence Lifetime Measurements and Biological Imaging. *Chemical reviews*. 2010;110(5):2641-84.
59. The Nyquist stability test [Internet]. 1993 [cited 28 June 2016]. Available from: <http://web.stanford.edu/class/archive/ee/ee214/ee214.1032/Handouts/nyquist.pdf>.
60. Digman MA, Caiolfa VR, Zamai M, Gratton E. The phasor approach to fluorescence lifetime imaging analysis. *Biophys J*. 2008;94(2):L14-6.
61. Calle D, Negri V, Ballesteros P, Cerdan S. Magnetoliposomes loaded with polyunsaturated fatty acids as novel theranostic anti-inflammatory formulations. *Theranostics*. 2015;5(5):489-503.
62. OECD GUIDELINE FOR THE TESTING OF CHEMICALS: Skin absorption - in vitro method [Internet]. 2004 [cited 23 May 2016]. Available from: [http://www.oecd-ilibrary.org/environment/test-no-428-skin-absorption-in-vitro-method\\_9789264071087-en](http://www.oecd-ilibrary.org/environment/test-no-428-skin-absorption-in-vitro-method_9789264071087-en).
63. Hinde E, Digman MA, Welch C, Hahn KM, Gratton E. Biosensor FRET detection by the phasor approach to fluorescence lifetime imaging microscopy (FLIM). *Microscopy research and technique*. 2012;75(3):271-81.
64. Christensen TQ. Applications of FRET and FLIM-FRET. Odense: University of Southern Denmark; 2015.
65. Lunz M, Bradley AL, Gerard VA, Byrne SJ, Gun'ko YK, Lesnyak V, et al. Concentration dependence of Förster resonant energy transfer between donor and acceptor nanocrystal quantum dot layers: Effect of donor-donor interactions. *Physical Review B*. 2011;83(11):115423.
66. Charrier A, Thibaudau F. Main phase transitions in supported lipid single-bilayer. *Biophys J*. 2005;89(2):1094-101.
67. Rhodamine B product specification [Internet]. Sigma Aldrich. [cited 27 June 2016]. Available from: [http://www.sigmaaldrich.com/Graphics/COFAInfo/SigmaSAPQM/SPEC/R6/R6626/R6626-BULK\\_SIGMA.pdf](http://www.sigmaaldrich.com/Graphics/COFAInfo/SigmaSAPQM/SPEC/R6/R6626/R6626-BULK_SIGMA.pdf).
68. Kay JG, Koivusalo M, Ma X, Wohland T, Grinstein S. Phosphatidylserine dynamics in cellular membranes. *Mol Biol Cell*. 2012;23(11):2198-212.
69. Song KC, Livanec PW, Klauda JB, Kuczera K, Dunn RC, Im W. Orientation of fluorescent lipid analogue BODIPY-PC to probe lipid membrane properties: insights from molecular dynamics simulations. *J Phys Chem B*. 2011;115(19):6157-65.
70. Roberts MS, Dancik Y, Prow TW, Thorling CA, Lin LL, Grice JE, et al. Non-invasive imaging of skin physiology and percutaneous penetration using fluorescence spectral and lifetime imaging with multiphoton and confocal microscopy. *Eur J Pharm Biopharm*. 2011;77(3):469-88.
71. Ariola FS, Mudaliar DJ, Walvick RP, Heikal AA. Dynamics imaging of lipid phases and lipid-marker interactions in model biomembranes. *Physical Chemistry Chemical Physics*. 2006;8(39):4517-29.
72. Dreier J, Sorensen JA, Brewer JR. Superresolution and Fluorescence Dynamics Evidence Reveal That Intact Liposomes Do Not Cross the Human Skin Barrier. *PLoS One*. 2016;11(1):e0146514.
73. Matthews DR, Carlin LM, Ofo E, Barber PR, Vojnovic B, Irving M, et al. Time-lapse FRET microscopy using fluorescence anisotropy. *J Microsc*. 2010;237(1):51-62.
74. Matthews DR, Ameer-Beg SM, Barber P, Pierce GP, Newman RG, Vojnovic B, et al, editors. A high-content screening platform utilizing polarization anisotropy and FLIM microscopy 2008.

75. Veatch SL, Keller SL. Separation of liquid phases in giant vesicles of ternary mixtures of phospholipids and cholesterol. *Biophys J*. 2003;85(5):3074-83.
76. Zhu Y, Negmi A, Moran-Mirabal J. Multi-Stacked Supported Lipid Bilayer Micropatterning through Polymer Stencil Lift-Off. *Membranes (Basel)*. 2015;5(3):385-98.
77. Wessely Z, Shapiro SH, Klavins JV, Tinberg HM. Identification of Mallory bodies with rhodamine B fluorescence and other stains for keratin. *Stain Technol*. 1981;56(3):169-76.
78. Alomrani AH, Al-Agamy MH, Badran MM. In vitro skin penetration and antimycotic activity of itraconazole loaded niosomes: Various non-ionic surfactants. *Journal of Drug Delivery Science and Technology*. 2015;28:37-45.
79. Romero EL, Morilla MJ. Highly deformable and highly fluid vesicles as potential drug delivery systems: theoretical and practical considerations. *Int J Nanomedicine*. 2013;8:3171-86.
80. Verma DD, Verma S, Blume G, Fahr A. Particle size of liposomes influences dermal delivery of substances into skin. *Int J Pharm*. 2003;258(1-2):141-51.
81. Mali N, Darandale S, Vavia P. Niosomes as a vesicular carrier for topical administration of minoxidil: formulation and in vitro assessment. *Drug Delivery and Translational Research*. 2013;3(6):587-92.
82. Zhang Y, Zhang K, Wu Z, Guo T, Ye B, Lu M, et al. Evaluation of transdermal salidroside delivery using niosomes via in vitro cellular uptake. *Int J Pharm*. 2015;478(1):138-46.
83. Abdelbary AA, AbouGhaly MH. Design and optimization of topical methotrexate loaded niosomes for enhanced management of psoriasis: application of Box-Behnken design, in-vitro evaluation and in-vivo skin deposition study. *Int J Pharm*. 2015;485(1-2):235-43.
84. Manosroi A, Chaikul P, Abe M, Manosroi W, Manosroi J. Melanogenesis of methyl myristate loaded niosomes in B16F10 melanoma cells. *J Biomed Nanotechnol*. 2013;9(4):626-38.
85. Percutaneous Penetration Enhancers. *Chemical Methods in Penetration Enhancement*. Dragievic N, Maibach H, editor. San Francisco, USA: Springer; 2016.
86. Verma DD, Verma S, Blume G, Fahr A. Liposomes increase skin penetration of entrapped and non-entrapped hydrophilic substances into human skin: a skin penetration and confocal laser scanning microscopy study. *European Journal of Pharmaceutics and Biopharmaceutics*. 2003;55(3):271-7.

## APPENDIX I: Rhodamine B calibration

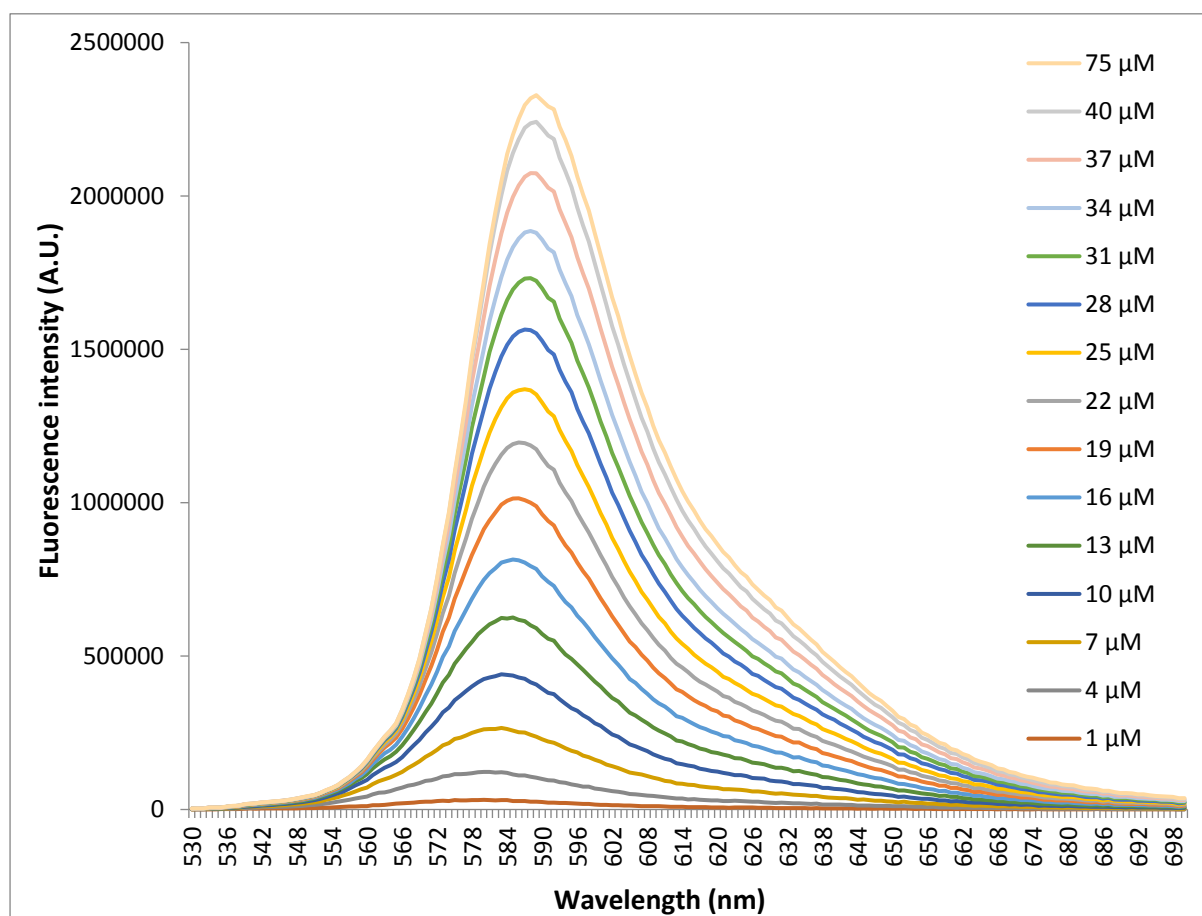


**Figure S1.** Rhodamine-B fluorescence emission spectra: 1 - 75 μM.  $\lambda_{\text{abs}} = 543 \text{ nm}$ .

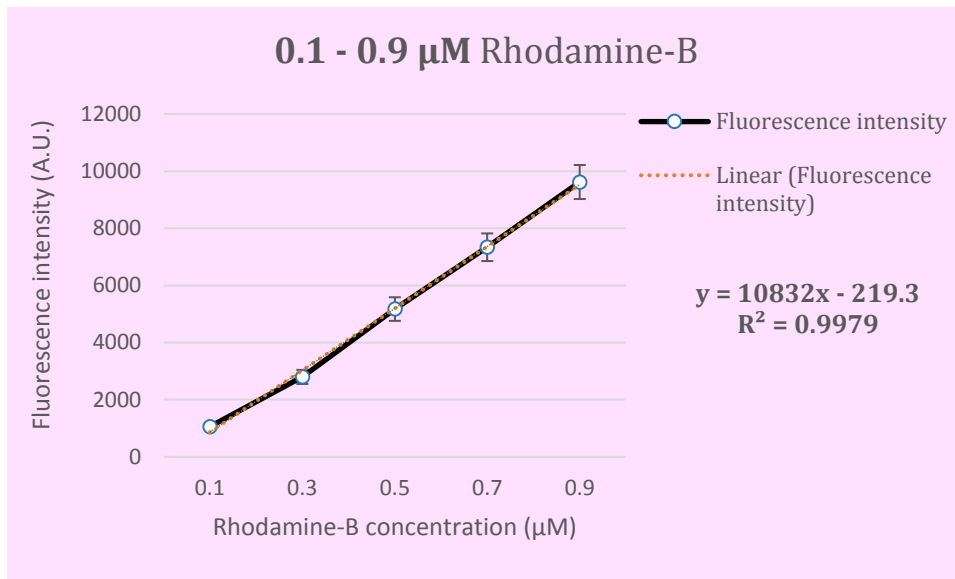


**Figure S2.** Rhodamine B calibration curve used for the determination of encapsulation efficiency.

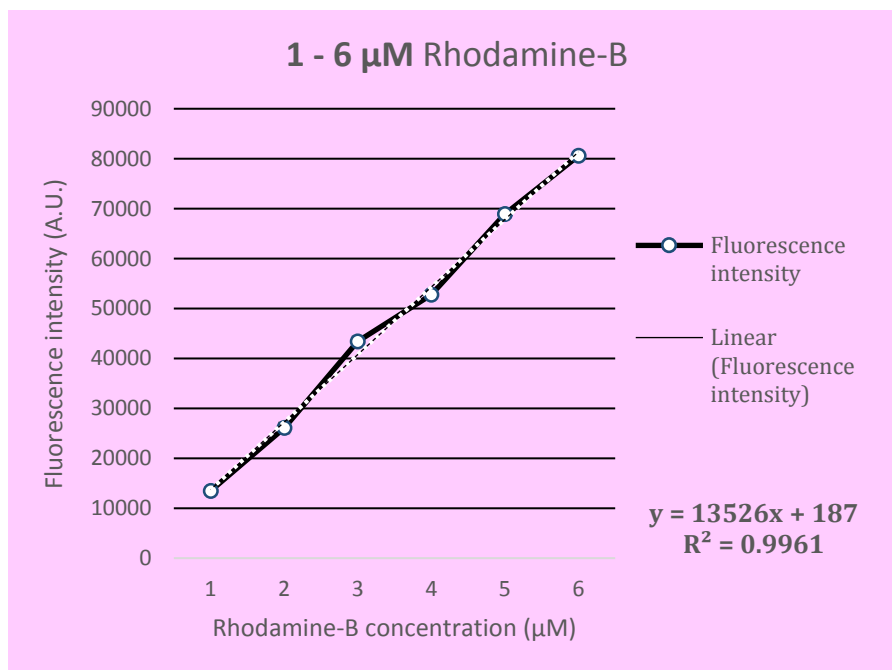
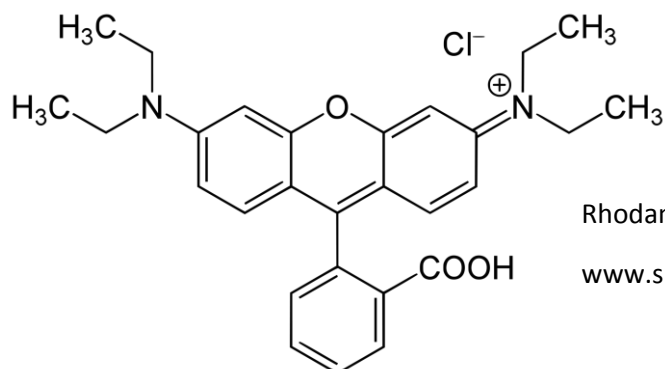


**Figure S3.** Rhodamine B calibration curve used for the analysis of the receptor compartment in the Franz diffusion experiment.

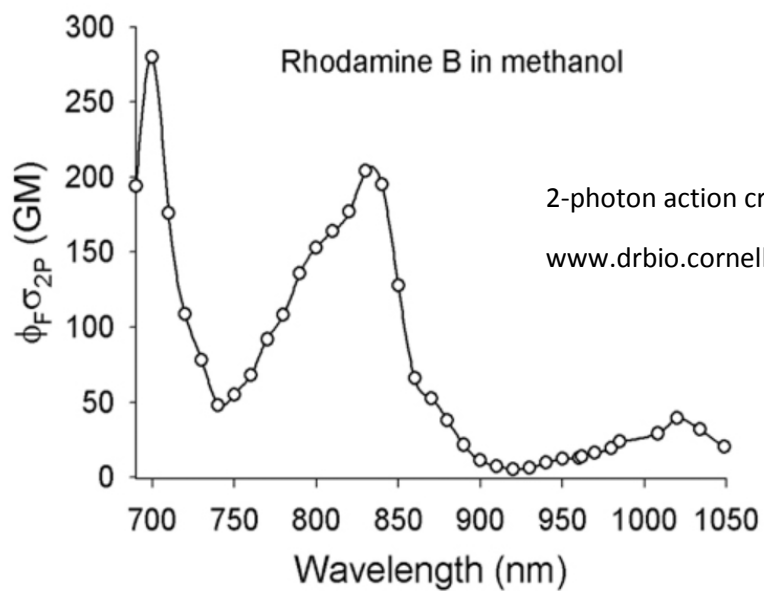
## APPENDIX II. Structure and spectra of the fluorescent probes

All information was found online. The source website is mentioned for each figure.

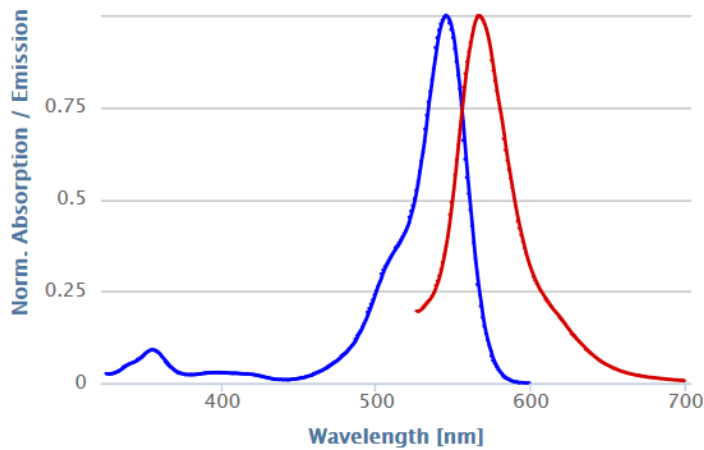
### Rhodamine-B



Rhodamine-B structure  
[www.sigmaaldrich.com](http://www.sigmaaldrich.com)



Rhodamine B in methanol  
2-photon action cross-section  
[www.drbio.cornell.edu](http://www.drbio.cornell.edu)



### Overview

Absorption  $\lambda_{\max}$

**545 nm, 355 nm**

Emission  $\lambda_{\max}$

**566 nm**

Solvent

**Methanol**

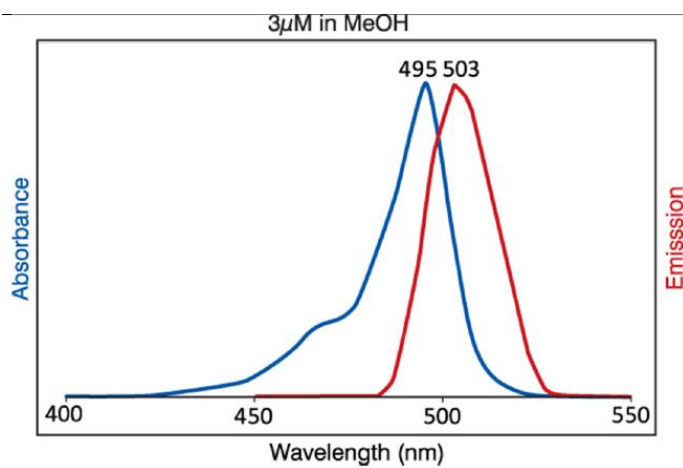
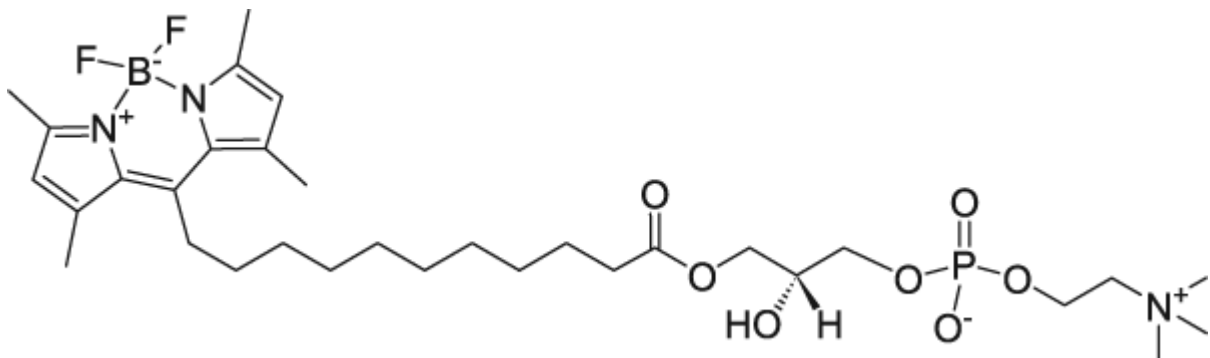
Molar Abs. Coefficient

-

Rhodamine-B spectra and properties

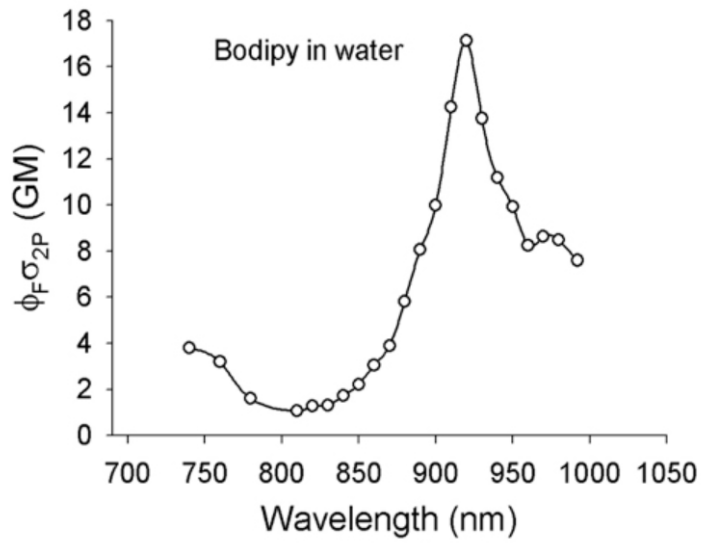
[www.fluorophores.tugraz.at](http://www.fluorophores.tugraz.at)

## TopFluor-PC



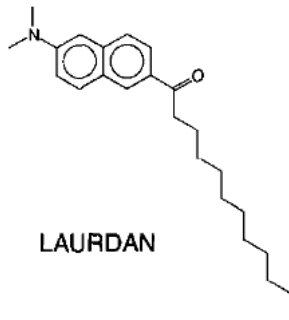
TopFluor-PC spectra and properties

[www.avantilipids.com](http://www.avantilipids.com)

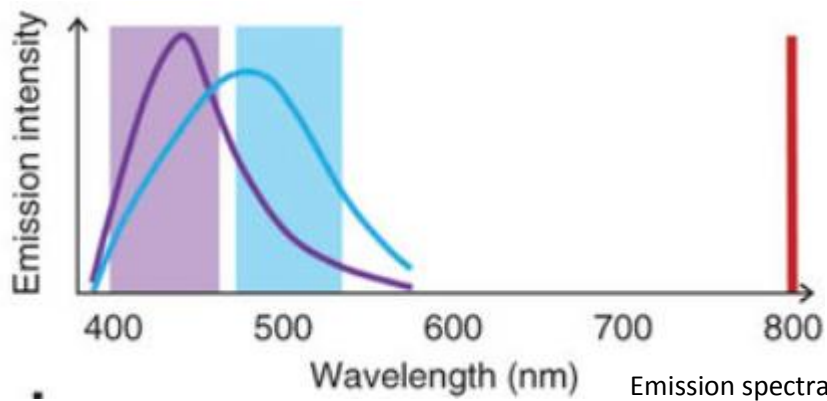


Bodipy (label in TopFluor)  
 2-photon action cross-section  
[www.drbio.cornell.edu](http://www.drbio.cornell.edu)

## Laurdan

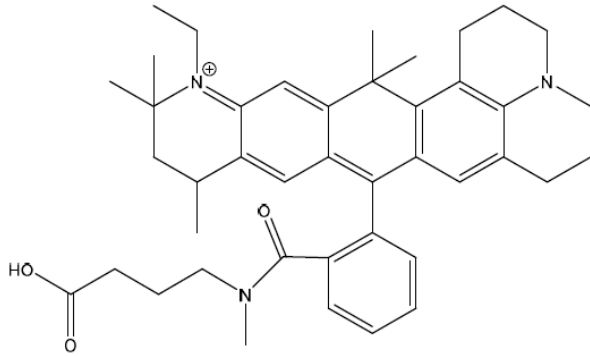


Structure  
[www.memphys.sdu.dk](http://www.memphys.sdu.dk)



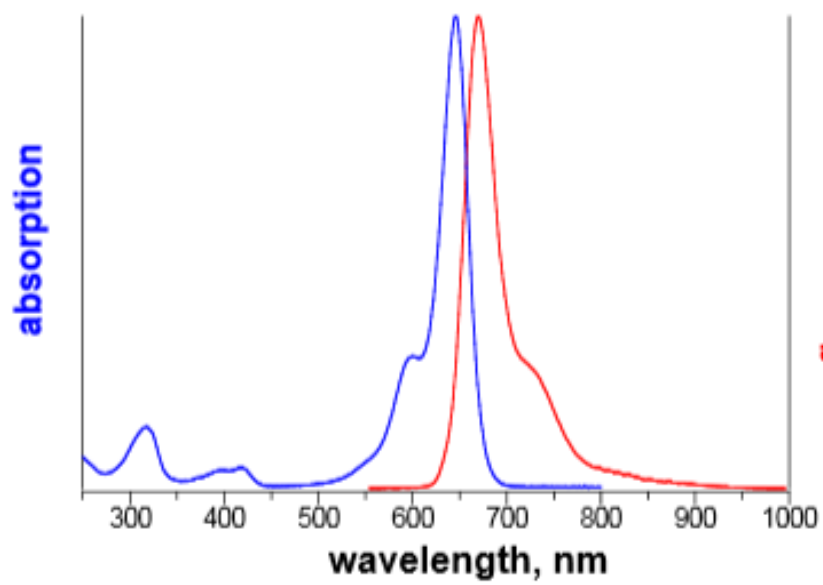
Emission spectra  
[www.nature.com](http://www.nature.com)

# ATTO647N

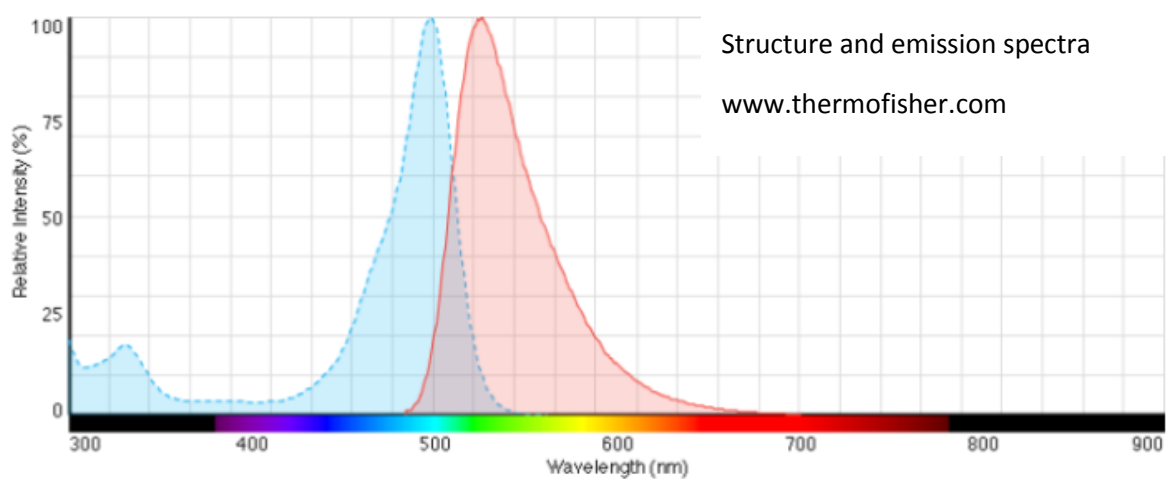
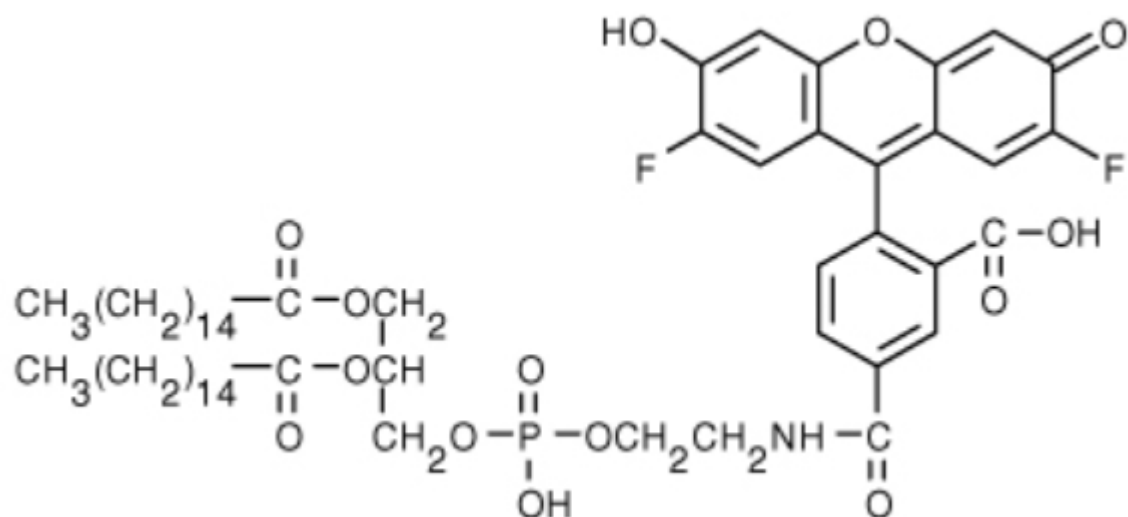


Structure and emission spectra

[www.atto-tec.com](http://www.atto-tec.com)



# Oregon green



APPENDIX III. Additional images from the skin FRET experiment

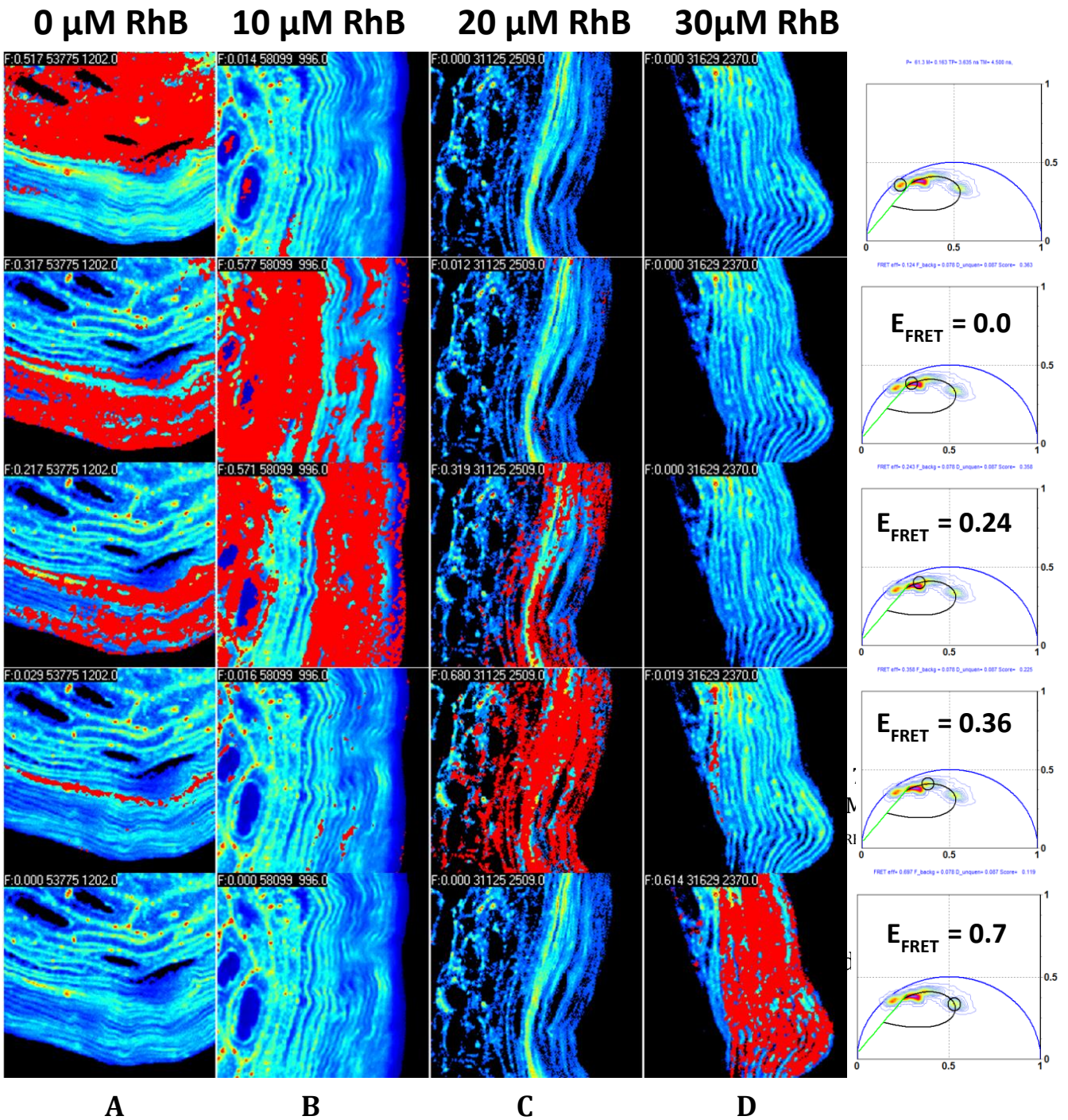


**Figure S4.** Intensity images of human epidermis labelled with: Column A: 7  $\mu$ M TopFluor-PC. Columns B, C, D: 7  $\mu$ M TopFluor-PC and 10  $\mu$ M, 20  $\mu$ M and 30  $\mu$ M rhodamine B, respectively. The red highlight maps the pixels in the image which have the  $E_{\text{FRET}}$  measured on the phasor diagram on the right.

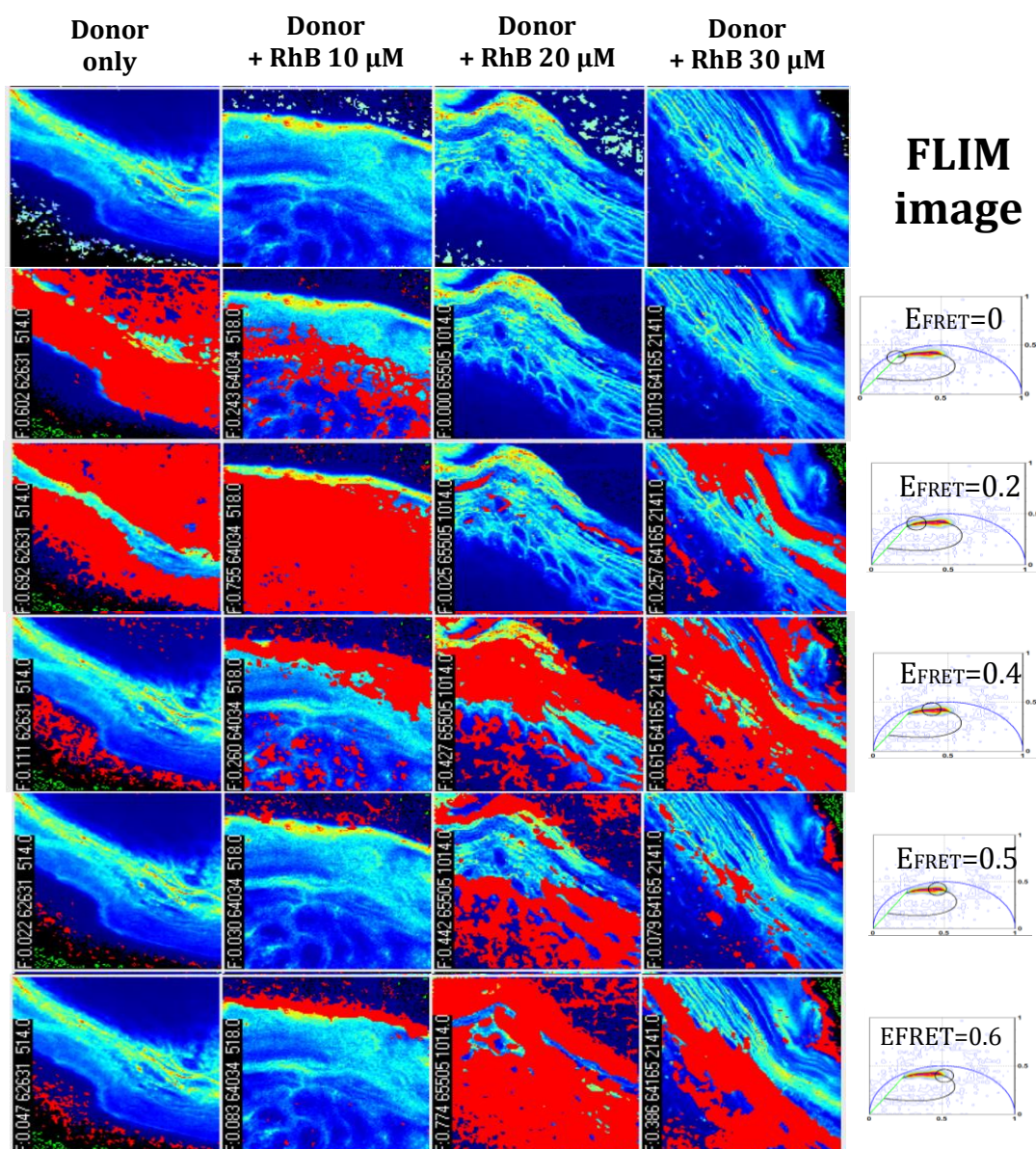


**Figure S5.** Intensity images of human epidermis labelled with: Column **A**: 3.5  $\mu\text{M}$  TopFluor-PC. Columns **B, C, D**: 3.5  $\mu\text{M}$  TopFluor-PC and 10  $\mu\text{M}$ , 20  $\mu\text{M}$  and 30  $\mu\text{M}$  rhodamine B, respectively. The red highlight maps the pixels in the image which have the  $E_{\text{FRET}}$  measured on the phasor diagram on the right.

## Appendix IV: Human skin manipulation and labelling for FRET imaging

Skin samples: obtained from abdominoplasty operations at OUH. Information about the skin: male 44 years old, skin collected 31. March 2016, removed the adipose tissue, cut into  $\sim 1\text{cm}^3$  pieces and cryopreserved at  $-80^\circ\text{C}$  until use.

On the day of the labelling, the skin was removed from the  $-80^\circ\text{C}$  freezer, cut into  $20\ \mu\text{m}$  slices using a cryomicrotome (Cryotome FSE, Thermo Scientific, Denmark) and transferred to SuperFrost®Plus microscope slides (VWR, Denmark)

The skin labelling protocol was optimized by a previous bachelor student in our group and consists of the following steps:

- After sectioning, the skin samples are fixed for 10 minutes in MeOH at  $-20^\circ\text{C}$ ;
- Rinse twice with 1 mL of PBS buffer (pH 7.4);
- A hydrophobic marker is used to draw a circle around the skin sample;
- 100  $\mu\text{L}$  of the TopFluor dye solution in DMSO was added and the samples were left to label overnight;
- The dye was removed and the sample was rinsed at least 3 times with PBS buffer (pH 7.4)
- 150  $\mu\text{L}$  PBS buffer (pH 7.4) was added to the sample and left for 15-30 minutes;
- The buffer was removed and steps 4-7 were repeated for the samples where the hydrophilic dye Rhodamine-B in PBS was added.
- Samples were left overnight to label.

After labelling, the excess labelling solution was removed and the samples were mounted with 30  $\mu\text{L}$  PBS and covered with round cover slips. The cover slips were sealed to the microscope slides with nail polish. The microscope slides with the skin samples were flipped before imaging (with the round cover slide facing the objective).